POLYFLUORENE-BASED ORGANIC FIELD-EFFECT TRANSISTORS

by

Michael C. Hamilton

A dissertation submitted in partial fulfillment
of the requirements for the degree of
Doctor of Philosophy
(Electrical Engineering)
in The University of Michigan
2005

Doctoral Committee:

Professor Jerzy Kanicki, Chair
Professor Kensall D. Wise
Professor Stephen C. Rand
Professor David C. Martin
Adjunct Assistant Professor Sandrine Martin

© Michael C. Hamilton 2005
All Rights Reserved

This thesis is dedicated to my beautiful wife, Brandi, my amazing daughter, Sydney, and to my late grandparents, Mr. and Mrs. Marvin Clayton Hamilton.

ACKNOWLEDGEMENTS

I sincerely thank Prof. Jerzy Kanicki, my doctoral committee chair and research advisor, for giving me the opportunity to work within his research group on this very interesting and exciting project, and for providing excellent guidance and advice throughout my time in his group. I also sincerely thank my doctoral committee members: Prof. Kensall Wise, Prof. Stephen Rand, Prof. David Martin and Dr. Sandrine Martin for their time and effort in helping me to complete this work. Special thanks are in order for Dr. Sandrine Martin for her kindness, helpfulness and advice throughout this process. It would have been nearly impossible for me to reach this point without the help, support and creative diversions provided by all of my current group members: Aaron Johnson, Alex Kuo, Hojin Lee, Luke Lee and Patrick Shea. I would like to thank my previous group members for providing useful discussions and assistance in the early stages of my work: Dr. Yongtaek Hong, Dr. ShuJen Lee, and Dr. Joohan Kim. I gratefully thank the Dow Chemical Company (especially David Brennan, Paul Townsend and Scott Kisting) for providing the organic semiconductor F8T2 polymer used in this work and the United States Department of Defense for providing funding through a National Defense Science and Engineering Graduate Fellowship. Finally, I must acknowledge the dedication and assistance of Beth Stalnaker, Becky Turanski and Elizabeth Fisher of the Electrical Engineering and Computer Science Department of the University of Michigan.

TABLE OF CONTENTS

DEDICATION . . . . **ii**

ACKNOWLEDGEMENTS . . . . **iii**

LIST OF TABLES . . . . **vi**

LIST OF FIGURES . . . . **vii**

CHAPTER

1. INTRODUCTION 1

1.1 Organic semiconductors 2
1.2 Outline of this thesis 7
References 11

2. DC CHARACTERISTICS OF PF-BASED OFETS 17

2.1 Device structure 18
2.2 DC operation and measurement 19
2.2.1 Measurement setup 20
2.3 DC performance parameter extraction methods and models 24
2.3.1 Extraction methods and discussion 26
2.3.2 Dependence on temperature 36
2.4 Source/drain contact resistance and intrinsic device performance 40
2.4.1 Experimental results and analysis 42
2.5 High-field operation 46
2.5.1 Experimental results and analysis 49
2.6 Conclusion 52
References 54

3. EFFECTS OF ILLUMINATION ON PF-BASED OFETS 57

3.1 Effects of broadband illumination 58
3.1.1 Experimental setup 58
3.1.2 Device under illumination 61
3.1.3 Experimental results and analysis 66
3.2 Effects of monochromatic illumination 77
3.2.1 Experimental setup 77

3.2.2 Device under illumination . . . 79
3.2.3 Experimental results and analysis . . . 81
3.3 Conclusion . . . 97
References . . . 99

4. HYSTERESIS IN THE ELECTRICAL CHARACTERISTICS OF PF-BASED OFETS . . . 101

4.1 Hysteresis in the electrical characteristics of OFETs . . . 101
4.1.1 Experimental results and analysis . . . 103
4.1.2 Dependence on temperature . . . 109
4.1.3 Dependence on illumination . . . 110
4.2 Reduction of hysteresis . . . 114
4.3 Conclusion . . . 117
References . . . 120

5. BIAS - TEMPERATURE STRESS AND INSTABILITIES OF PF-BASED OFETs . . . 122

5.1 Bias -temperature stress of OFETs . . . 122
5.1.1 Experimental methods . . . 123
5.1.2 Experimental results and analysis . . . 124
5.2 Maximum operating temperature . . . 139
5.3 Conclusion . . . 141
References . . . 144

6. PHOTODISCHARGE INVESTIGATION OF THE DENSITY OF STATES IN PF-BASED OFETS . . . 146

6.1 Experimental methods . . . 147
6.2 Experimental results and analysis . . . 148
6.2.1 Dependence on applied gate voltage . . . 148
6.2.2 Dependence on temperature . . . 154
6.3 Conclusion . . . 160
References . . . 161

7. CONCLUSIONS AND FUTURE WORK . . . 162

7.1 Summary . . . 162
7.2 Future directions . . . 166

APPENDIX . . . **168**

LIST OF TABLES

Table

2.1 OFET Electrical Characteristics Measurement Bias Conditions 22

2.2 Fitting Parameters Used For Figure 2-3(b). 30

LIST OF FIGURES

Figure

1.1 Chemical structure of the organic molecules (a) pentacene, (b) tetrabenzoporphyrin (c) sexithiophene and (d) poly-3-hexylthiophene. 3

1.2 Chemical structure of the organic polymer polyacetylene describing the alternating double- (π) and single- (σ) carbon-carbon bonds. 3

1.3 (a) Energy levels of a single molecule demonstrating the Highest Occupied Molecular Orbital and Lowest Unoccupied Molecular Orbital. (b) Schematic intermediate range of an amorphous conglomeration of several molecules and the corresponding broadening of the molecular orbitals and breaking of conjugation that leads to allowed states within the energy gap. (c) Schematic density of states for an amorphous film of an organic (or inorganic) semiconductor showing the band edges (band-tails) as well as the allowed states within the gap. 4

2.1 (a) Cross-section of device structure and chemical structure of F8T2. (b) TEM cross-section of device structure courtesy of Elvin Beach, Steve Rozeveld, and Charlie Wood of the Dow Chemical Company. (c) Top-view of device showing gate, source, and drain. For this device, L = 56μm, W = 116μm and source/drain-gate overlap is 5μm. 19

2.2 (a) Output characteristics of an OFET with L = 16μm, W = 56μm, source/drain-gate overlap of approximately 5μm (b) Linear regime ($V_{DS} < V_{GS} - V_T$) transfer characteristics of same OFET. Lines are fits to equations (2.2) and (2.4). (c) Saturation regime ($V_{DS} \approx V_{GS} - V_T$) transfer characteristics of same OFET. . . . 21

2.3 F8T2-based OFET linear regime transfer characteristics. Arrows indicate direction of measurement. 27

2.4 OFET transfer characteristics in the linear and saturation regimes. Symbols represent experimental data, solid lines show fits to equation (2.10) and equation (2.20), respectively. 28

2.5 Comparison of the results of several extraction methods used to find the OFET field-effect mobility of the same device as used in Figure 2.3, in the linear regime. 32

2.6 Comparison of the results of several extraction methods used to find the OFET field-effect mobility of the same device as used in Figure 2.3, in the saturation regime. 35

2.7 Linear regime transfer characteristics of an OFET measured at different temperatures between 10°C and 80°C. The symbols correspond to experimental data and the lines correspond to fits using equation (2.10) 37

2.8 Dependence of the field-effect mobility on applied gate bias at different temperatures, found from the data shown in Figure 2.7 using equation (2.10) and equation (2.14). 38

2.9 Dependence of the OFET field-effect mobility on temperature, taken from the data shown in Figure 2.7 at different gate biases. $|V_{GS}|$ increases from 28V to 40V for the data from the bottom to the top of the figure. Symbols are experimental data and straight lines are the fits to an Arrhenius relationship, giving the activation energy (E_a) of the field-effect mobility. 38

2.10 The activation energy of the OFET field-effect mobility as a function of applied gate bias, found from the data shown in Figure 2.9. 39

2.11 Dependence of the OFET threshold voltage on temperature, extracted from the data shown in Figure 2.7. Symbols are experimental data and the straight line is the linear fit, which serves as a guide to the eye. 40

2.12 Dependence of the OFET gamma parameter on temperature, extracted from the data shown in Figure 2.7. Symbols are experimental data and the straight lines are linear fits to the corresponding sections of the gamma data and serve as guides to the eye. 41

2.13 Drain current versus drain-to-source voltage for device measured with the gate electrode as common and floating. 42

2.14 Normalized ON resistance (i.e., $W \times R_{ON} = W \times V_{DS}/I_D$) as a function of channel length for different applied gate biases above the threshold voltage. Similar results were obtained for calculations for measurements at the other temperatures. 43

2.15 Inverse slopes of the linear fits to the data in Figure 2.14 as a function of applied gate bias above threshold voltage, (i.e., $d(W \times R_{ON})/dL)^{-1}$ vs. V_{GS}). 44

2.16 Intrinsic field-effect mobility (taken from the slopes of the data in Figure 2.15) plotted as a function of inverse temperature. 45

2.17 Intrinsic threshold voltage (taken from the x-intercepts of the linear fits shown in Figure 2.15) as a function of temperature. 45

2.18 Normalized S/D contact resistance (i.e., channel width times total extracted S/D series resistance) as a function of applied gate bias for 283 < T < 343K. 46

2.19 Normalized contact resistance as a function of temperature for various applied gate biases above threshold. 47

2.20 Activation energy of the normalized contact resistance as a function of applied gate bias. 47

2.21 Average normalized channel resistance (i.e., channel resistance per unit channel length averaged over the range of different device geometries used in this study) as a function of applied gate biases above threshold for a range of temperatures. . 48

2.22 Average normalized channel resistance as a function of temperature for a range of applied gate biases. 48

2.23 Activation energy of the average normalized channel resistance as a function of applied gate bias. 49

2.24 (a) Output characteristics of a device measured to $V_{DS max} = V_{GS max} = -100V$. (b) Linear regime transfer characteristics of a device measured (using a maximum gate bias of $V_{GS max}$ = -100V, corresponding to a maximum estimated electric field across the gate insulator of 1.67×10^5 V/cm) measured from OFF to strong accumulation (circles) and strong accumulation to OFF (triangles). 50

2.25 Gate leakage current as a function of applied gate-to-source bias, shown for two different applied drain-to-source biases. 51

2.26 Saturation regime transfer characteristics (i.e., $V_{DS} = V_{GS}$). 51

3.1 (a) Cross-section of device structure and chemical structure of F8T2. (b) Top-view of illuminated device showing gate, source, and drain. For this device, L = 56μm, W = 116μm and source/drain-gate overlap is 5μm 60

3.2 Absorption coefficient of F8T2 and light emission spectrum of incident light as a function of the photon energy. 61

3.3 (a) Output characteristics of OFET in the dark and illuminated at $2.9W/cm^2$. (b) Transfer characteristics of OFET in the dark and illuminated at $2.9W/cm^2$ 62

3.4 Proposed energy band diagram of OFET under illumination in the region from (a) the gate electrode to the source electrode (i.e., following the line A to C in Figure 3.1(a)) and (b) the drain electrode to the source electrode (i.e., following the line B to C in Figure 3.1(a)). 64

3.5 Transfer characteristics of OFET in the dark and under various irradiance levels. . 66

3.6 Dependence of ON-state drain current, OFF-state drain current, field-effect mobility, threshold voltage, and apparent subthreshold slope on irradiance. μ_{FE}, V_T, and S^* extracted from the data in Figure 3.5, using equations (2.2) and (2.4). Lines are provided as guides to the eye. 67

3.7 Threshold voltage-normalized transfer characteristics (i.e., I_D versus $V_{GS} - V_T$) of OFET in the dark and illuminated at various irradiance levels. 69

3.8 OFET responsivity (R) and photosensitivity (P) versus V_{GS} for various irradiance levels taken from data for the same device shown in Figure 3.7. 71

3.9 OFET responsivity (R) and photoresponse ($R_{L/D}$) versus irradiance for various V_{GS}. 73

3.10 Power exponent γ (experimental and fit using equations (3.5a) and (3.5b)) versus V_{GS} 75

3.11 I_{Dillum} / I_{Ddark} at maximum irradiance versus V_{DS} at various V_{GS} 77

3.12 Threshold voltage-normalized transfer characteristics of OFET illuminated at different wavelengths/photon energies, measured with a constant optical flux of 5×10^{13} photons/cm^{2}sec. The straight lines are fits using equations (2.2) and (2.4). 80

3.13 Dependence of ON-state drain current, OFF-state drain current, and the change in threshold voltage on the energy of the incident photons. Extracted from the non-threshold voltage-normalized transistor characteristics (not shown), using equations (2.2). Also shown is an estimation of the number of photons absorbed per second in the channel region of the device as a function of the photon energy. . . 82

3.14 Responsivity (R), photosensitivity (P) and external quantum efficiency (EQE) versus V_{GS} of the OFET for illumination at different wavelengths/photon energies with W =56μm, L =6μm, and V_{DS} =-10V. 85

3.15 Responsivity (R), photosensitivity (P) and external quantum efficiency (EQE) versus the energy of incident photons (measured with a constant optical flux of $5{\times}10^{13}$ photons/cm^{2}sec) for different biasing regimes of an OFET with W =56μm, L =6μm, and V_{DS} =-10V. 86

3.16 Threshold voltage-normalized transfer characteristics of OFET illuminated at a wavelength of 460nm (corresponding to maximum absorption of the F8T2 polymer film) for different irradiance levels. The straight lines are fits using equations (2.2) and (2.4). 91

3.17 Dependence of ON-state drain current, OFF-state drain current and the change in threshold voltage on irradiance at a wavelength of 460nm. Also shown is the number of photons absorbed in the channel region of the device as a function of incident irradiance. 92

3.18 Responsivity (R), photosensitivity (P) and external quantum efficiency (EQE) of an OFET versus V_{GS} for various irradiance levels at a wavelength of 460nm with W =56μm, L =6μm, and V_{DS} =-10V. 94

3.19 γ-factor of the OFET versus V_{GS} for various irradiance levels at a wavelength of 460nm. 96

4.1 Transfer characteristics (measured from OFF to Strong Accumulation (SA) to OFF) of device measured to different maximum V_{GS} (V_{GMax}). Also shown for reference is transfer characteristics of OFET on semilog scale. Lines are fits to equations (1) and (2). For this device, L = 16μm, W = 56μm and the source/drain-gate overlap is approximately 5μm. 104

4.2 (a) Transfer characteristics (from OFF to ON to OFF) for different total measurement time (i.e., varying step time, with same number of steps). (b) Transfer characteristics (from OFF to ON to OFF) measured back-to-back, with no time delay between measurements. 106

4.3 (a) Output characteristics (V_{DS} = 0V to V_{DS} = -highV to V_{DS} = 0V) for same V_{DSmax} and different V_{GS}. (b) Output characteristics (V_{DS} = 0V to V_{DS} = -highV to V_{DS} = 0V) to a larger V_{DSmax}. 108

4.4 Q_{hyst} as a function of V_{GSmax}, taken from the data of Figure 4.1, with two different exponential fits. 109

4.5 Transfer characteristics (from OFF to ON to OFF) for device measured at different temperatures on (a) linear and (b) semilog scales. (c) Q_{hyst} (as defined in the text) and $|I_{ON}|$ as functions of the measurement temperature for the data presented in Figure 4.5(a). 111

4.6 (a) Transfer characteristics (measured from OFF-SA-OFF, double arrow corresponds to first portion of measurement) of a device measured under illumination at different wavelengths for the same photon flux. (b) (filled circles) Dependence of hysteresis charge (taken from data presented in Figure 4.6(a) and (line) absorption coefficient on the energy of the incident photons. 112

4.7 Hysteresis charge versus (a) absorption coefficient and (b) number of absorbed photons for devices of different thickness. 113

4.8 Transfer characteristics (from OFF to ON to OFF) for a device under monochromatic illumination at 460nm and different irradiance values shown on (a) linear and (b) semilog scales. (c) Q_{hyst} taken from transfer characteristics of Figure 4.8(a) measured under different illumination conditions. 115

4.9 Linear regime transfer characteristics for two devices. Black circles are for a device using only SiO_2 as a gate insulator and blue triangles are for a device with the addition of an organic insulator between the SiO_2 and F8T2. 116

4.10 Normalized linear regime transfer characteristics of devices from Figure 4.9 plotted on (a) linear-linear and (b) semi-log scales to allow visual comparison of field-effect mobility, threshold charge and subthreshold swing. 118

5.1 Typical linear regime transfer characteristics taken before and between bias stressing episodes. ΔV_T is defined in this plot as the voltage shift between the extracted threshold voltage before stressing and after stressing to a certain time. 125

5.2 (a) Field-effect mobility and (b) subthreshold swing versus accumulated stress time for a DC accumulation BTS experiment, extracted from the data presented in Figure 5.1. 126

5.3 Typical linear regime transfer characteristics taken before and between DC depletion bias stressing episodes. ΔV_T is defined in this plot as the voltage shift between the extracted threshold voltage before stressing and after stressing to a certain time. 127

5.4 (a) Threshold voltage shift, (b) field-effect mobility and (c) subthreshold swing versus accumulated stress time for a DC depletion BTS experiment, extracted from the data presented in Figure 5.3. 128

5.5 (a) Threshold voltage shift versus accumulated stress time for same OFET stressed at different stress temperatures. (b) Derivative of stretched exponential curves as a function of accumulated stress time, showing peak/inflection point times. 129

5.6 β and τ (taken from the stretched exponential fits) as a function of temperature. . 130

5.7 Arrhenius plot of peak/inflection time constant and τ. 131

5.8 Threshold voltage shift versus normalized stress time for BTS at different stress temperatures. 132

5.9 (a) Threshold voltage shift versus stress energy for BTS different temperatures. (b) Density of traps filled (or states formed) per unit energy as a function of the thermalization energy. 133

5.10 Schematic diagram of gate and drain bias pulse signals used in this work. Note that the dashed line corresponds to the drain-to-source bias pulse signal, the solid line corresponds to the gate-to-source bias pulse signal and $V_{DS} = V_{GS} = 0$ between pulses. 135

5.11 Representative evolution of the transfer characteristics measured during the interruptions of a bias stress performed with an AC gate bias frequency of 10Hz and duty cycles of (a) 50% and (b) 10% . . . 135

5.12 Variation of field-effect mobility taken from the data presented in Figure 5.11(a), as well as for AC BTS measurements performed at a duty cycle of 50 % at other frequencies. . . . 136

5.13 (a) Threshold voltage shift for negative AC (filled symbols) and positive AC (open symbols) BTS, performed using a range of pulse frequencies, plotted versus effective accumulated stress time (i.e., taking into account that for pulsed signals at 50% duty cycle, the effective bias time is half of the total stress time). (b) Threshold voltage shift versus effective accumulated stress time for BTS performed using a range of gate bias stress pulse signal duty cycles. . . . 138

5.14 Threshold voltage shift versus total stress time for BTS performed using a gate bias stress pulse signal with a range of duty cycles. The solid, interpolating line represents a stretched exponential fit to the average of the experimental data. . . . 139

5.15 (a) Linear regime transfer characteristics for device measured at several different temperatures. (b) Threshold voltage and field-effect mobility extracted from data in Figure 5.15(a). (c) Drain current versus drain-to-source bias (for floating gate electrode) measured at different temperatures. . . . 142

6.1 (a) Experimental set-up used to perform the photodischarge measurements. The dashed line around the schematic device structure corresponds to the electromagnetic shield around the probe-station used in the experiment. (b) Timescale of the photodischarge experiments showing the gate bias pulse for t_g, delay time t_d, illumination pulse, resulting current transient $I(t)$and residual charge Q. . . . 149

6.2 Representative set of voltage pulses as observed on the oscilloscope corresponding to the photo-discharging of the remaining filled trap states after the given gate bias application times and a delay time of approximately one second. Similar results were observed for other measurement temperatures. . . . 150

6.3 (a) Extracted residual charge as a function of gate bias application time for a range of gate bias levels at room temperature. The points correspond to the experimentally determined data and the lines are provides as guides to the eye. (b) Extracted residual charge as a function of delay time after a gate bias application at different voltages for 300 sec. The points correspond to the experimentally determined data and the lines correspond to the best least squares fit of the equations given in the text. . . . 152

6.4 The dependence of the fit parameters ((a) E_o and ΔE and (b) ν and Q_o on gate bias. 155

6.5 Residual charge versus gate bias application time for delay time of approximately 3 sec. Points are experimental data and lines are fits that serve as guides to the eye. 156

6.6 (a) Extracted residual charge as a function of delay time after a gate bias application of -50V for 300 sec for the same device measured at different temperatures. The points correspond to the experimentally determined data and the lines correspond to the best least squares fit of the equations given in the text. (b) Extracted residual charge plotted versus the normalized delay time. 157

6.7 The dependence of the fit parameters ((a) E_o and ΔE and (b) ν and Q_o on temperature, points are actual data, lines are guides. 159

6.8 Density of states extracted from the photodischarge measurement described in this paper assuming a normal (Gaussian) distribution of trap states above the valence band. 160

CHAPTER 1

INTRODUCTION

Semiconducting properties of organic materials were first reported in the early 1950's and studies continued through the 1960's mainly focusing on the photogeneration of charge carriers, charge carrier mobility and electroluminescence of organic crystals such as naphthalene, anthracene and tetracene [1–5]. By the mid-1960's and into the 1970's the focus on organic polymers was growing, due to expected synthesis and processing advantages, and the conductivity and charge carrier mobility in doped polymer systems was investigated for photoconductor applications such as xerography [6, 7]. The combined results of this work demonstrated that this interesting class of materials was promising for use in electronic and optoelectronic applications.

Electronic and optoelectronic devices based on conjugated organic semiconductors, in the forms of small molecules as well as polymers, have been the subject of increased research over the past few years. The interest in devices such as organic light-emitting devices (OLEDs) [8–13], organic field-effect transistors (OFETs) [14–20] and organic photodetectors arises from the promise of the availability of a wider range of organic materials and the ability to tune the electronic and optoelectronic properties of the active organic materials, in addition to proposed processing advantages such as [21–24]:

- fabrication at low temperature and over large area;

- deposition from solution and by direct printing;
- use of molecular self-assembly methods.

It is expected that these advantages will allow organic electronic and optoelectronic devices to be used in applications and configurations that are difficult to acheive with inorganic materials, for example in applications requiring large area displays and sensor arrays, fabrication on flexible substrates or curved surfaces.

1.1 Organic semiconductors

Organic materials can be roughly classified into three categories: small molecules, oligomers and polymers. For comparison, the organic small molecules can be considered to be a short, non-repetitive, sequence of covalently-bonded atoms with a carbon backbone and typical molecular weights in the range of several hundred (i.e., $\lesssim 500$), as shown in Figure 1.1(a) and (b). On the other end of the scale, the organic polymers are very large molecules that consist of many repeated units (monomers), with molecular weights in the thousands and greater (i.e., $\gtrsim 2000$), as shown in Figure 1.1(d). The oligomers fall in the range of molecular weights between that of the small molecules and polymers and consist of only a few repeated units, but are generally too short to be considered polymers as shown in Figure 1.1(c). The organic molecules that consist of alternating single and double carbon-carbon bonds are said to be conjugated and one of the simplest cases of an organic polymer, polyacetylene, is shown in Figure. 1.2. The single carbon-carbon bonds are termed σ-bonds and correspond to highly localized electrons on the molecule. The double carbon-carbon bonds consist of a σ-bond, which is again highly localized, and a π-bond, which is formed from the overlap of the p_z atomic orbitals and corresponds to a delocalized π-electron system along the backbone of the molecule. With proper design, conjugated molecules possess the proper molecular orbital energy structure to result in an

energy gap between a filled π-band (i.e., Highest Occupied Molecular Orbital, or HOMO) and an empty π-band (i.e., Lowest Unoccupied Molecular Orbital, or LUMO) as shown in Figure 1.3(a). This energy gap is termed the HOMO-LUMO gap and is in the range of approximately 1 to 4 eV, corresponding to a wide range of optical energies. In general, we can make the rough assumption that the HOMO level, LUMO level and the HOMO-LUMO gap roughly correspond to the top of the valence band, bottom of the conduction band and the energy band gap of crystalline inorganic materials.

It is important (and interesting) to note the main differences between the crystalline

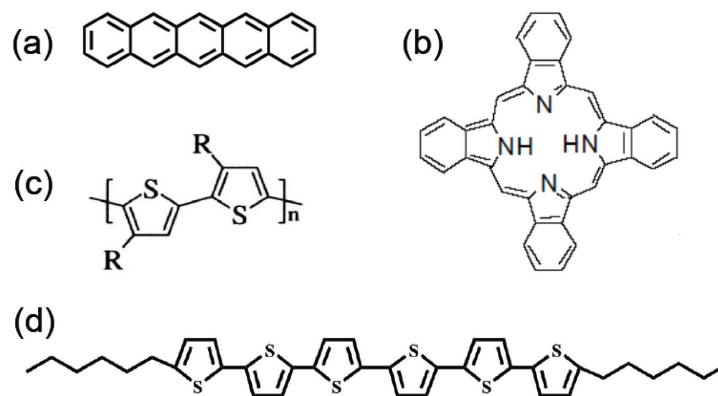

Figure 1.1: Chemical structure of the organic molecules (a) pentacene, (b) tetrabenzoporphyrin (c) sexithiophene and (d) poly-3-hexylthiophene.

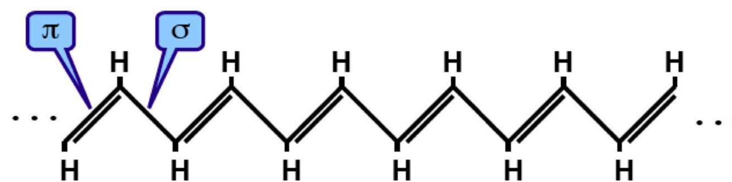

Figure 1.2: Chemical structure of the organic polymer polyacetylene describing the alternating double- (π) and single- (σ) carbon-carbon bonds.

inorganic semiconductors, such as Si and GaAs, and the conjugated organic semiconductors, such as pentacene and F8T2 [poly(9,9-dioctylfluorene-co-bithiophene)] alternating copolymer from the Dow Chemical Company. Crystalline inorganic semiconductors are

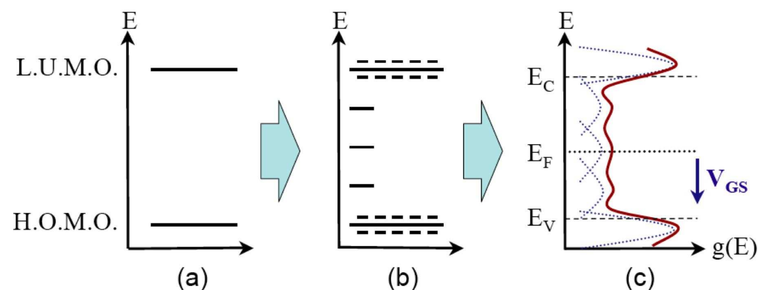

Figure 1.3: (a) Energy levels of a single molecule demonstrating the Highest Occupied Molecular Orbital and Lowest Unoccupied Molecular Orbital. (b) Schematic intermediate range of an amorphous conglomeration of several molecules and the corresponding broadening of the molecular orbitals and breaking of conjugation that leads to allowed states within the energy gap. (c) Schematic density of states for an amorphous film of an organic (or inorganic) semiconductor showing the band edges (band-tails) as well as the allowed states within the gap.

characterized by a three-dimensional network in which the atoms are all connected by covalent bonds with bonding energies on the order of 75kcal/mole (for Si–Si bonds) [25]. The semiconductivity of the material arises as a property of the entire system and the conduction and valence bands are relatively wide due to the strong interatomic bonds, resulting in numerous delocalized states and a relatively high charge carrier mobility. By contrast, for the case of the conjugated organic semiconductors, the intermolecular forces are weak van der Waal forces with typical energies of 10kcal/mole. Since the energies of these interactions are relatively weak, the electronic properties of the organic material arise mostly from the properties of the individual molecule. Another consequence of the weak intermolecular interactions is that the energy bands resulting from the interaction of the collective LUMO levels, as well as the collective HOMO levels, is relatively narrow, resulting in charge transport that is mostly limited by transport via localized states and a relatively low charge carrier mobility, as shown schematically by the density of states of the organic thin-film presented in Figure 1.3(c). The charge transport in conjugated organic materials occurs through both intramolecular and intermolecular processes

and is described in more detail below. The main ideas that can lead to enhancement of the charge transport properties of conjugated organic semiconductors are that of extended π-conjugation and π-stacking and refer to the degrees of conjugation and crystallinity of the organic material, respectively. For example, fused ring polymeric derivatives based on aromatic and/or heteroaromatic molecules can provide molecular geometries that are more planar and can lead to more extended ground state conjugation [26]. Additionally, the planarity of the molecules allows for better organization of the molecules, reducing the molecular separation and strengthening the intermolecular interactions, and thereby enhancing charge carrier transport.

For the case of conjugated organic small molecules, pentacene is by far the most studied and its chemical structure is shown in Figure 1.1(a) [27–39]. In general, pentacene exhibits p-type semiconducting behavior with field-effect hole mobilities in excess of 0.1cm^2/Vs and approaching that of hydrogenated amorphous silicon. Several groups have reported n-type transistor action from vacuum sublimed or evaporated [40–42] and solution deposited small molecules [43]. Recently, solution-processible porphyrin-based organic molecules have been of interest, namely tetrabenzoporphyrin shown in Figure 1.1(b) [44, 45].

In general, it has been observed that the majority of the organic semiconductors, especially in the form of polymers, present hole mobilities ($\approx 10^{-2}$ cm^2/Vsec) much greater than electron mobilities, i.e., p-type transistor action is much easier to observe than n-type transistor action. However, recently it has been demonstrated by Chua, et al., that this observation is often misleading. With the use of source and drain electrodes with the proper work function and especially with the use of a hydroxyl-free gate dielectric, n-type transistor action (i.e., appreciable electron mobility approaching $\approx 10^{-2}$ cm^2/Vsec) is observed [46]. Chua explained that the reduction of electron mobility in the studied materials

is due to the trapping of electrons at the gate dielectric interface by the hydroxyl groups of the gate dielectric when insulators such as SiO_2 are used.

Conjugated copolymers, such as F8T2, demonstrate the usefulness of organic semiconductors in that they are synthesized from a combination of two (or more) different monomers in order to create a molecule with certain energetic and morphological characteristics. In general, synthesizing materials to achieve certain desired characteristics can result in materials with properties such as light emission or absorption with a specific spectrum, enhanced transport of a specific charge species, enhanced environmental stability, processing from solution, etc. In the case of F8T2, the molecule is co-polymerized, using the "Suzuki reaction" from two monomers: 9,9-dioctylfluorene alternating with dithiophene [47–50]. The resulting molecules are of the "hairy rod" type, with weight averaged molecular weights (M_w) between 30 and 150 kg/mol and thermotropic, nematic liquid crystalline properties. The glass transition (T_g) and liquid crystal transition (T_{XL-N}) generally occur around 130°Cand 265°C, respectively [52]. The liquid crystalline properties of F8T2 have allowed several groups to demonstrate an enhancement of the charge carrier mobility by enhancing the crystallinity of the material (i.e., increasing π-stacking), as well as through the alignment of the molecules with respect to the channel of the device [49, 51–53].

As mentioned above, solution deposition and processing of high-quality conjugated organic semiconductors is also a major goal and proposed advantage over crystalline inorganic semiconductors. So far, F8T2 has proved that this is not an empty promise. Several groups have shown that an F8T2 ink can be used with advanced inkjet printers and working electronic circuits can be fabricated [50, 54–56].

1.2 Outline of this thesis

The electrical performance of electronic devices based on this unique class of conjugated organic semiconductors, such as organic field-effect transistors (OFETs) has steadily increased over the past several years [21–23,56–59]. This increase can be attributed to the development of high quality organic semiconductors and engineering of device structures and fabrication methods, as well as to the progress made in understanding the underlying physics of organic materials and devices. One important factor in the development of this class of materials and devices is the ability to reliably compare the various performance parameters (i.e., field-effect mobility, threshold voltage and ON/OFF ratio) extracted by different research groups and for different devices. The first topic of this thesis, presented in Chapter 2, is a discussion and development of the methods used to extract the field-effect mobility from the transfer characteristics of organic (polymer) field-effect transistors. We discuss the limitations of and problems with the use of the conventional extraction methods. We show that some of these limitations can be overcome by taking into account the dispersive nature of charge transport through an amorphous semiconductor, which leads to a gate-bias dependence of the charge carrier mobility (i.e., field-effect mobility). Taking this dependence into account allows for a more reliable and reproducible parameter extraction method.

Additionally, since many of the proposed uses of OFETs will involve the purposeful or possible exposure of the device to light (i.e., as a sensor in a photodetector array or as driving circuitry in active matrix displays), it is important to understand the effects, as well as the underlying physics, of illumination on the electrical performance of these devices. The second topic of this thesis, presented in Chapter 3 is our study of the electrical performance of OFETs exposed to both broadband and monochromatic illumination.

An interesting application of organic semiconducting materials is in photodetectors. These detectors can be classified into two main groups: two-terminal photodiodes and three-terminal phototransistors. A number of groups have described conjugated organic polymer-based photodiodes in various configurations and excellent reviews can be found in [60–62]. Several groups have discussed organic photodiode structures utilizing a blend of different polymers [63], incorporating a composite of a small molecule (such as C_{60}) and a polymer [64–67], using a multilayer structure composed of alternating layers of various polymers [68], in a microcavity [69], and combined with hydrogenated amorphous silicon (a-Si:H) thin-film transistor (TFT) addressing [70]. Still other groups have reported two-terminal photodetectors in a lateral configuration based on a self-assembled layer of a DNA derivative [71] and which have been optimized for optical detection in the near infrared [72].

However, a much smaller number of groups have demonstrated the effects of illumination on the electrical performance of three-terminal, polymer-based OFETs or the use of these devices as photosensors, which is also described in Chapter 3. Zukawa, et al., have demonstrated an organic heterojunction-based phototransistor [73]. Schön and Klock have shown the use of a pentacene-based metal-semiconductor field-effect transistor as a phototransistor [74]. Additionally, Narayan, et al., have described, in limited detail, an organic polymer field-effect transistor that responds to light [75, 76]. In this chapter, the performance of our gate-planarized OFET as a photodetector is described.

Before devices such as OFETs can be commercialized and integrated into applications such as smart cards and flat-panel displays, it is important that the non-idealities and instabilities of the devices be understood and brought under control. Currently, the device-to-device reproducibility of organic electronics is relatively poor, compared to that of other thin-film and bulk/crystalline electronic devices (such as hydrogenated amorphous

silicon and silicon, respectively). Additionally, it has been observed that organic thin-film transistors can exhibit significant non-idealities in the measured electrical characteristics. Specifically, the electrical characteristics can be significantly different depending on both the electrical characteristics sweep direction (i.e., OFF-to-ON or ON-to-OFF) and on the previous state of the device (i.e., if the device was biased into the ON-state for a certain amount of time before the electrical characteristics were measured). These effects, which are attributed to localization of charge carriers, which leads to changes in the threshold (or turn-on) voltage of the device, are described in the next two chapters of this thesis. Namely, the hysteresis in the measured electrical characteristics is discussed in Chapter 4 and the instabilities of OFETs, studied through the use of bias-temperature stress (BTS), are discussed in Chapter 5. We also demonstrate that the hysteresis can be eliminated from the electrical characteristics of our devices by incorporating an intermediate organic insulator layer between an inorganic insulator and the organic semiconductor layers. We have performed negative/positive, DC/AC BTS and analyzed the results with theory developed for bias stress effects in amorphous semiconductors. From the BTS work, we extract a form of the density of states of the active organic semiconductor layer and relate it to the experimentally observed instabilities of the OFETs.

Finally, the subject of Chapter 6 is our characterization of the density of trap states within the polymer active layer. This characterization has been performed by the use of an interesting experimental technique, the photodischarge measurement, in which after forcing charge carriers to be trapped into the localized states within the channel layer of the device and after waiting a certain delay time, the residual trapped charge is probed with an illumination pulse. By performing the fits described in this chapter, we are able to study the kinetics of the trap states and characterize the density and energetic distribution of the trap states of the active organic semiconductor layer. These results are compared to, and

found to be very consistent with, the results from the other chapters of this work.

This thesis concludes with Chapter 7, where the major conclusions derived from the work of this thesis are summarized. Several ideas regarding possible future work and directions are also briefly discussed in the concluding chapter.

References

[1] H. Mette and H. Pick, *Z. Physik*, vol. 134, p. 566, 1953.

[2] R. G. Kepler, "Charge carrier production and mobility in anthracene crystals," *Phys. Rev.*, vol. 119, pp. 1226–1229, 1960.

[3] O. H. LeBlanc, "Hole and electron drift mobilities in anthracene," *J. Chem. Phys.*, vol. 33, p. 626, 1960.

[4] M. Pope, H. P. Kallmann, and P. Magnante, "Electroluminescence in organic crystals," *J. Chem. Phys.*, vol. 38, pp. 2042–2043, 1963.

[5] W. Helfrich and W. G. Schneider, "Recombination radiation in anthracene crystals," *Phys. Rev. Lett.*, vol. 14, pp. 229–231, 1965.

[6] H. Hoegl, "On photoelectric effects in polymers and their sensitization by dopants," *J. Phys. Chem.*, vol. 69, pp. 755–766, 1965.

[7] C. K. Chiang, C. R. F. Jr., Y. W. Park, A. J. Heeger, H. Shirakawa, E. J. Louis, S. C. Gau, and A. C. MacDiarmid, "Electrical conductivity in doped polyacetylene," *Phys. Rev. Lett.*, vol. 39, pp. 1098–1101, 1977.

[8] P. S. Vincett, W. A. Barlow, R. A. Hann, and G. G. Roberts, "Electrical conduction and low voltage blue electroluminescence in vacuum-deposited organic films," *Thin Solid Films*, vol. 94, pp. 171–183, 1982.

[9] C. W. Tang, "Two-layer organic photovoltaic cell," *Appl. Phys. Lett.*, vol. 48, pp. 183–185, 1986.

[10] C. W. Tang and S. A. VanSlyke, "Organic electroluminescent diodes," *Appl. Phys. Lett.*, vol. 51, pp. 913–915, 1987.

[11] C. W. Tang, S. A. VanSlyke, and C. H. Chen, "Electroluminescence of doped organic thin films," *J. Appl. Phys.*, vol. 85, pp. 3610–3616, 1989.

[12] J. H. Burroughes, D. D. C. Bradley, A. R. Brown, R. N. Marks, K. Mackay, R. H. Friend, P. L. Burns, and A. B. Holmes, "Light-emitting diodes based on conjugated polymers," *Nature*, vol. 347, pp. 539–541, 1990.

[13] A. R. Brown, D. D. C. Bradley, J. H. Burroughes, R. H. Friend, N. C. Greenham, P. L. Burns, A. B. Holmes, and A. Kraft, "Poly(p-phenylenevinylene) light-emitting diodes: Enhanced electroluminiscent efficiency through charge carrier confinement," *Appl. Phys. Lett.*, vol. 61, pp. 2793–2795, 1992.

[14] J. H. Burroughes, C. A. Jones, and R. H. Friend, “New semiconductor device physics in polymer diodes and transistors,” *Nature*, vol. 335, pp. 137–141, 1988.

[15] R. Madru, G. Guillaud, M. al Sadoun, M. Maitrot, J.-J. André, J. Simon, and R. Even, “A well-behaved field effect transistor based on an intrinsic molecular semiconductor,” *Chem. Phys. Lett.*, vol. 145, pp. 343–346, 1988.

[16] C. Clarisse, M. T. Riou, M. Gauneau, and M. le Contellec, “Field-effect transistor with diphthalocyanine thin film,” *Electron. Lett.*, vol. 24, pp. 674–675, 1998.

[17] A. Tsumura, H. Koezuka, and T. Ando, “Polythiophene field-effect transistor: Its characteristics and operation mechanism,” *Synth. Met.*, vol. 25, pp. 11–23, 1988.

[18] A. Assadi, C. Svensson, M. Willander, and O. Inganäs, “Field-effect mobility of poly(3-hexylthiophene),” *Appl. Phys. Lett.*, vol. 53, pp. 195–197, 1988.

[19] G. Horowitz, D. Fichou, X. Peng, Z. Xu, and F. Garnier, “A field-effect transistor based on conjugated alpha-sexithienyl,” *Solid State Commun.*, vol. 72, pp. 381–384, 1989.

[20] F. Garnier, R. Hajlaoui, A. Yassar, and P. Srivastava, “All-polymer field-effect transistor realized by printing techniques,” *Science*, vol. 265, pp. 1684–1686, 1994.

[21] C. D. Dimitrakopoulos and D. J. Mascaro, “Organic thin-film transistors: A review of recent advances,” *IBM J. Res. and Dev.*, vol. 45, pp. 11–27, 2001.

[22] G. Horowitz, “Organic field-effect transistors,” *Adv. Mater.*, vol. 10, pp. 365–377, 1998.

[23] T. N. Jackson, Y. Lin, D. J. Gundlach, and H. Klauk, “Organic thin-film transistors for organic light-emitting flat-panel display backplanes,” *IEEE J. Select. Topics Quantum Electron.*, vol. 4, pp. 100–104, 1998.

[24] H. Sirringhaus, N. Tessler, and R. H. Friend, “Integrated optoelectronic devices based on conjugated polymers,” *Science*, vol. 280, pp. 1741–1743, 1998.

[25] F. Garnier, G. Horowitz, D. Fichou, and A. Yassar, “Role of mesoscopic molecular organization in organic-based thin film transistors,” *Supramol. Sci.*, vol. 4, pp. 155–162, 1997.

[26] P. Coppo and M. L. Turner, “Cyclopentadithiophene based electroactive materials,” *J. Mater. Chem.*, vol. 15, pp. 1123–1133, 2005.

[27] A. Afzali, C. D. Dimitrakopoulos, and T. O. Graham, “Photosensitive pentacene precursor: Synthesis, photothermal patterning, and application in thin-film transistors,” *Adv. Mater.*, vol. 15, pp. 2066–2069, 2003.

[28] V. Y. Butko, X. Chi, D. V. Lang, and A. P. Ramirez, “Field-effect transistor on pentacene single crystal,” *Appl. Phys. Lett.*, vol. 83, pp. 4773–4775, 2003.

[29] D. J. Gundlach, Y. Y. Lin, T. N. Jackson, S. F. Nelson, and D. G. Schlom, “Pentacene organic thin-film transistors - molecular ordering and mobility,” *IEEE Electron Device Lett.*, vol. 18, pp. 87–89, 1997.

[30] H. Klauk, M. Halik, U. Zschieschang, G. Schmid, W. Radlik, and W. Weber, “High-mobility polymer gate dielectric pentacene thin film transistors,” *J. Appl. Phys.*, vol. 92, pp. 5259–5263, 2002.

[31] D. Knipp, R. A. Street, A. Völkel, and J. Ho, "Pentacene thin film transistors on inorganic dielectrics: Morphology, structural properties, and electronic transport," *J. Appl. Phys.*, vol. 93, pp. 347–355, 2003.

[32] T. Kodzasa, M. Yoshida, S. Uemura, and T. Kamata, "Memory effects of pentacene mfs-fet," *Synth. Met.*, vol. 137, pp. 943–944, 2003.

[33] T. Komoda, K. Kita, K. Kyuno, and A. Toriumi, "Performance and degradation in single grain-size pentacene thin-film transistors," *Jpn. J. Appl. Phys.*, vol. 42, pp. 3662–3665, 2003.

[34] J. G. Laquindanum, H. E. Katz, A. J. Lovinger, and A. Dodabalapur, "Morphological origin of high mobility in pentacene thin-film transistors," *Chem. Mater.*, vol. 8, pp. 2542–2544, 1996.

[35] M. J. Panzer, C. R. Newman, and C. D. Frisbie, "Low-voltage operation of a pentacene field-effect transistor with a polymer electrolyte gate dielectric," *Appl. Phys. Lett.*, vol. 86, p. 103503, 2005.

[36] R. A. Street, D. Knipp, and A. R. Völkel, "Hole transport in polycrystalline pentacene transistors," *Appl. Phys. Lett.*, vol. 80, pp. 1658–1660, 2002.

[37] M. L. Swiggers, G. Xia, J. D. Slinker, A. A. Gorodetsky, G. G. Malliaras, R. L. Headrick, B. T. Weslowski, R. N. Shashidhar, and C. S. Dulcey, "Orientation of pentacene films using surface alignment layers and its influence on thin-film transistor characteristics," *Appl. Phys. Lett.*, vol. 79, pp. 1300–1302, 2001.

[38] A. R. Völkel, R. A. Street, and D. Knipp, "Carrier transport and density of state distributions in pentacene transistors," *Phil. Rev. B*, vol. 66, p. 195336, 2002.

[39] S. Yaginuma, J. Yamaguchi, K. Itaka, and H. Koinuma, "Pulsed laser deposition of oxide gate dielectrics for pentacene organic field-effect transistors," *Thin Solid Films*, vol. 486, pp. 218–221, 2005.

[40] J. G. Laquindanum, H. E. Katz, A. Dodabalapur, and A. J. Lovinger, "n-channel organic transistor materials based on naphthalene frameworks," *J. Am. Chem. Soc.*, vol. 118, pp. 11 331–11 332, 1996.

[41] P. R. L. Malenfant, C. D. Dimitrakopoulos, J. D. Gelorme, L. L. Kosbar, T. O. Graham, A. Curioni, and W. Andreoni, "N-type organic thin-film transistor with high field-effect mobility based on a n,n'-dialkyl-3,4,9,10-perylene tetracarboxylic diimide derivative," *Appl. Phys. Lett.*, vol. 80, pp. 2517–2519, 2002.

[42] B. A. Paez, M. Bartzsch, G. Salvan, R. Scholz, T. U. Kampen, and D. R. T. Zahn, "Combined electrical and raman characterization of c_{60} based organic field effect transistors," *Proc. of SPIE*, vol. 5217, pp. 63–70, 2003.

[43] C. Waldauf, P. Schilinsky, M. Perisutti, J. Hauch, and C. J. Brabec, "Solution-processed organic n-type thin-film transistors," *Adv. Mater.*, vol. 15, pp. 2084–2088, 2003.

[44] P. B. Shea, A. R. Johnson, N. Ono, and J. Kanicki, "Electrical properties of staggered electrode, solution-processed, polycrystalline tetrabenzoporphyrin field-effect transistors," *IEEE Trans. Electron Devices*, vol. 52, pp. 1497–1503, 2005.

[45] P. B. Shea, J. Kanicki, and N. Ono, "Field-effect mobility of polycrystalline tetrabenzoporphyrin thin-film transistors," *J. Appl. Phys.*, vol. 98, p. 014503, 2005.

[46] L.-L. Chua, J. Zaumseil, J.-F. Cheng, E. C.-W. Ou, P. K.-H. Ho, H. Sirringhaus, and R. H. Friend, "General observation of n-type field-effect behaviour in organic semiconductors," *Nature*, vol. 434, pp. 194–199, 2005.

[47] N. Miyaura, T. Yanagi, and A. Suzuki, "The palladium?catalyzed cross?coupling reaction of phenylboronic acid with haloarenes in the presence of bases," *Synth. Commun.*, vol. 11, pp. 513–519, 1981.

[48] M. Inbasekaran, W. Wu, and E. P. Woo, "Process for preparing conjugated polymers," Patent.

[49] M. Grell, M. Redecker, K. S. Whitehead, D. D. C. Bradley, M. Inbasekaran, E. P. Woo, and W. Wu, "Monodomain alignment of thermotropic fluorene copolymers," *Liquid Crystals*, vol. 26, pp. 1403–1407, 1999.

[50] D. J. Brennan, P. H. Townsend, D. M. Welsh, M. G. Dibbs, J. M. Shaw, J. Miklovich, R. B. Boeke, A. C. Arias, L. Creswell, J. D. MacKenzie, C. Ramsdale, A. Menon, and H. Sirringhaus, "Polyfluorenes as organic semiconductors for polymeric field effect transistors," *Proc. SPIE*, vol. 5217, pp. 1–6, 2003.

[51] H. Sirringhaus, R. J. Wilson, R. H. Friend, M. Inbasekaran, W. Wu, E. P. Woo, M. Grell, and D. D. C. Bradley, "Mobility enhancement in conjugated polymer field-effect transistors through chain alignment in a liquid-crystalline phase," *Appl. Phys. Lett.*, vol. 77, pp. 406–408, 2000.

[52] L. Kinder, J. Kanicki, and P. Petroff, "Structural ordering and enhanced carrier mobility in organic polymer thin film transistors," *Synth. Met.*, vol. 146, pp. 181–185, 2004.

[53] S. P. Li, C. J. Newsome, D. M. Russell, T. Kugler, M. Ishida, and T. Shimoda, "Friction transfer deposition of ordered conjugated polymer nanowires and transistor fabrication," *Appl. Phys. Lett.*, vol. 87, p. 062101, 2005.

[54] T. Kawase, H. Sirringhaus, R. H. Friend, and T. Shimoda, "Inkjet printed via-hole interconnections and resistors for all-polymer transistor circuits," *Adv. Mater.*, vol. 13, pp. 1601–1605, 2001.

[55] B.-J. de Gans, P. C. Duineveld, and U. S. Schubert, "Inkjet printing of polymers: State of the art and future development," *Adv. Mater.*, vol. 16, pp. 203–213, 2004.

[56] A. Salleo, W. S. Wong, M. L. Chabinyc, K. E. Paul, and R. A. Street, "Polymer thin-film transistor arrays patterned by stamping," *Adv. Funct. Mater.*, vol. 15, pp. 1105–1110, 2005.

[57] S. Martin, J. Y. Nahm, and J. Kanicki, "Gate-planarized organic polymer thin-film transistors," *J. Electron. Mater.*, vol. 31, pp. 512–519, 2002.

[58] S. Martin, M. C. Hamilton, and J. Kanicki, "Organic polymer thin-film transistors for active-matrix flat panel displays?" *J. SID.*, vol. 11, pp. 543–549, 2003.

[59] Y. Wu, P. Liu, B. S. Ong, T. Srikumar, N. Zhao, G. Botton, and S. Zhu, "Controlled orientation of liquid-crystalline polythiophene semiconductors for high-performance organic thin-film transistors," *Appl. Phys. Lett.*, vol. 86, p. 142102, 2005.

[60] S. R. Forrest, “Active optoelectronics using thin-film organic semiconductors,” *IEEE J. Select. Topics Quantum Electron.*, vol. 6, pp. 1072–1083, 2000.

[61] P. Peumans, A. Yakimov, and S. R. Forrest, “Small molecular weight organic thin-film photodetectors and solar cells,” *J. Appl. Phys.*, vol. 93, pp. 3693–3723, 2003.

[62] D. Natali and M. Sampietro, “Detectors based on organic materials: status and perspectives,” *Nuc. Inst. and Meth. A*, vol. 512, pp. 419–426, 2003.

[63] J. Y. Park, H. M. Le, G. T. Kim, H. Park, Y. W. Park, I. N. Kang, D. H. Hwang, and H. K. Shim, “The electroluminescent and photodiode device made of a polymer blend,” *Synth. Met.*, vol. 79, pp. 177–181, 1996.

[64] J. Gao, F. Hide, and H. Wang, “Efficient photodetectors and photovoltaic cells from composites of fullerenes and conjugated polymers: photoinduced electron transfer,” *Synth. Met.*, vol. 84, pp. 979–980, 1997.

[65] K. S. Narayan and T. B. Singh, “Nanocrystalline titanium dioxide-dispersed semiconducting polymer photodetectors,” *Appl. Phys. Lett.*, vol. 74, pp. 3456–3458, 1999.

[66] G. Yu, Y. Cao, J. Wang, J. McElvain, and A. J. Heeger, “High sensitivity polymer photosensors for image sensing applications,” *Synth. Met.*, vol. 102, pp. 904–907, 1999.

[67] G. Yu, G. Srdanov, J. Wang, H. Wang, Y. Cao, and A. J. Heeger, “Large area, full-color, digital image sensors made with semiconducting polymers,” *Synth. Met.*, vol. 111-112, pp. 133–137, 2000.

[68] P. Peumans, V. Bulović, and S. R. Forrest, “Efficient, high-bandwidth organic multilayer photodetectors,” *Appl. Phys. Lett.*, vol. 76, pp. 3855–3857, 2000.

[69] J. M. Lupton, R. Koeppe, J. G. Müller, J. Feldmann, U. Scherf, and U. Lemmer, “Organic microcavity photodiodes,” *Adv. Mater.*, vol. 15, pp. 1471–1474, 2003.

[70] R. A. Street, J. Craham, Z. D. Popovic, A. Hor, S. Ready, and J. Ho, “Image sensors combining an organic photoconductor with a-Si:H matrix addressing,” *J. Non-Cryst. Solids*, pp. 1240–1244, 2002.

[71] R. Rinaldi, E. Branca, R. Cingolani, S. Masiero, G. P. Spada, and G. Gottarelli, “Photodetectors fabricated from a self-assembly of a deoxyguanosine derivative,” *Appl. Phys. Lett.*, vol. 78, pp. 3541–3543, 2001.

[72] D. Natali, M. Sampietro, M. Arca, C. Denotti, and F. A. Devillanova, “Wavelength-selective organic photodetectors for near-infrared applications based on novel neutral dithiolenes,” *Synth. Met.*, vol. 137, pp. 1489–1490, 2003.

[73] T. Zukawa, S. Naka, H. Okada, and H. Onnagawa, “Organic heterojunction phototransistor,” *J. Appl. Phys.*, vol. 91, pp. 1171–1174, 2002.

[74] J. H. Schön and C. Kloc, “Organic metal-semiconductor field-effect phototransistors,” *Appl. Phys. Lett.*, vol. 78, pp. 3538–3540, 2001.

[75] K. S. Narayan, A. G. Manoj, T. B. Singh, and A. A. Alagiriswamy, “Novel strategies for polymer based light sensors,” *Thin Solid Films*, vol. 417, pp. 75–77, 2002.

[76] K. S. Narayan and N. Kumar, "Light responsive polymer field-effect transistor," *Appl. Phys. Lett.*, vol. 79, pp. 1891–1893, 2001.

CHAPTER 2

DC CHARACTERISTICS OF PF-BASED OFETS

In this chapter, the structure of the device used in all of the experiments in this thesis is described. Next, the DC operation and electrical performance parameter extraction methods and models of polyfluorene-based organic field-effect transistors (OFETs) are discussed. We present a method of extracting the field-effect mobility from the transfer characteristics of OFETs, in both the linear and saturation regimes, by accounting for the dependence of the mobility on the gate bias, which translates to a dependence on the accumulated density of majority charge carriers in the channel. This method is compared to the commonly used extraction methods, which are based on the standard MOSFET square-law drain current equations that do not account for the variation of mobility with the applied gate bias. We show that by using the standard MOSFET equations, the extracted field-effect mobility can be significantly overestimated. We also demonstrate the use of the proposed method to extract the field-effect mobility at different measurement temperatures, as well as the dependence of the extracted parameters on temperature. Additionally, the contact resistance and intrinsic device performance are investigated through the use of the transverse line method (TLM). Finally, the performance of these devices under high gate-to-source and drain-to-source electric fields is presented.

2.1 Device structure

A schematic cross-section of the device used in this study is shown in Figure 2.1(a), along with a TEM cross-section in Figure 2.1(b). A top-view of one device is shown in Figure 2.1(c). The device is an inverted, defined-gate, gate-planarized, coplanar thin-film transistor [1–3]. Indium tin oxide (ITO) was used for the source and drain contacts, benzocyclobutene (BCB) was used as the gate-planarization layer and also functions as a gate insulator, PECVD hydrogenated amorphous silicon nitride (a-SiN:H) was used as a second gate insulator layer, and chromium (Cr) was used for the patterned gate electrode. For the case of these devices, the usefulness of the BCB planarization layer is limited. However, if a thicker gate electrode is to be used, the planarization will allow for better step coverage of the subsequently deposited layers [4]. The devices were fabricated on a silicon substrate (with a thick, thermally grown silicon dioxide layer) to facilitate processing in standard microelectronic fabrication equipment; however, this device structure could easily be fabricated on a transparent glass or flexible plastic substrate. We used a 1wt% solution of the organic semiconductor F8T2 [poly(9,9-dioctylfluorene-co-bithiophene)] alternating copolymer dissolved in either xylenes or mesitylenes. F8T2 is described in more detail in the following section. The polymer film was deposited by spin-coating and cured in a vacuum oven at 90°C, providing a uniform and unpatterned film with an approximate thickness of 1000Å. By ”curing”, we mean that the solvent in which the F8T2 was dissolved was driven out of the film by heating the sample in a vacuum. The reproducibility from sample-to-sample and the lack of a change in device performance for devices that have been used over many months provide evidence that the solvent is completely driven out of the film through this process, since we would expect a change in device performance over time if the solvent was not completely removed in the initial processing of the

devices. Samples are stored in air, at room temperature under yellow ambient light.

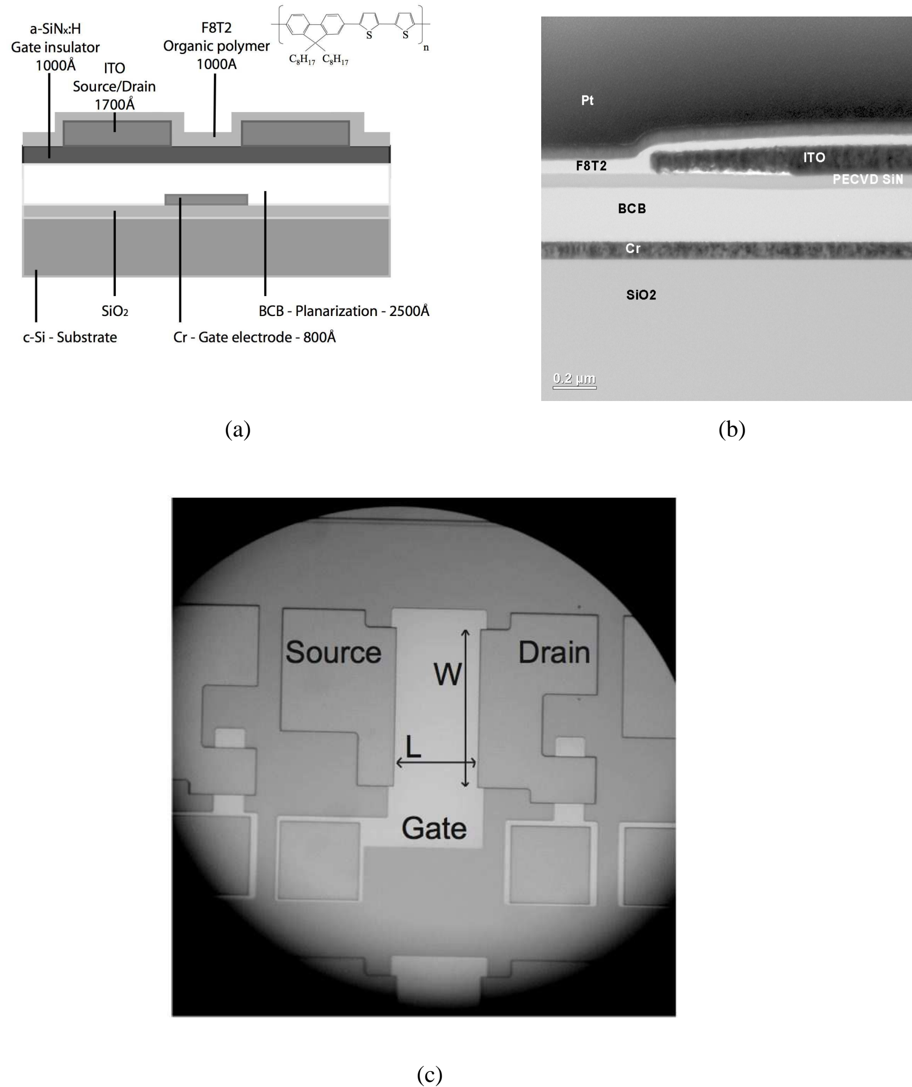

(a) (b)

(c)

Figure 2.1: (a) Cross-section of device structure and chemical structure of F8T2. (b) TEM cross-section of device structure courtesy of Elvin Beach, Steve Rozeveld, and Charlie Wood of the Dow Chemical Company. (c) Top-view of device showing gate, source, and drain. For this device, L = 56μm, W = 116μm and source/drain-gate overlap is 5μm.

2.2 DC operation and measurement

OFETs based on F8T2 exhibit p-channel field-effect transistor behavior (i.e., holes are accumulated within the channel) as can be seen from the output characteristics (drain current versus drain-to-source voltage, $I_D - V_{DS}$) shown in Figure 2.2(a). As expected, for

field-effect transistors, the output characteristics show two distinct regions of device operation: linear and saturation. The non-ideal behavior of the device in the linear regime (at low V_{DS}) is most likely due to the current crowding associated with the contact resistance between the polymer channel and the source and drain electrodes [5]. The linear regime transfer characteristics (drain current versus gate-to-source voltage, $I_D - V_{GS}$) of a device in the dark are presented in Figure 2.2(b).

2.2.1 Measurement setup

The transfer characteristics (drain current versus gate-to-source voltage, $I_D - V_{GS}$) of the OFET were measured in the dark, at various temperatures using a Karl Suss PM8 probe station, and an HP4156 semiconductor parameter analyzer controlled by Interactive Characterization Software (Metrics). For the transfer characteristic measurements performed in this study, we measured the devices from the strong accumulation (i.e., ON-state) to the OFF-state, as is commonly done. Transfer characteristic measurements performed in this manner provide more manageable results, since any non-ideal effects that depend on the applied gate bias, which would gradually accumulate for the case of measurement from the OFF-state to the ON-state, occur immediately and completely at the start of the measurement from the ON-state to the OFF-state. A Signatone QuietTemp temperature controller and hot-chuck were used to control the temperature of the devices between 10°C and 80°C. Except where specified, all measurements were performed in the dark and in ambient atmosphere.

The typical bias conditions used to measure the transfer characteristics, in both the linear and saturation regimes, and the output characteristics of the devices, are given in Table 2.1. We chose to measure the transfer characteristics from the ON-state to the OFF-state (i.e., from $V_{GS} = -40V$ to $20V$), as shown in Table 2.1. This measurement method was

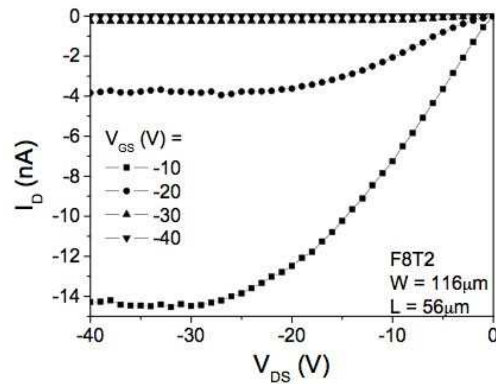

(a)

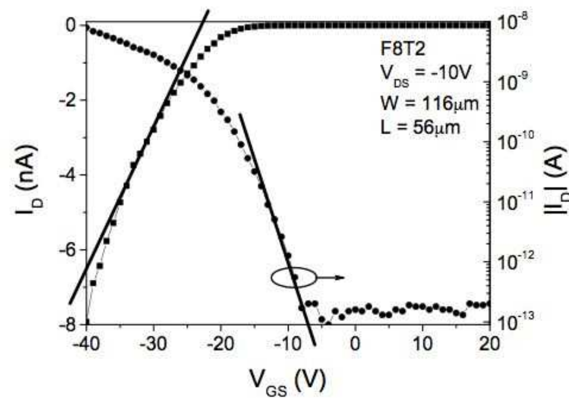

(b)

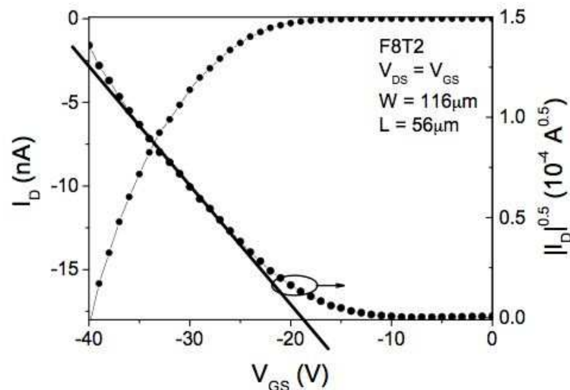

(c)

Figure 2.2: (a) Output characteristics of an OFET with L = 16μm, W = 56μm, source/drain-gate overlap of approximately 5μm (b) Linear regime ($V_{DS} < V_{GS} - V_T$) transfer characteristics of same OFET. Lines are fits to equations (2.2) and (2.4). (c) Saturation regime ($V_{DS} \approx V_{GS} - V_T$) transfer characteristics of same OFET.

chosen because it provides very reproducible data, with a variation in the ON-current of less than ±5% for the linear regime transfer characteristics measured back-to-back in the dark. This allows reliable comparison of the electrical performance of the device under various measurement conditions. The standard method used to extract the linear regime

Table 2.1: OFET Electrical Characteristics Measurement Bias Conditions

Transfer Characteristics		
V_G	Initial	$-40V$
	Final	$20V$
	Step	$+1V$
V_D	Linear	$-5V or -10V$
	Saturation	V_G
V_S	Common	$0V$
Output Characteristics		
V_G	$-40, -30, -20, -10V$	
V_D	Initial	$0V$
	Final	$-40V$
	Step	$-1V$
V_S	Common	$0V$

field-effect mobility and threshold voltage from the linear regime transfer characteristics uses the following equation, based on the MOSFET gradual channel approximation [6]:

$$I_D = -\mu_{FElin} C_{ins} \frac{W}{L} \left[(V_{GS} - V_{Tlin}) V_{DS} - \frac{V_{DS}^2}{2} \right] \tag{2.1}$$

or, for low V_{DS}:

$$I_D = -\mu_{FElin} C_{ins} \frac{W}{L} (V_{GS} - V_{Tlin}) V_{DS} \tag{2.2}$$

In these equations, μ_{FElin} is the linear regime field-effect mobility (cm^2/Vs), C_{ins} is the gate insulator capacitance per unit area (F/cm^2), W is the channel width of the device, L is the channel length of the device, V_{GS} is the applied gate-to-source bias, V_{DS} is the applied drain-to-source bias, and V_{Tlin} is the linear regime threshold voltage given by the following

equations for MOSFETs [7]:

$$V_{Tlin} = 2\phi_F - \frac{\epsilon_{semi}}{\epsilon_{ins}} d_{ins} \sqrt{\frac{4qN_A^{eff}}{\epsilon_{semi}\epsilon_{ins}}(-\phi_F)} + V_{FB}^{eff} \tag{2.3a}$$

$$V_{FB}^{eff} = \phi_{MS} - \frac{Q_{eff}}{C_{ins}} \tag{2.3b}$$

Here, ϕ_F is the electrostatic potential in the semiconductor bulk, ϵ_{semi} and ϵ_{ins} are the dielectric constants of the semiconductor and insulator, respectively, d_{ins} is the effective thickness of the insulator, N_A^{eff} is the effective acceptor density, ϕ_{MS} is the potential difference between the metal gate and semiconductor bulk at zero gate bias, and Q_{eff} is the effective interface charge. For simplicity, we account for the cumulative effect of all charges, other than that from N_A^{eff}, in the semiconductor by assuming an effective charge Q_{eff} at the semiconductor-to-gate insulator interface [8]. In actuality, the charges in the device that affect the threshold voltage of OFETs are the fixed bulk charge, the mobile charge, and the interface trapped charge. We can associate the negative threshold voltage of the p-channel OFETs with a density of positively charged states in the semiconductor channel N_T [9].

The subthreshold swing is extracted from the linear regime transfer characteristics, in the transition from the OFF-state to the ON-state, using the following equation:

$$I_D \propto 10^{-V_{GS}/S} \tag{2.4}$$

In this equation S is the subthreshold swing (V/decade), which can be associated with the density of deep bulk states (N_{BS}) in the organic semiconductor and interface states (N_{SS}) at the interface between the gate insulator and organic semiconductor through [10]:

$$S = \frac{kT}{q\log(e)}\left[1 + \frac{qd_{ins}}{\epsilon_{ins}}\left(\sqrt{\epsilon_{semi}N_{BS}} + qN_{SS}\right)\right] \tag{2.5}$$

where k, T, and q are the usual physical parameters, ϵ_{ins}, ϵ_{semi} and d_{ins} have been described above. Though an exact relation between the subthreshold swing of an OFET and the

density of states in the active organic semiconductor material has yet to be developed, we expect that equation (2.5) can provide an estimate since it has been successfully for devices based on amorphous semiconductors. In other words, we can assume that the subthreshold swing can be positively associated with the densities of bulk states and interface states (i.e., as the state densities increase, the device will turn on slower with applied gate bias, and therefore a larger subthreshold swing will be observed). This agrees with the relation shown in (2.5).

From the linear regime transfer characteristics of the device in the dark, shown in Figure 2.2(b), we find typical values of the linear regime field-effect mobility, threshold voltage, and subthreshold swing to be 4×10^{-3}cm^2/Vs, -25V, and 3.0V/decade, respectively.

The standard method used to extract the saturation regime field-effect mobility (μ_{FEsat}) and threshold voltage (V_{Tsat}) from the saturation regime transfer characteristics (drain current versus gate-to-source voltage, $I_D - V_{GS}$, with $V_{DS} \geq V_{GS}$ for the saturation regime) uses the following equation, based on the MOSFET theory [6]:

$$I_D = -\mu_{FEsat} C_{ins} \frac{W}{2L} (V_{GS} - V_{Tsat})^2 \tag{2.6}$$

From the saturation regime transfer characteristics, shown in Figure 2.2(c), we find typical values of the saturation regime field-effect mobility and threshold voltage to be 5×10^{-3}cm^2/Vs and -20V respectively. In general, we find values of the saturation regime field-effect mobility to be slightly larger than the field-effect mobility in the linear regime.

2.3 DC performance parameter extraction methods and models

The electrical performance of organic electronic devices, such as organic field-effect transistors (OFETs) has steadily improved over the past several years [1, 3, 11–13]. This improvement can be attributed to the development of high quality organic semiconduc-

tors and to the engineering of device structures and fabrication methods, as well as to the progress made in explaining the underlying physics of organic materials and devices. One important factor in the development of this class of devices is the ability to reliably compare the various performance parameters (i.e., field-effect mobility, threshold voltage and ON/OFF ratio) extracted for different devices and found by different research groups. In this section, the methods used to extract the field-effect mobility from the transfer characteristics of OFETs will be discussed.

In the past, several research groups have examined the field-effect mobility in OFETs from various theoretical perspectives. These studies were based on either the variable-range hopping (VRH) model [14–16] or on the multiple trapping and release (MTR) model [17,18]. For the case of VRH, the transport of charge carriers occurs within organic molecules by hopping (or tunneling) from one localized state to another, either over a short distance with a relatively high activation energy or over a longer distance with a smaller activation energy. In the MTR model, the charge carriers move within organic molecules from localized states to delocalized states by thermal activation. Charge transport occurs through the delocalized states until the carriers are trapped into another localized state, and so on. The derived analytical expressions were shown to agree well with the experimentally determined gate bias and temperature dependence of the field-effect mobility, but the validity of each model in various organic molecular systems (i.e., well organized small molecule systems versus amorphous polymer systems) is still under debate.

Other groups have studied the effect of various device fabrication methods on the field-effect mobility. It was observed that the field-effect mobility has a significant dependence on the morphology and ordering of the molecules in the thin-film (for both small molecule and polymers). The ordering of the molecules can be controlled by the deposition temperature and rate for vacuum-deposited small molecules [19–21], by the solvent used for

deposition from solution [22, 23] and by mechanical treatment of the substrate before the deposition of the organic semiconductor. Furthermore, it should be noted that the dependence of the charge carrier mobility on the applied gate bias seems to arise from the variation of the mobility with carrier density in the channel [17, 18, 24]. The density of charge carriers in the channel is controlled by the applied gate bias (i.e., accumulation of holes in p-channel devices), therefore, this translates into the observed dependence of the carrier mobility with the applied gate bias.

The dependence of the field-effect mobility on applied gate bias often results in a non-ideal behavior of the OFET transfer characteristics with gate-to-source bias, at low drain-to-source voltage [25, 26]. In this section, we present a tractable method of extracting the field-effect mobility from the transfer characteristics of OFETs, in both the linear and saturation regimes. This method is based on the commonly used MOSFET square-law drain current equations with a modification to allow the dependence on the applied gate bias to be taken into account. Using this method, we show that the field-effect mobility extracted using the standard equations can be significantly overestimated, giving results that may be unreliable [27]. This method is then used to extract the field-effect mobility and related parameters from the transfer characteristics at different temperatures, and the dependence of these parameters on temperature is presented.

2.3.1 Extraction methods and discussion

As stated above, the OFET transfer characteristics at low drain voltage do not always exhibit a perfectly linear behavior with applied gate bias, above the threshold voltage, as in the case of ideal c-Si MOSFETs. Typical transfer characteristics of an F8T2-based OFET are shown in Figure 2.3 and Figure 2.4. This deviation from the ideal c-Si MOSFET behavior, has also been observed in thin-film transistors based on amorphous semiconduc-

tors, such as a-Si:H TFTs [28–32] where it has been associated with dispersive transport of the charge carriers (electrons) in a-Si:H [31, 33]. In general, in amorphous and other low-mobility solids (including organic polymers), the movement of an injected pulse of charges in a steady electric field produces a completely smeared-out drift of the pulse. This is due, in part, to heavy trapping of the charge carriers and the slow release from the traps under thermal excitation. In such a case, it is difficult to define the transit time of any particular charge carrier. Instead, the time dependence of the current is described by a power-law:

$$I(t) \propto t^{-s}, \ (0 < s < 2) \tag{2.7}$$

where t is time and s is a material dependent parameter related to the dispersive nature of the transport mechanisms. This type of behavior is known as dispersive carrier transport in disordered materials.

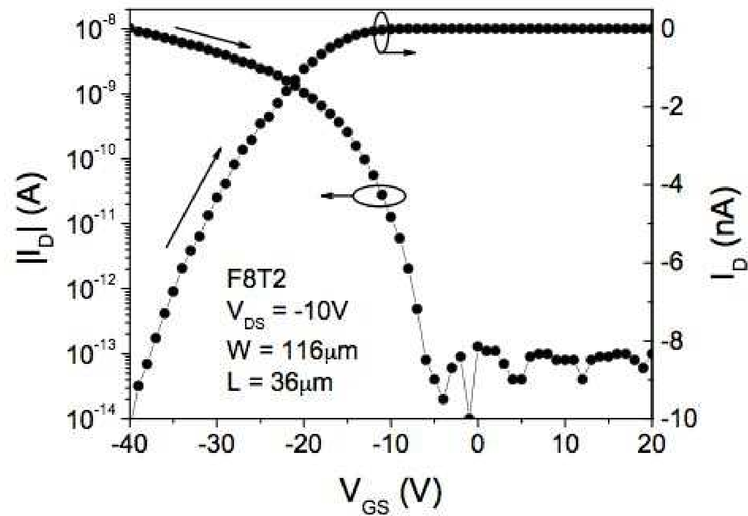

Figure 2.3: F8T2-based OFET linear regime transfer characteristics. Arrows indicate direction of measurement.

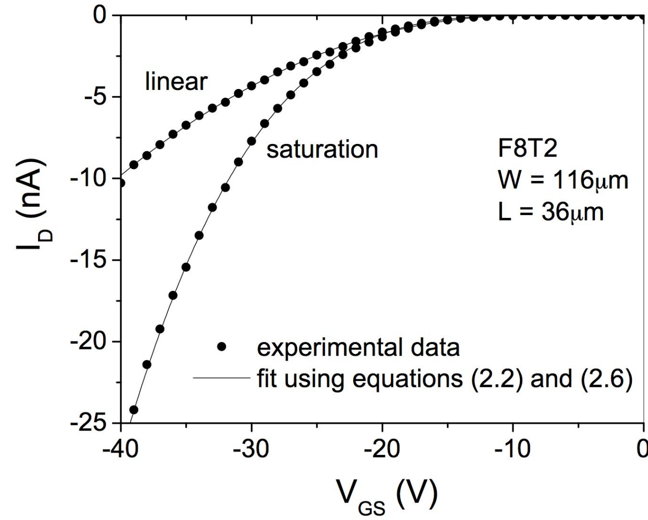

Figure 2.4: OFET transfer characteristics in the linear and saturation regimes. Symbols represent experimental data, solid lines show fits to equation (2.10) and equation (2.20), respectively.

Linear regime

To accommodate dispersive carrier transport, a general expression for the drain current has been derived by Merckel, et al from Kishida and Leroux [28–30]:

$$I_D = -\mu_{FE} C_{ins} \frac{W}{L} \frac{1}{\gamma + 1} \left[(V_{GS} - V_{Tlin})^{\gamma+1} - (V_{GS} - V_{Tlin} - V_{DS})^{\gamma+1} \right] \tag{2.8}$$

The right side of equation (2.8) can be series expanded in V_{DS} to the second order to give the linear regime drain current as:

$$I_D = -\mu_{FE} C_{ins} \frac{W}{L} (V_{GS} - V_{Tlin})^{\gamma-1} \left[(V_{GS} - V_{Tlin}) V_{DS} - \frac{\gamma}{2} V_{DS}^2 \right] \tag{2.9}$$

For low V_{DS}, the $\frac{\gamma}{2} V_{DS}^2$ term becomes negligible and equation (2.9) reduces to:

$$I_D^{lin} = -\mu_{FElin0} C_{ins} \frac{W}{L} (V_{GS} - V_{Tlin})^{\gamma} V_{DS} \tag{2.10}$$

where μ_{FElin0} is a fitting parameter associated with the field-effect mobility of the device in the linear regime and the other parameters have been described above. We should note

that the unit of μ_{FElin0} is not cm^2/Vs but $cm^2/V^{\gamma}s$.

The modified equation includes an additional parameter, γ, which can be associated with the non-linearity of the device transfer characteristic at low V_{DS} [28–31]. The physical significance of γ in amorphous semiconductors has often been expressed by:

$$\gamma = 2\frac{T_0}{T} - 1 \tag{2.11}$$

where T_0 is the characteristic temperature of the semiconductor density-of-states distribution around the position of the Fermi level [26, 30]. The equation is valid for $T < T_0$. As an example of the application of this theory to an amorphous semiconductor, consider the case of a-Si:H TFTs, which are usually operated as n-channel devices. For this case, T_0 is the characteristic temperature (i.e., slope) of the conduction band tail. In a-Si:H, the non-ideal situation of $\gamma > 1$ is associated with a high density of conduction band tail states, which can be attributed to variations of the Si-Si bond angles and distances in the amorphous semiconductor. We have also previously demonstrated for a-Si:H TFTs [34] that γ can be significantly under-estimated in cases of non-negligible source and drain series resistances. Indeed, $\gamma = 1$ can be observed for a TFT with both a high density of conduction band tail states and high source and drain series resistances.

To fit the OFET experimental data in the linear regime over a wide gate voltage range, shown in Figure 2.4, we used equation (2.10) and the fitting parameters summarized in Table 2.2. The physical significance of γ values larger than one in organic devices has not yet been fully explained. However, we believe that, following the amorphous semiconductor ideas described above, it can be associated with an energy dependent high density of states distribution around the Fermi level position, caused by residual disorder in the locally self-organized polymer film. In other words, the amorphous nature of the organic semiconductor leads to a density of states with band-tail states at the valence and conduction band edges. For the case we are dealing with here, i.e., for p-type semiconductor action, γ is

Table 2.2: Fitting Parameters Used For Figure 2-3(b).

	Linear regime	Saturation Regime
W/L	116/36	116/36
C_{ins} (F/cm^2)	7.5×10^{-9}	7.5×10^{-9}
μ_{FElin0} or μ_{FEsat0} $\times C_{ins}\times(W/L)$ $(A/V^{\gamma+1})$	7×10^{-12}	1×10^{-13}
μ_{FE} (cm^2/Vs) at $V_{GS}-V_T=-25V$	1×10^{-3}	2×10^{-3}
γ	2.1	2.5
T_0 (K)	465	525
V_{Tlin} and V_{Tsat} (V)	-9	-6

related to the slope of the valence band-tail states through the characteristic temperature T_o of the valence band-tail states and is still given by the relation of equation (2.11). As the carrier concentration increases, localized states are filled and the Fermi level approaches a region of the density of states of more extended electronic states (i.e., the band edge) with higher mobilities. Indeed, the gate voltage dependence of the OFET field-effect mobility has already been connected to the characteristic temperature of the semiconductor density-of-states distribution around the position of the Fermi level, T_0 [15]. As stated above, when the OFET parameter extraction is performed using equation (2.10), the unit of μ_{FElin0} is not cm^2/Vs but $cm^2/V^{\gamma}s$, and equation (2.10) is therefore used only to extract γ.

To comment further, we should note that, unlike the case of amorphous organic materials we are dealing with here, the case of a more crystalline (ordered) small molecule organic semiconductor allows a possible connection between the molecular structure and the density of states (i.e., γ) of a thin film, through computer simulations. The case of amorphous materials introduces disordered molecular potentials, due to morphological and conformational variations in the molecules that make up the film, which are more difficult to simulate with a reasonable amount of resources (including time). Alternatively,

it is also possible to rewrite equation (2.10) as:

$$I_D^{lin} = -\mu_{FElin0}\,(V_{GS} - V_{Tlin})^{\gamma-1}\,C_{ins}\frac{W}{L}\,(V_{GS} - V_{Tlin})\,V_{DS} \tag{2.12}$$

which becomes:

$$I_D^{lin} = -\mu_{FElin}\,(V_{GS})\,C_{ins}\frac{W}{L}\,(V_{GS} - V_{Tlin})\,V_{DS} \tag{2.13}$$

with:

$$\mu_{FElin}\,(V_{GS}) = \mu_{FElin0}\,(V_{GS} - V_{Tlin})^{\gamma-1} \tag{2.14}$$

Equation (2.13) is very similar to the standard MOSFET equation (2.2) in the linear regime, but contains the gate voltage dependence of the field-effect mobility. It is therefore inaccurate to extract μ_{FElin} from equation (2.2), as it is done for the MOSFET, because of the gate voltage dependence of the field-effect mobility. As it has been pointed out previously [27], doing so would overestimate the field-effect mobility of the device by a factor γ, as indicated by the equations below. Using equation (2.2), the field-effect mobility is sometimes extracted using the following equation:

$$\mu_{calc}^{lin} = \frac{1}{V_{DS}C_{ins}W/L}\left(\frac{dI_D^{lin}}{dV_{GS}}\right) \tag{2.15}$$

with:

$$\frac{dI_D^{lin}}{dV_{GS}} = \mu_{FElin}C_{ins}\frac{W}{L}V_{DS} \tag{2.16}$$

However, if the field-effect mobility is gate voltage dependent, equation (2.2) has to be replaced by equation (2.10) or equation (2.13). In such a case, the field-effect mobility expression becomes:

$$\mu_{calc}^{lin} = \gamma\mu_{FElin0}\,(V_{GS} - V_{Tlin})^{\gamma-1} \tag{2.17}$$

or:

$$\mu_{calc}^{lin} = \gamma\mu_{FElin}\,(V_{GS}) \tag{2.18}$$

where:

$$\mu_{FElin} = \mu_{FElin0} (V_{GS} - V_{Tlin})^{\gamma-1} \tag{2.19}$$

This equation clearly indicates that the OFET field-effect mobility can be overestimated by a factor γ if the parameter extraction is not done properly. These observations are illustrated in Figure 2.5 where we have plotted the field-effect mobility in the linear regime extracted by the different methods mentioned here.

1. Conventional value extracted from experimental data using, equation (2.2), the standard MOSFET drain current equation in the linear regime;
2. Values calculated using equation (2.14) and the fitting parameters from Table 2.2;
3. Values extracted from experimental data using equation (2.15), i.e., μ_{calc}^{lin};
4. Values extracted from experimental data using equation (2.15) and taking into account γ, i.e., μ_{calc}^{lin}/γ.

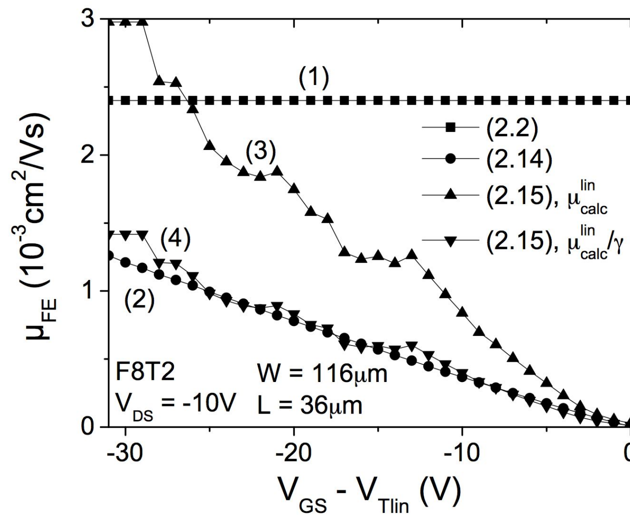

Figure 2.5: Comparison of the results of several extraction methods used to find the OFET field-effect mobility of the same device as used in Figure 2.3, in the linear regime.

Note that curves (1) and (3) show significantly overestimated values of the field-effect mobility, especially at moderate gate voltages. For the case of (1), the extraction using the

standard MOSFET equations, which ignores the gate bias dependence of the mobility, the extracted mobility is constant with applied gate bias, as shown in Figure 2.5. On the other hand, curves (2) and (4) are very similar and increase with gate bias, as expected from the discussion above. Therefore, it is critical to keep in mind that when the conventional field-effect mobility extraction method (i.e., using equation (2.2)) is applied to OFETs, the values found for the linear regime field-effect mobility can be significantly overestimated. We can also conclude that the methods used to extract curves (2) and (4) are the most appropriate for OFETs, and allow a more reliable comparison of the electrical performance of different devices and materials.

Saturation regime

In the saturation regime, (i.e., $V_{DS} \geq V_{GS} - V_{Tsat}$), equation (2.8) becomes equation (2.20).:

$$I_D^{sat} = -\mu_{FEsat0} C_{ins} \frac{W}{(\gamma + 1) L} (V_{GS} - V_{Tsat})^{\gamma+1} \tag{2.20}$$

where μ_{FEsat0} is the saturation regime field-effect mobility fitting parameter, V_{Tsat} is the threshold voltage in the saturation regime and the other parameters have been described above.

Figure 2.4 also shows the OFET drain current in the saturation regime and the fit to equation (2.20) using the parameters summarized in Table 2.2.

Following the same method as that used for the linear regime, it is possible to rewrite equation (2.20) as:

$$I_D^{sat} = -\mu_{FEsat0} (V_{GS} - V_{Tsat})^{\gamma-1} C_{ins} \frac{W}{(\gamma + 1) L} (V_{GS} - V_{Tsat})^2 \tag{2.21}$$

or

$$I_D^{sat} = -\mu_{FEsat} (V_{GS}) C_{ins} \frac{W}{(\gamma + 1) L} (V_{GS} - V_{Tsat})^2 \tag{2.22}$$

with

$$\mu_{FEsat}(V_{GS}) = \mu_{FEsat0}(V_{GS} - V_{Tsat})^{\gamma-1} \tag{2.23}$$

Equation (2.22) is very similar to the standard MOSFET equation in the saturation regime, but contains the gate voltage dependence of the field-effect mobility. As was the case with the linear regime parameter extraction, it is inaccurate to extract μ_{FEsat} as it is done for the MOSFET because of the gate voltage dependence of the field-effect mobility. As it has been pointed out previously [27], doing so would overestimate the field-effect mobility of the device by a factor $(\gamma + 1)/2$, as indicated by the equations below. It is possible to write the standard saturation regime MOSFET equation (2.6) as follows:

$$\sqrt{\left|I_D^{sat}\right|} = \sqrt{\mu_{FEsat} C_{ins} \frac{W}{2L}}\,(V_{GS} - V_{Tsat}) \tag{2.24}$$

Consequently, the field-effect mobility is sometimes extracted using the following equation:

$$\mu_{calc}^{sat} = \frac{1}{C_{ins} W/2L}\left(\frac{d\sqrt{\left|I_D^{sat}\right|}}{dV_{GS}}\right)^2 \tag{2.25}$$

with:

$$\frac{d\sqrt{\left|I_D^{sat}\right|}}{dV_{GS}} = \sqrt{\mu_{FEsat} C_{ins} \frac{W}{2L}} \tag{2.26}$$

However, if the field-effect mobility is gate voltage dependent, equation (2.6) has to be replaced by equation (2.20) or equation (2.22). In such a case, the field-effect mobility expression becomes:

$$\mu_{calc}^{sat} = \left(\frac{\gamma + 1}{2}\right)\mu_{FEsat0}(V_{GS} - V_{Tsat})^{\gamma-1} \tag{2.27}$$

or:

$$\mu_{calc}^{sat} = \left(\frac{\gamma + 1}{2}\right)\mu_{FEsat}(V_{GS}) \tag{2.28}$$

where:

$$\mu_{FEsat} = \mu_{FEsat0}(V_{GS} - V_{Tsat})^{\gamma-1} \tag{2.29}$$

In Figure 2.6, we show the values of the extracted field-effect mobility in the saturation regime, using the following methods.

1. Conventional value extracted from experimental data using the standard saturation regime MOSFET equation (2.6);
2. Values calculated using equation (2.23) and fitting parameters from Table 2.2;
3. Values extracted from experimental data using equation (2.25), i.e., μ_{calc}^{sat};
4. Values extracted from experimental data using equation (2.25) and taking into account γ, i.e., $\mu_{calc}^{lin}/(\gamma + 1/2)$.

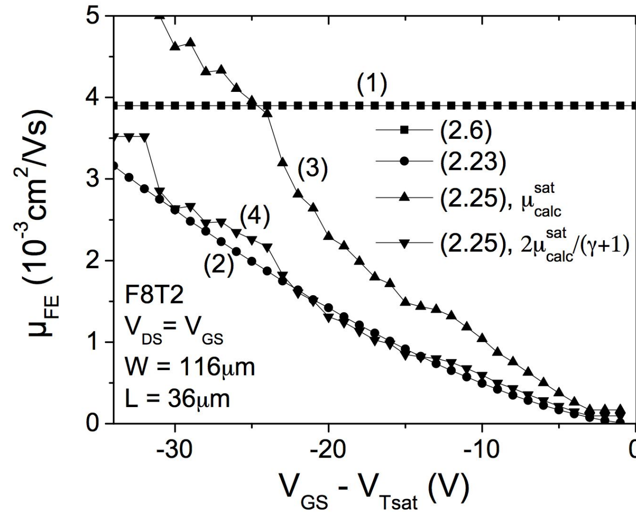

Figure 2.6: Comparison of the results of several extraction methods used to find the OFET field-effect mobility of the same device as used in Figure 2.3, in the saturation regime.

Note that, as shown in Figure 2.6 and as it is with the case for the extraction in the linear regime, the curves (1) and (3) show significantly overestimated values of the field-effect mobility in the saturation regime, especially at moderate gate voltages. For the case of curve (1), we see that the extraction results in a mobility that is independent of the applied gate bias. The difference in the results from each method is less significant for large values of the gate voltage. On the other hand, curves (2) and (4) are very similar, and give the

expected result of increasing field-effect mobility with applied gate bias. Therefore, it is critical to keep in mind that when the conventional extraction method (i.e., using equation (2.6)) is applied to OFETs, the field-effect mobility in the saturation regime can be significantly overestimated. We can also conclude that the methods used to extract curves (2) and (4) are the most appropriate for OFETs.

In general, the behavior of the mobility for the case of devices based on disordered materials (i.e., OFETs based on F8T2) is different from the case of devices based on crystalline materials (i.e., MOSFETs based on c-Si) because of the nature of the density of states, near the position of the Fermi level, that the carriers move through. Crystalline materials are characterized by well-defined, delocalized transport bands separated by an energy gap that is nearly devoid of localized states, resulting in a mobility that has negligible dependence on the applied gate bias. Whereas, in disordered materials, the delocalized transport bands are not well defined and there exists a significant density of localized states in the energy gap, as well as band edges that are not ideal in nature and consist of sloped band-tails.. This shape of density of states results in a field-effect mobility that has a significant dependence on the applied gate bias, since the region of the density of states, through which the charge carriers are transported, changes with the applied gate bias.

2.3.2 Dependence on temperature

We have used the extraction methods developed in the previous section on OFET transfer characteristic data taken at different temperatures ranging from 10°C to 80°C, as shown in Figure 2.7.

In Figure 2.7, we see that the OFF-state drain current is significantly affected by the temperature of the device, and increases from approximately 5×10^{-13}A to 5×10^{-12}A as the temperature is increased from 10°C to 80°C. Also, note that the subthreshold slope of the

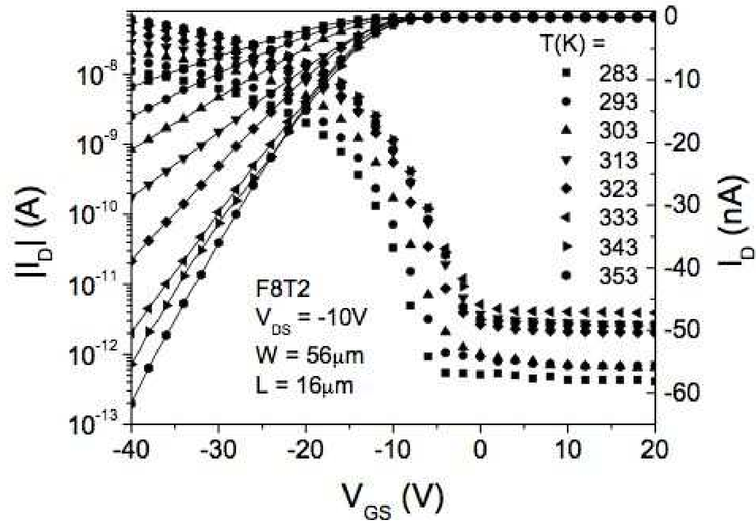

Figure 2.7: Linear regime transfer characteristics of an OFET measured at different temperatures between 10°C and 80°C. The symbols correspond to experimental data and the lines correspond to fits using equation (2.10)

transfer characteristics (i.e., the slope of the semilog plots in the transition regime from the OFF-state to the ON-state) does not appear to be affected by the temperature, indicating that the region of the density of states of the organic semiconductor near the Fermi level is not significantly altered. In Figure 2.7, the symbols represent the experimental data and the lines show fits of the linear plots using equation (2.10). From the fits, the linear regime field-effect mobility μ_{FElin0}, linear regime threshold voltage V_{Tlin}, and the γ-parameter are extracterd from the data of Figure 2.7 at different temperatures. Then, using equation (2.14), μ_{FElin} as a function of applied gate bias is calculated for each temperature. The field-effect mobility increases with gate bias, as shown in Figure 2.8, and the temperature dependence of the field-effect mobility at different applied gate biases is shown in Figure 2.9.

The fit of μ_{FElin} with temperature is an Arrhenius relationship of the form:

$$\mu_{FElin} = \mu^{*}_{FE} e^{-E_a/kT} \tag{2.30}$$

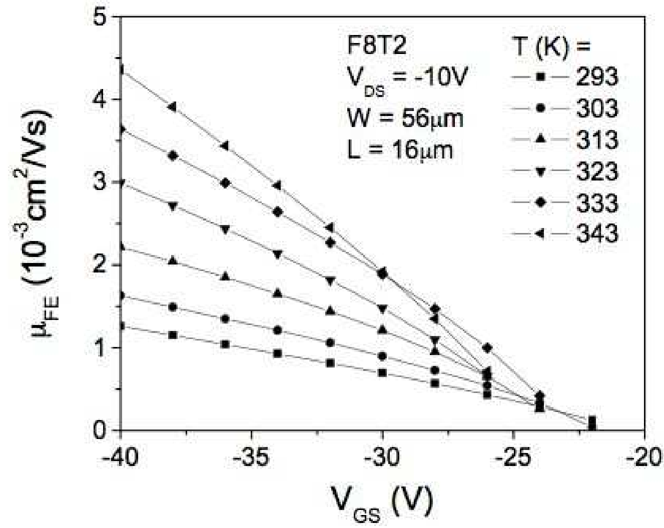

Figure 2.8: Dependence of the field-effect mobility on applied gate bias at different temperatures, found from the data shown in Figure 2.7 using equation (2.10) and equation (2.14).

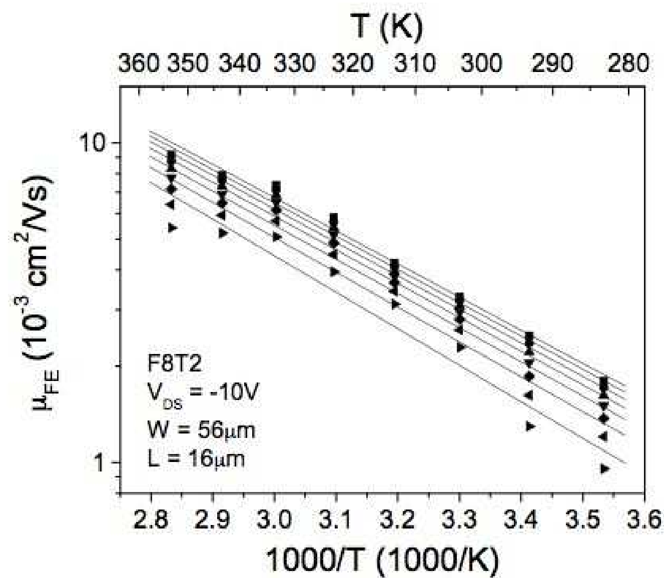

Figure 2.9: Dependence of the OFET field-effect mobility on temperature, taken from the data shown in Figure 2.7 at different gate biases. $|V_{GS}|$ increases from 28V to 40V for the data from the bottom to the top of the figure. Symbols are experimental data and straight lines are the fits to an Arrhenius relationship, giving the activation energy (E_a) of the field-effect mobility.

where μ_{FE}^{*} is the pre-exponent factor of the mobility and has a value of approximately 10 cm^2/Vs here. The fit is excellent up to approximately 80°C and we can see that, as expected, the field-effect mobility is activated in temperature. In Figure 2.10, we present the thermal activation energy E_a of the field-effect mobility as a function of applied gate bias. This data was taken from the mobility data found using methods (2) and (4), described in the previous section.

From this figure, we see that E_a is constant at a value of approximately 0.2eV for high

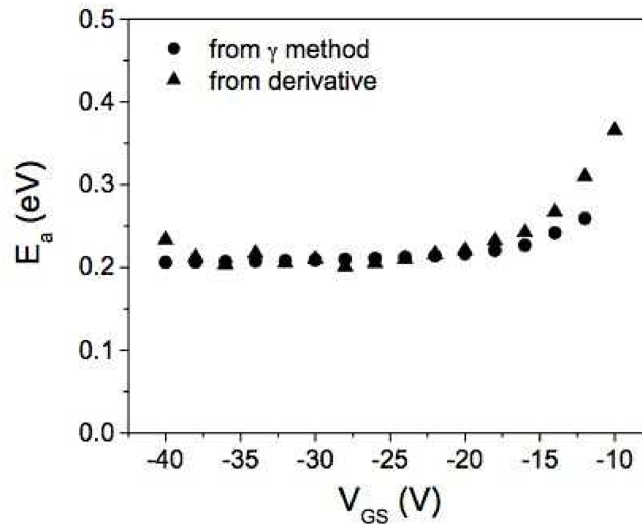

Figure 2.10: The activation energy of the OFET field-effect mobility as a function of applied gate bias, found from the data shown in Figure 2.9.

applied gate biases ($|V_{GS}| \gtrsim |V_{Tlin}|$) and increases for lower gate biases. Similar results were obtained by others and were associated with the filling of low-lying localized electronic states by the accumulated charges as the gate bias is increased [15]. We should note that this entire method is only valid for gate biases above the threshold voltage, or in other words, for gate biases that bias the device into accumulation.

Furthermore, the dependence of the threshold voltage, extracted from Figure 2.7 using equation (2.10), on temperature is shown in Figure 2.11, and we can see that the threshold

voltage decreases slightly with increasing temperature, at a rate of approximately 0.04V/K over the range of temperature we used here.

We present the temperature dependence of γ, found from Figure 2.7 using equation

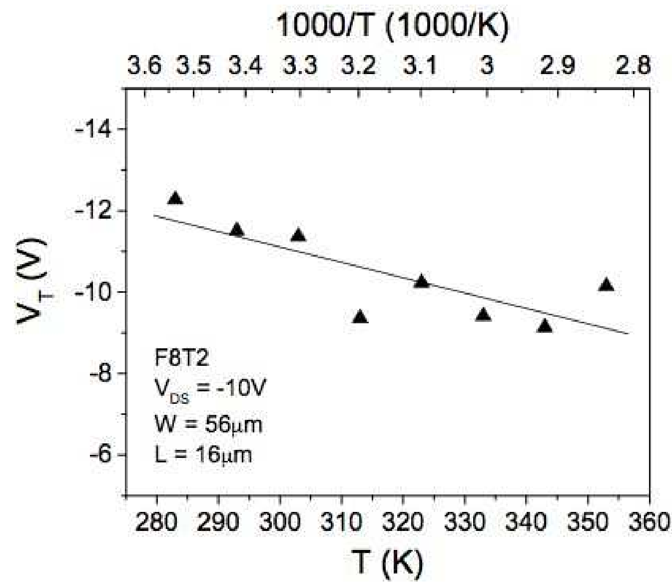

Figure 2.11: Dependence of the OFET threshold voltage on temperature, extracted from the data shown in Figure 2.7. Symbols are experimental data and the straight line is the linear fit, which serves as a guide to the eye.

(2.10), in Figure 2.12. We can see from this figure that γ has a value significantly larger than unity and has a more complex dependence on temperature. The observed temperature dependence is not the expected result that should follow from equation (2.11). At the lower temperatures, below 40°C, γ decreases with temperature, as expected. However, at higher temperatures, above 40°C, the dependence on temperature is reversed and reduced. Though these results were reproduced several times, further investigation of the dependence of γ on temperature is needed.

2.4 Source/drain contact resistance and intrinsic device performance

The electrical performance of thin-film transistors are often limited by the resistance between the active layer material and the source and drain electrodes (i.e., contact resis-

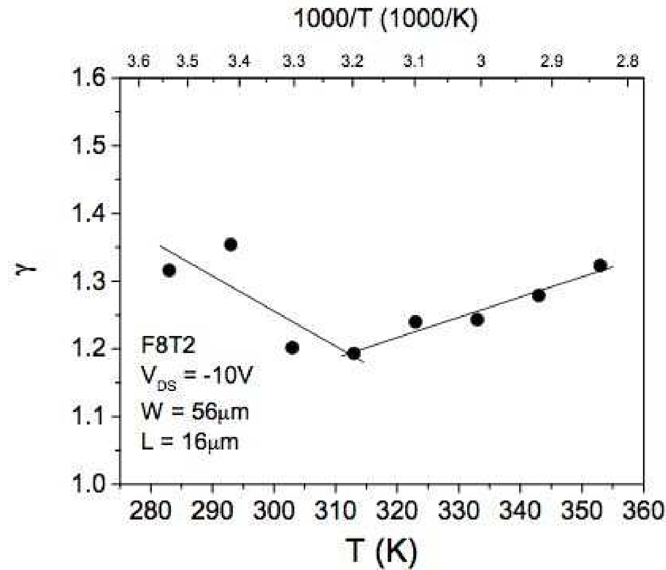

Figure 2.12: Dependence of the OFET gamma parameter on temperature, extracted from the data shown in Figure 2.7. Symbols are experimental data and the straight lines are linear fits to the corresponding sections of the gamma data and serve as guides to the eye.

tance) [35–42]. This resistance presents itself as an additional resistance to the current that flows through the channel of the device and thereby reduces the performance of the device. In this section, the source and drain contact resistance and intrinsic device performance (i.e., intrinsic field-effect mobility and intrinsic threshold voltage) are characterized. Additionally, the temperature dependence of the intrinsic performance and contact resistance is described.

In general, we have found that the source and drain electrodes made of indium tin oxide (ITO) provide effective electrical contact to the organic material. As shown in Figure 2.13, we see that the contacts exhibit a Schottky-type behavior (i.e., exponential dependence) at low V_{DS} and changes to an apparent space charge limited current type of behavior (i.e., quadratic dependence) at higher V_{DS} [35]. Note that the curves in this figure are similar for measurements with the gate electrode floating and with the gate electrode grounded to the common bias point.

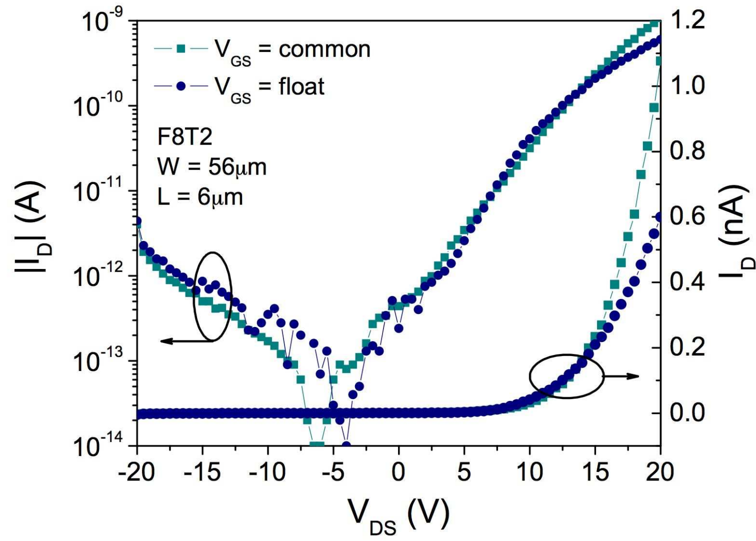

Figure 2.13: Drain current versus drain-to-source voltage for device measured with the gate electrode as common and floating.

2.4.1 Experimental results and analysis

To investigate the energetic properties of the source/drain electrical contacts and of the intrinsic electrical performance parameters (i.e., intrinsic field-effect mobility and threshold voltage), we measured the linear regime transfer characteristics at different temperatures ($10 < T < 70°C$) of a series of devices with different values of channel width (W) and channel length (L).

To continue with the analysis of these devices at different temperatures, we calculated the normalized ON resistance as:

$$W \times R_{ON} = W \times V_{DS}/I_D \tag{2.31}$$

and plotted it as a function of channel length as in Figure 2.14 below.

Performing linear fits to the data in Figure 2.14, provides the slopes of the normalized on resistance curves at several applied gate bias points. The inverse of the slopes are plotted as a function of applied gate bias as shown in Figure 2.15 for each set of measurements at

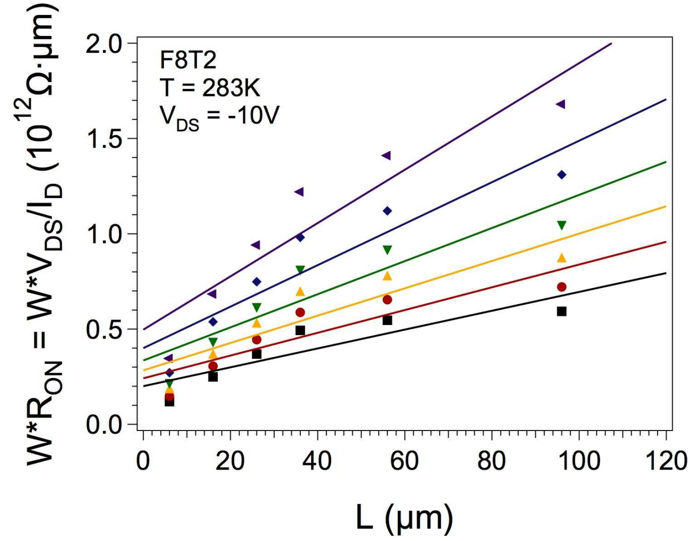

Figure 2.14: Normalized ON resistance (i.e., $W \times R_{ON} = W \times V_{DS}/I_D$) as a function of channel length for different applied gate biases above the threshold voltage. Similar results were obtained for calculations for measurements at the other temperatures.

different temperatures.

The linear fits to the data of Figure 2.15 provide a means of obtaining the intrinsic mobility and intrinsic threshold voltage at different temperature. These data are shown below in Figure 2.16 and 2.17, respectively.

Plotting the field-effect mobility as shown in Figure 2.16 allows for the determination of the activation energy of the field-effect mobility (over this limited temperature range). For the field-effect mobility, we find a μ_o of approximately 4 cm^2/Vs with an activation energy E_a of 0.19eV. These results agree very well with our previous measurements described above and parameter extractions without using the TLM (i.e., we found μ_o = 10 cm^2/Vs and E_a = 0.2eV in section 2.3).

We see from Figure 2.17 that the threshold voltage shows little dependence on the temperature, exhibiting $\Delta V_T/\Delta T$ = 92mV/K. These data are consistent with our previous extraction results (i.e., $\Delta V_T/\Delta T$ 40mV/K) presented in section 2.3.

From the y-intercepts of the data shown in Figure 2.14 (and from similar plots for mea-

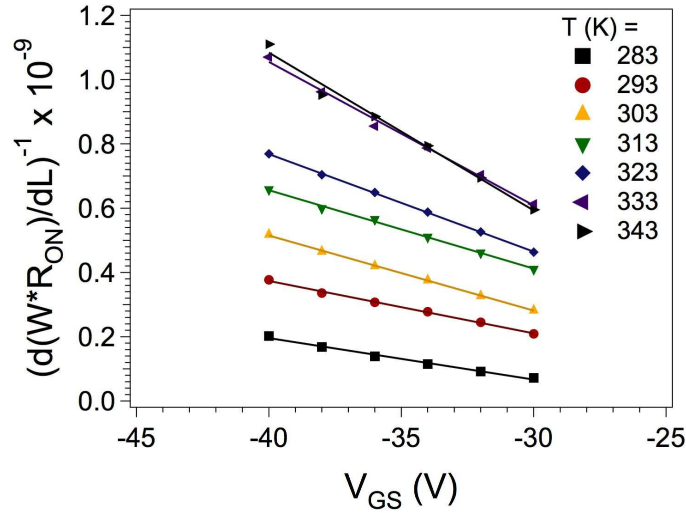

Figure 2.15: Inverse slopes of the linear fits to the data in Figure 2.14 as a function of applied gate bias above threshold voltage, (i.e., $d(W \times R_{ON})/dL)^{-1}$ vs. V_{GS}).

surements at other temperatures), we can extract the source/drain contact resistance. For comparison, we then calculate and plot the normalized contact resistance as a function of applied gate bias and temperature as shown below in Figure 2.18.

For devices biased above threshold, the S/D contact resistance drops exponentially with the applied gate bias. We see from Figure 2.19 and 2.20 that the contact resistance is activated with temperature with an activation energy near 0.2eV. The activation energy increases as the applied gate bias is decreased. These results seem to make physical sense, since we expect the contact resistance, as well as the energy required to inject/extract charge carriers, to decrease as the level of accumulation of charge carriers in the channel increases.

Given the contact resistance (extracted as described above), we can calculate and plot the channel resistance as a function of applied gate bias and temperature as shown in Figures 2.21 and 2.22. For a valid performance comparison, we use the average normalized channel resistance, averaged over the range of device geometries used in this study and normalized per unit channel length.

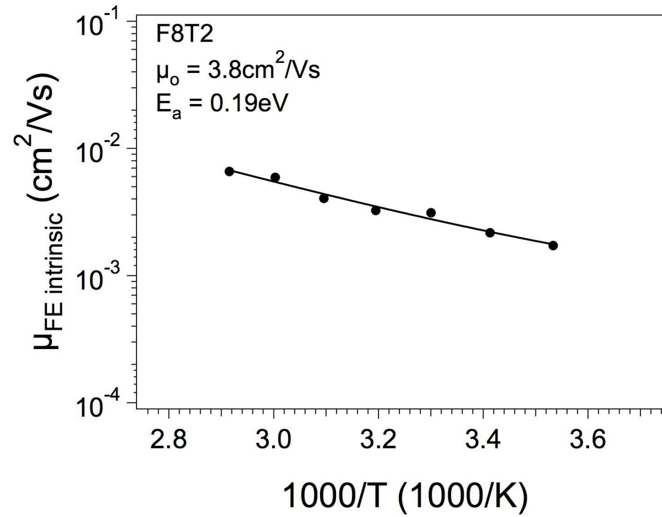

Figure 2.16: Intrinsic field-effect mobility (taken from the slopes of the data in Figure 2.15) plotted as a function of inverse temperature.

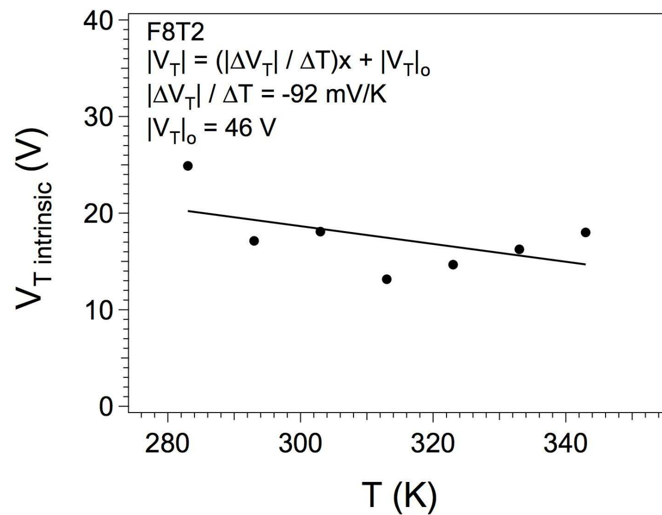

Figure 2.17: Intrinsic threshold voltage (taken from the x-intercepts of the linear fits shown in Figure 2.15) as a function of temperature.

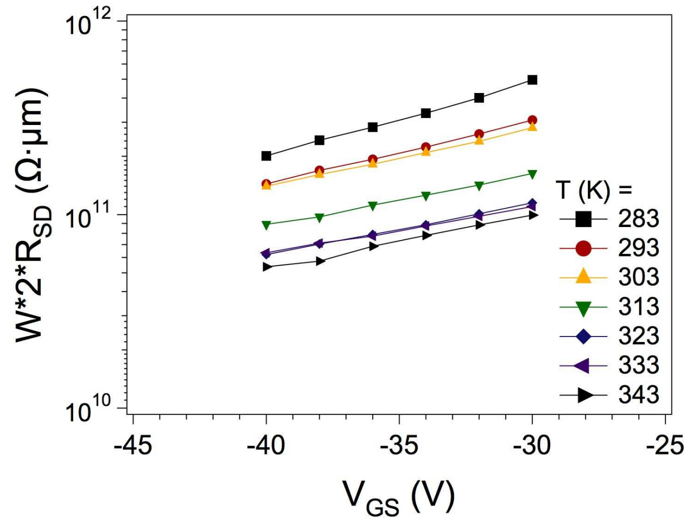

Figure 2.18: Normalized S/D contact resistance (i.e., channel width times total extracted S/D series resistance) as a function of applied gate bias for 283 < T < 343K.

Similar to the case for S/D contact resistance, we see that the channel resistance drops exponentially as the gate bias is increased and is thermally activated with an activation energy of approximately 0.2eV, which varies with applied gate bias as shown in Figure 2.23.

2.5 High-field operation

In order for OFETs to make their way into commercial applications, they must be able to operate within specific environmental conditions as well as provide the desired electrical performance. For example, in the case of flat-panel displays such as cholesteric liquid crystal displays, the driving circuitry must be able to output a large voltage in order to control the display. In this section, we present the electrical performance of these devices under high gate-to-source and drain-to-source electric fields.

To demonstrate the possible use of OFETs in high-voltage/high-power applications (such as electronic paper and certain types of liquid crystal displays) we tested the operation of these devices at high bias points (i.e., $V_{GSmax} = V_{DSmax} = -100V$, corresponding

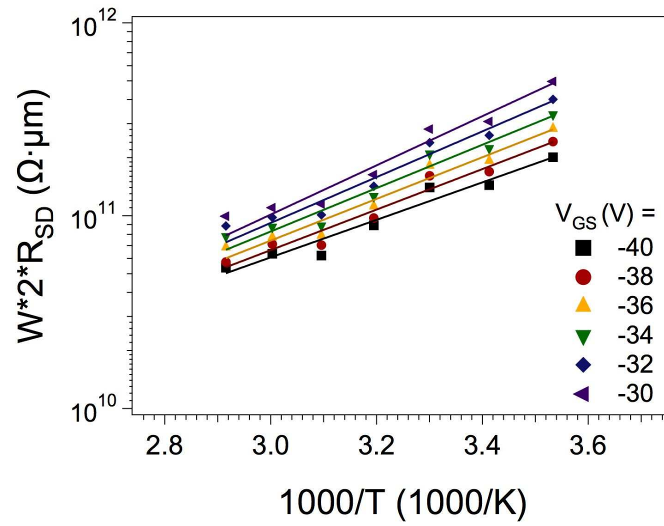

Figure 2.19: Normalized contact resistance as a function of temperature for various applied gate biases above threshold.

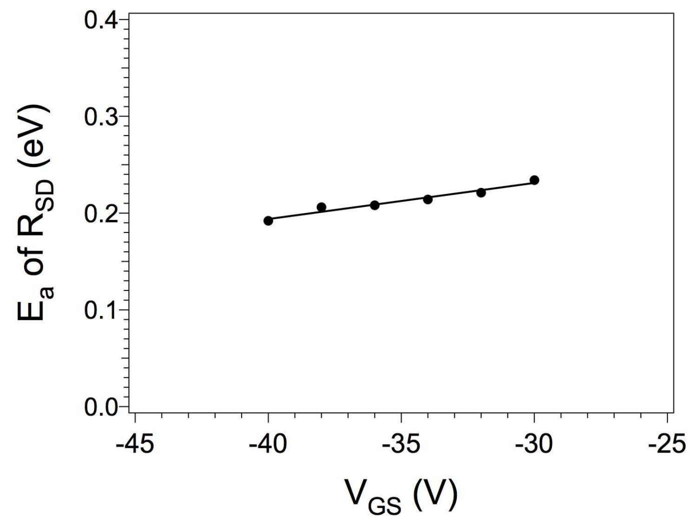

Figure 2.20: Activation energy of the normalized contact resistance as a function of applied gate bias.

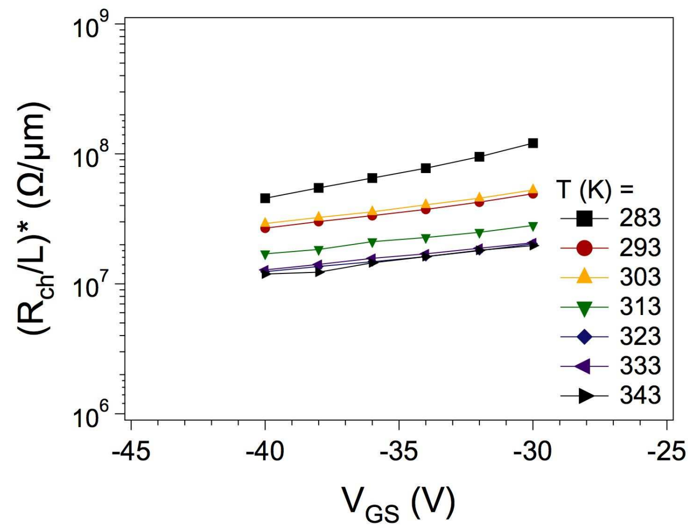

Figure 2.21: Average normalized channel resistance (i.e., channel resistance per unit channel length averaged over the range of different device geometries used in this study) as a function of applied gate biases above threshold for a range of temperatures.

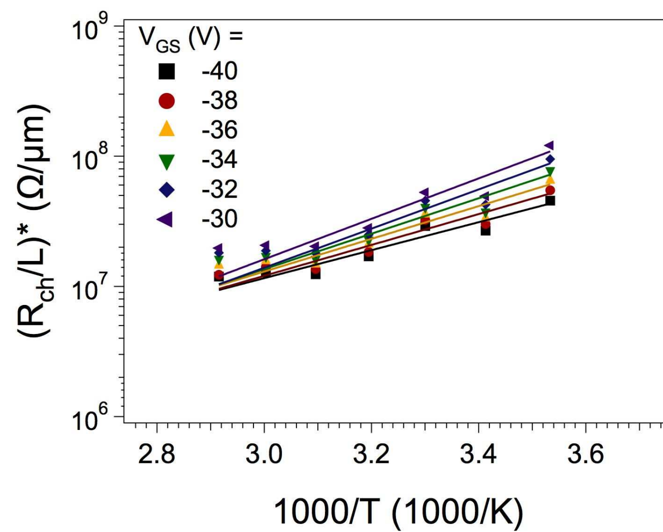

Figure 2.22: Average normalized channel resistance as a function of temperature for a range of applied gate biases.

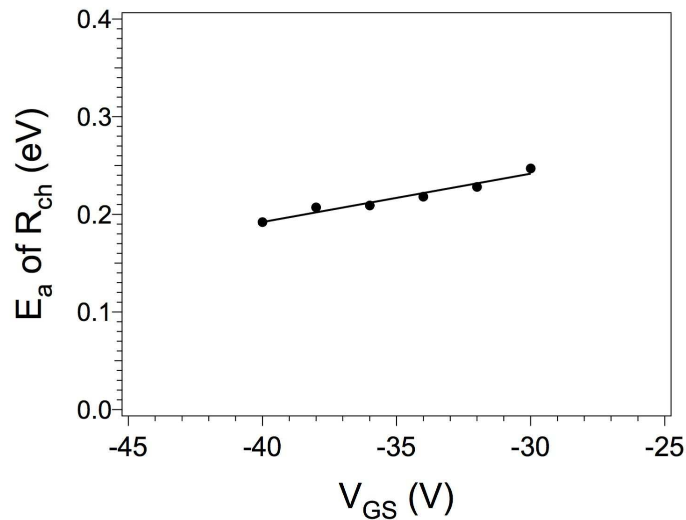

Figure 2.23: Activation energy of the average normalized channel resistance as a function of applied gate bias.

to a maximum electric field from drain-to-source of 1.67×10^5 V/cm). The results are presented and described below.

2.5.1 Experimental results and analysis

By examining the transfer characteristics presented in Figure 2.24, we see that under high-field conditions, the device performs as usual (i.e., similar to the low-bias case shown in Figure 2.2). As shown in this figure, we do observe a shift of the characteristics, corresponding to a threshold voltage shift, for measurements in different directions. This short-term, reversible effect is presumably due to the trapping of charge carriers in the channel of the device, near the gate-insulator organic semiconductor interface, These device instabilities are described in further detail in the following chapters.

Figure 2.25 demonstrates, that even for high gate-to-source electric fields, the gate insulator stack of this device structure is robust and maintains a low gate leakage current. Note that this measurement was taken at the same time as the data shown in Figure 2.24. For the device in the ON-state, the gate leakage current is at least 2 orders of magnitude

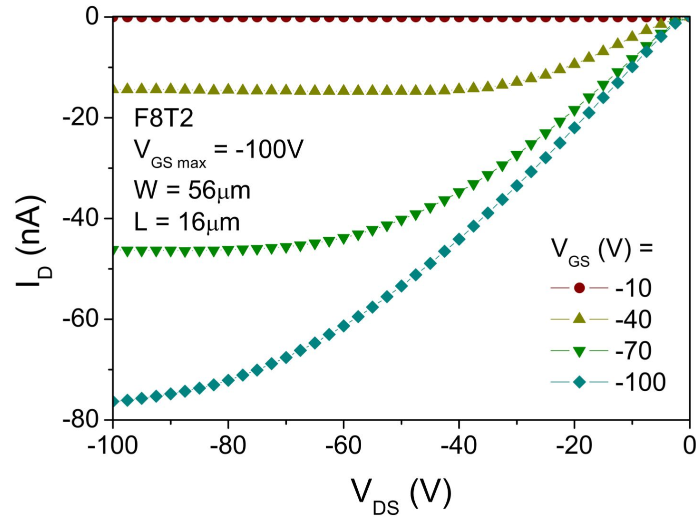

(a)

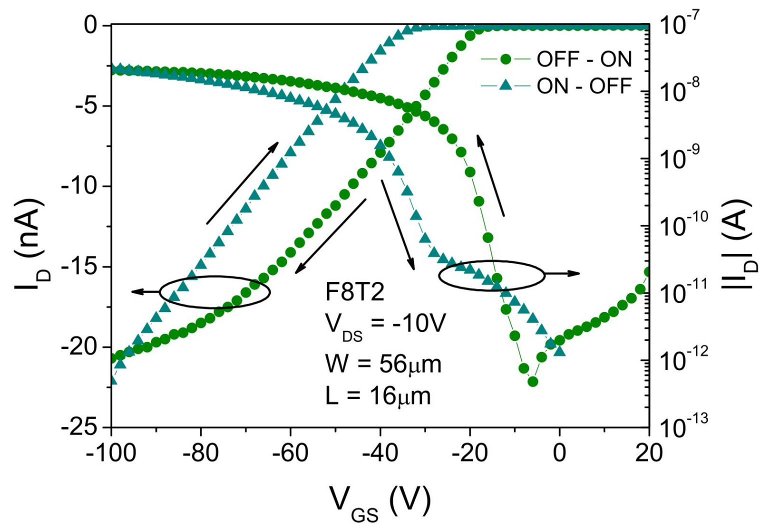

(b)

Figure 2.24: (a) Output characteristics of a device measured to $V_{DS\,max} = V_{GS\,max} = -100V$. (b) Linear regime transfer characteristics of a device measured (using a maximum gate bias of $V_{GS\,max}$ = -100V, corresponding to a maximum estimated electric field across the gate insulator of 1.67×10^5 V/cm) measured from OFF to strong accumulation (circles) and strong accumulation to OFF (triangles).

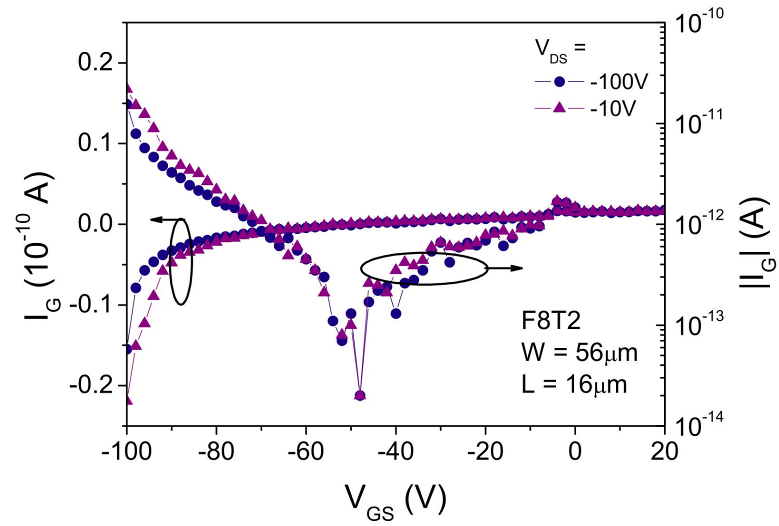

Figure 2.25: Gate leakage current as a function of applied gate-to-source bias, shown for two different applied drain-to-source biases.

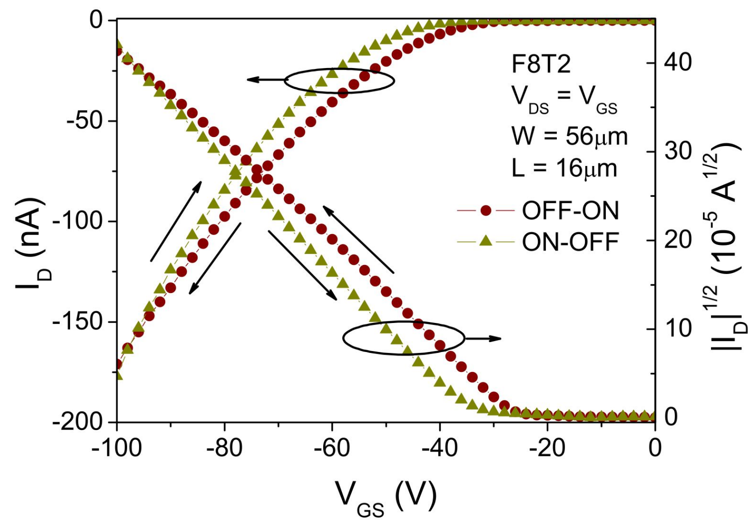

Figure 2.26: Saturation regime transfer characteristics (i.e., $V_{DS} = V_{GS}$).

below the drain current. For the device in the OFF-state, the drain current is reduced to nearly the same level as the gate leakage current.

From these characteristics, we see that the field-effect mobility does not deteriorate and the ON/OFF ratio stays the same for devices under high applied drain-to-source and gate-to-source biases. However, there are significant threshold voltage shifts and the sub-threshold slope appears to degrade as the maximum gate-to-source bias is increased.

From these results, we see that the F8T2-based OFETs appear to be good candidates for applications requiring high-voltage devices, including high-voltage, low current switches, as well as inverters. Though there are significant shifts in the electrical characteristics, there does not appear to be any breakdown occurring through the channel or through the gate-insulator. We expect that devices based on similar materials and structures could function properly and provide the necessary requirements to drive certain flat-panel display technologies requiring high voltage requirements.

2.6 Conclusion

The structure of the device used in the present experiments and the operation and measurement of this device has been reviewed. Additionally, a method that can be used to reliably extract and compare the field-effect mobility from the transfer characteristics of OFETs has been presented. This method is based on the modification of the standard MOSFET equations to include the gate bias dependence of the charge carrier mobility, which can more physically be described as a dependence on the charge carrier density in the channel. We have shown that the use of the standard MOSFET equations to extract the mobility can give significantly overestimated results, in both the linear and saturation regimes, and this should be kept in mind when comparing the electrical performance of devices evaluated in this manner. The proposed method was used to extract the field-

effect mobility from the transfer characteristics measured at different temperatures and the temperature dependence of the relevant parameters was presented. We observed that the field-effect mobility was thermally activated, with an activation energy (E_a) that depends on the applied gate bias and has a value of approximately 0.2eV. These results agree with previously published results, demonstrating the validity of the OFET parameter extraction method described in this paper.

The source and drain contact resistance and intrinsic device performance (i.e., intrinsic field-effect mobility and threshold voltage) have been characterized using the transverse line method (TLM). The temperature dependence and activation energies of each parameter have been found and agree with results from other measurements. These results indicate that the electrical contact between the organic semiconductor and the source/drain electrodes exhibits Schottky-like behavior at low V_{DS}, which gradually changes to a space charge limited current behavior as V_{DS} is increased.

The electrical performance of the F8T2-based OFETs under high gate-to-source and drain-to-source electric fields has also been characterized and presented. These results indicate that, even though these devices exhibit a significant degree of instability (i.e., threshold voltage shifts), they show promise for use in applications such as electronic paper that require high voltages.

References

[1] S. Martin, J. Y. Nahm, and J. Kanicki, "Gate-planarized organic polymer thin-film transistors," *J. Elect. Mat.*, vol. 31, pp. 512–519, 2002.

[2] S. Martin and J. Kanicki, "Organic polymer thin-film transistors for active-matrix flat panel displays?" *Proc. of the IDRC 2002*, pp. 25–28, 2002.

[3] S. Martin, M. C. Hamilton, and J. Kanicki, "Organic polymer thin-film transistors for active-matrix flat panel displays?" *J. SID.*, vol. 11, pp. 543–549, 2003.

[4] J. H. Lan and J. Kanicki, "Planarized copper gate hydrogenated amorphous-silicon thin-film transistors for am-lcd's," *IEEE Electron Device Lett.*, vol. 20, pp. 129–131, 1999.

[5] R. R. Troutman and A. Kotwal, "A device model for the amorphous-silicon staggered-electrode thin-film transistor," *IEEE Trans. Electron Devices*, vol. 36, pp. 2915–2922, 1989.

[6] R. F. Pierret, *Semiconductor Device Physics*. Reading, MA: Addison-Wesley, 1996.

[7] R. F. Pierret, *Field Effect Devices*, 2nd ed., ser. Modular Series on Solid State Devices, G. W. Neudeck and R. F. Pierret, Eds. Reading, MA: Addison-Wesley, 1990, vol. IV.

[8] Y. Tsividis, *Operation and Modeling of The MOS Transistor*, 2nd ed. Boston, MA: WCB/McGraw-Hill, 1999.

[9] G. Horowitz and P. Delannoy, "An analytical model for organic-based thin-film transistors," *J. Appl. Phys.*, vol. 70, pp. 469–475, 1991.

[10] A. Rolland, J. Richard, J.-P. Kleider, and D. Mencaraglia, "Electrical properties of amorphous silicon transistors and MIS devices: comparative study of top nitride and bottom nitride configurations," *J. Electrochem. Soc.*, vol. 149, pp. 3679–3683, 1993.

[11] G. Horowitz, "Organic field-effect transistors," *Adv. Mat.*, vol. 10, pp. 365–377, 1998.

[12] C. D. Dimitrakopoulos and D. J. Mascaro, "Organic thin-film transistors: A review of recent advances," *IBM J. Res. and Dev.*, vol. 45, pp. 11–27, 2001.

[13] T. N. Jackson, Y. Lin, D. J. Gundlach, and H. Klauk, "Organic thin-film transistors for organic light-emitting flat-panel display backplanes," *IEEE J. Select. Topics Quantum Electron.*, vol. 4, pp. 100–104, 1998.

[14] A. R. Brown, C. P. Jarrett, D. M. deLeeuw, and M. Matters, "Field-effect transistors made from solution-processed organic semiconductors," *Synth. Met.*, vol. 88, pp. 37–55, 1997.

[15] M. C. J. M. Vissenberg and M. Matters, “Theory of the field-effect mobility in amorphous organic transistors,” *Phil. Rev. B*, vol. 57, pp. 12 964–12 967, 1988.

[16] G. Paasch, T. Lindner, and S. Scheinert, “Variable range hopping as possible origin of a universal relation between conductivity and mobility in disordered organic semiconductors,” *Synth. Met.*, vol. 132, pp. 97–104, 2002.

[17] G. Horowitz, R. Hajlaoui, R. Bourguiga, and M. Hajlaoui, “Theory of the organic field-effect transistor,” *Synth. Met.*, vol. 101, pp. 401–404, 1999.

[18] G. Horowitz, “Tunnel current in organic field-effect transistors,” *Synth. Met.*, vol. 138, pp. 101–105, 2003.

[19] F. Garnier, G. Horowitz, D. Fichou, and A. Yassar, “Molecular order in organic-based field-effect transistors,” *Synth. Met.*, vol. 81, pp. 163–171, 1996.

[20] J. G. Laquindanum, H. E. Katz, A. J. Lovinger, and A. Dodabalapur, “Morphological origin of high mobility in pentacene thin-film transistors,” *Chem. Mater.*, vol. 8, pp. 2542–2544, 1996.

[21] D. J. Gundlach, Y. Y. Lin, T. N. Jackson, S. F. Nelson, and D. G. Schlom, “Pentacene organic thin-film transistors - molecular ordering and mobility,” *IEEE Electron Device Lett.*, vol. 18, pp. 87–89, 1997.

[22] W. Geens, D. Tsamouras, J. Poortmans, and G. Hadziioannou, “Field-effect mobilities in spin-cast and vacuum-deposited PPV-type pentamers,” *Synth. Met.*, vol. 122, pp. 191–194, 2001.

[23] W. Geens, S. E. Shaheen, B. Wessling, C. J. Brabec, J. Poortmans, and N. S. Sariciftci, “Dependence of field-effect hole mobility of PPV-based polymer films on the spin-casting solvent,” *Org. Electron.*, vol. 3, pp. 105–110, 2002.

[24] C. Tanase, E. J. Meijer, P. W. M. Blom, and D. M. deLeeuw, “Local charge carrier mobility in disordered organic field-effect transistors,” *Org. Electron.*, vol. 4, pp. 33–37, 2003.

[25] P. V. Necliudov, M. S. Shur, D. J. Gundlach, and T. N. Jackson, “Modeling of organic thin film transistors of different designs,” *J. Appl. Phys.*, vol. 88, pp. 6594–6597, 2000.

[26] G. Horowitz, R. Hajlaoui, D. Fichou, and A. E. Kassmi, “Gate voltage dependent mobility of oligothiophene field-effect transistors,” *J. Appl. Phys.*, vol. 85, p. 3202, 1999.

[27] C. Detcheverry and M. Matters, “Device simulation of all-polymer thin-film transistors,” *Proc. of ESSDERC 2000*, pp. 328–331, 2000.

[28] G. Merckel and A. Rolland, “A compact CAD model for amorphous silicon thin film transistors simulation - I. d.c. analysis,” *Sol. State Electron.*, vol. 39, p. 1231, 1996.

[29] T. Leroux, “Static and dynamic analysis of amorphous-silicon field-effect transistors,” *Sol. State Electron.*, vol. 29, pp. 47–58, 1986.

[30] S. Kishida, Y. Naruke, Y. Uchida, and M. Matsumura, “Theoretical analysis of amorphous-silicon field-effect-transistors,” *Jpn. J. Appl. Phys.*, vol. 22, pp. 511–517, 1983.

[31] S. Martin, J. Kanicki, and Y. Ugai, "Top-gate a-Si:H TFTs: a-Si:H thickness effect and electrical instabilities," *Proc. of the IDRC 1999*, pp. 45–48, 1999.

[32] M. C. Hamilton, S. Martin, and J. Kanicki, "Field-effect mobility of organic polymer thin-film transistors," *Chem. Mater.*, vol. 16, pp. 4699–4704, 2004.

[33] T. Tiedje and A. Rose, "A physical interpretation of dispersive transport in disordered semiconductors," *Solid State Commun.*, vol. 37, pp. 49–52, 1981.

[34] S. Martin, Y. Feillens, and J. Kanicki, "Five-terminal thin-film transistor structure," *Proc. of the IDRC 2000*, pp. 127–130, 2000.

[35] S. Martin, M. C. Hamilton, and J. Kanicki, "Source/drain contacts in organic polymer thin-film transistors," *Mat. Res. Soc. Symp. Proc.*, vol. 771, pp. 163–168, 2003.

[36] G. B. Blanchet, C. R. Fincher, M. Lefenfeld, and J. A. Rogers, "Contact resistance in organic thin film transistors," *Appl. Phys. Lett.*, vol. 84, pp. 296–298, 2004.

[37] I. yagi, K. Tsukagoshi, and Y. Aoyagi, "Direct observation of contact and channel resistance in pentacene four-terminal thin-film transistor patterned by laser ablation method," *Appl. Phys. Lett.*, vol. 84, pp. 813–815, 2004.

[38] B. H. Hamadani and D. Natelson, "Temperature-dependent contact resistances in high-quality polymer field-effect transistors," *Appl. Phys. Lett.*, vol. 84, pp. 443–445, 2004.

[39] H. Klauk, G. Schmid, W. Radlik, W. Weber, L. Zhou, C. D. Sheraw, J. A. Nichols, and T. N. Jackson, "Contact resistance in organic thin film transistors," *Solid-State Electron.*, vol. 47, pp. 297–301, 2003.

[40] L. Bürgi, T. J. Richards, R. H. Friend, and H. Sirringhaus, "Close look at charge carrier injection in polymer field-effect transistors," *J. Appl. Phys.*, vol. 94, pp. 6129–6137, 2003.

[41] R. J. Chesterfield, J. C. McKeen, C. R. Newman, C. D. Frisbie, P. C. Ewbank, K. R. Mann, and L. L. Miller, "Variable temperature film and contact resistance measurements on operating n-channel organic thin film transistors," *J. Appl. Phys.*, vol. 95, pp. 6396–6405, 2004.

[42] P. V. Necliudov, M. S. Shur, D. J. Gundlach, and T. N. Jackson, "Contact resistance extraction in pentacene thin film transistors," *Solid-State Electron.*, vol. 47, pp. 259–262, 2003.

CHAPTER 3

EFFECTS OF ILLUMINATION ON PF-BASED OFETS

As mentioned earlier in this thesis, several of the proposed applications of OTFTs involve the exposure of the devices to illumination, either by design or unintentionally. For example, OTFTs may be used in a photosensor array as the sensing elements or they may be used in flat-panel displays as the driving circuitry. In either case, it is likely that the OTFTs will be exposed to illumination. Therefore, it is important to understand the physical mechanisms involved with and how the illumination effects the electrical performance of OTFTs.

We have studied the electrical performance of the gate-planarized OFETs based on F8T2 under illumination, as well as the performance of these devices as photodetectors. We found that the OFF-state drain current of the OFET is significantly increased due to the illumination, while a smaller, relative effect is observed on the drain current in the strong accumulation regime. Furthermore, the illumination effectively decreases the threshold voltage of the device and increases the apparent subthreshold swing, while the field-effect mobility of the charge carriers in the polymer channel is unchanged. We have observed full recovery of the devices after the illumination is removed at room temperature. These observations are explained in terms of the photogeneration of excitons due to the absorbed photons. The photogenerated excitons subsequently diffuse and dissociate into free charge

carriers, thereby enhancing the carrier density in the channel of the device. The photogenerated electrons can be trapped by positively charged states, thereby reducing the threshold voltage, while the photogenerated holes contribute to the excess photocurrent measured at the drain.

The first section of this chapter discusses the effect of steady-state, white-light (broadband) illumination on the electrical characteristics of OFETs. We have found broadband responsivities of approximately 0.7mA/W for devices biased in the strong accumulation regime and gate-to-source voltage-independent photosensitivities of approximately 10^3 for devices in the OFF-state. We also determine the flatband voltage of these devices to be about -2.3V.

The second section of this chapter discusses the effect of monochromatic illumination on the electrical characteristics of OFETs and the use of these devices as photosensors. To demonstrate the possible use of OFETs as photosensors, we present the responsivity, photosensitivity (signal-to-noise ratio), external quantum efficiency, noise-equivalent power, and specific detectivity of these devices. The dependence of these parameters on the incident photon energy and irradiance level is described.

3.1 Effects of broadband illumination

3.1.1 Experimental setup

To investigate the effect of steady-state illumination on the electrical performance of our devices, the devices were illuminated from the top, as shown in Figure 3.1(a). The experiments were carried out on a Karl Suss PM8 probe station, using broadband white light from a 150W halogen lamp through a Mitutoyo microscope as the illumination source. The ultraviolet-visible absorption spectrum of a thin-film (1000Å) of F8T2 on a quartz substrate (taken with a Cary 5e UV-Vis-NIR Spectrophotometer) and the spectrum of the

incident light at the sample surface are shown in Figure 3.2. From this figure, we can see that light from the lamp is absorbed mainly in the range of wavelengths from approximately 475 to 525nm (2.6 to 2.4eV). In this wavelength range, the absorption coefficient (α) varies from 2.5×10^5 to $2.5 \times 10^4 \text{cm}^{-1}$, providing a 1/α light absorption depth from 400 to 4000Å. Since the thickness of the F8T2 film is only 1000Å, we can assume that the irradiance inside the polymer film at the channel is approximately equal to the irradiance at the film surface (i.e., the photons are uniformly absorbed throughout the polymer film). It was also assumed that the lateral distribution of light was uniform. The incident light irradiance at the surface of the film, measured using an International Light SED625 thermopile detector connected to an International Light IL1700 research radiometer, was controlled from 0 to 2.9W/cm^2. The light delivered to the device was focused to a spot size approximately equal to the area of the device and the entire channel of the device was illuminated as shown in Figure 3.1(b).

We measured the OFET electrical characteristics in the dark and under various levels of illumination at room temperature using an HP4156 semiconductor parameter analyzer controlled by Interactive Characterization Software (Metrics). The bias conditions used to measure the transfer characteristics, in both the linear and saturation regimes, and the output characteristics of our devices, are given in Table X. We chose to measure the transfer characteristics from the ON-state to the OFF-state (i.e., from $V_{GS} = -40V$ to $20V$). This measurement method was chosen because it provides very reproducible data, with a variation in the ON-current of less than ±5% for the linear regime transfer characteristics measured back-to-back in the dark. This allows reliable comparison of the electrical performance of the device in the dark and under illumination.

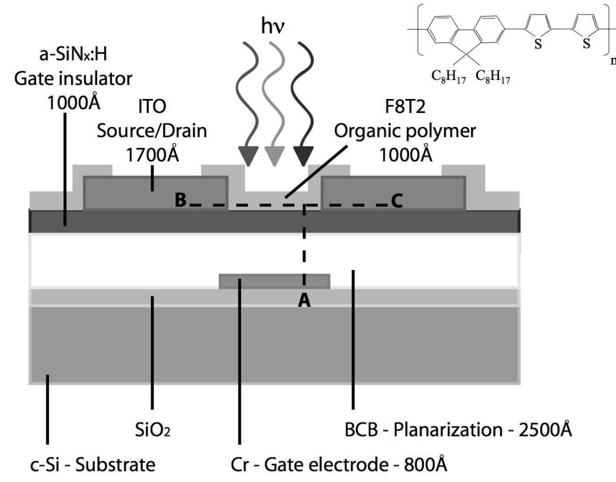

(a)

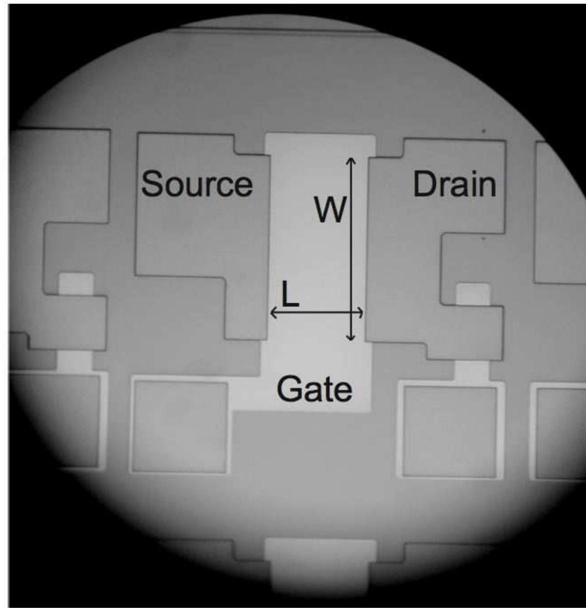

(b)

Figure 3.1: (a) Cross-section of device structure and chemical structure of F8T2. (b) Top-view of illuminated device showing gate, source, and drain. For this device, L = 56μm, W = 116μm and source/drain-gate overlap is 5μm

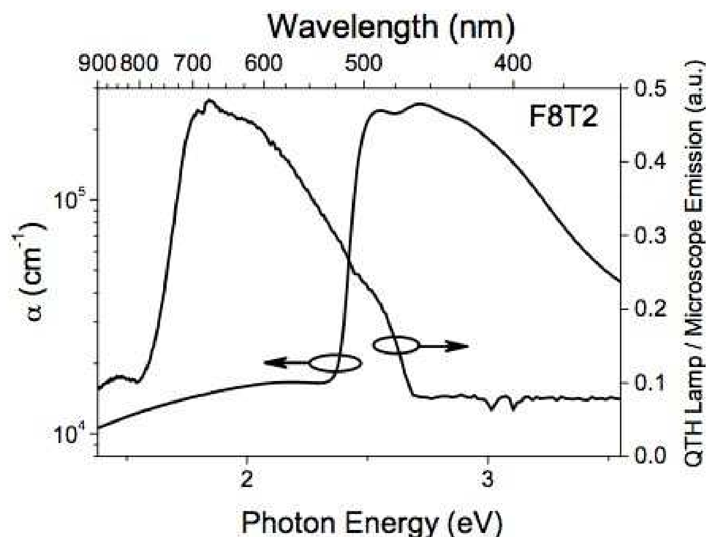

Figure 3.2: Absorption coefficient of F8T2 and light emission spectrum of incident light as a function of the photon energy.

3.1.2 Device under illumination

We have observed very strong effects of steady-state, broadband illumination on the electrical performance of OFETs. The effects are evident when we compare the linear regime transfer characteristics of a device in the dark to those of the same device under illumination as shown in Figure 3.3(b). From this figure, we can see that the drain current in the OFF-state is significantly increased by several orders of magnitude, while a milder effect of illumination on the drain current in the strong accumulation regime is observed. The significant increase of drain current in the OFF-state, when the device is under illumination, can be attributed to the enhancement of the carrier density in, and therefore the conductivity of, the channel of the device due to the photogeneration of excitons in the polymer.

There are four basic photocarrier generation processes in solid organic polymers that can contribute to the enhancement of the carrier density in the polymer channel of the device [1]:

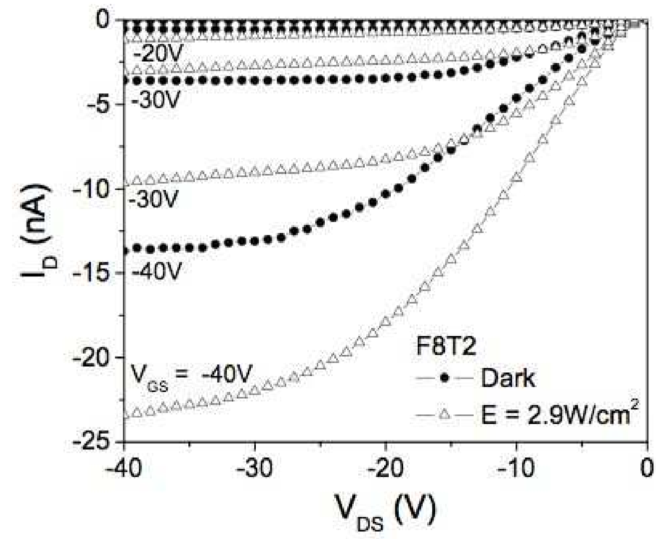

(a)

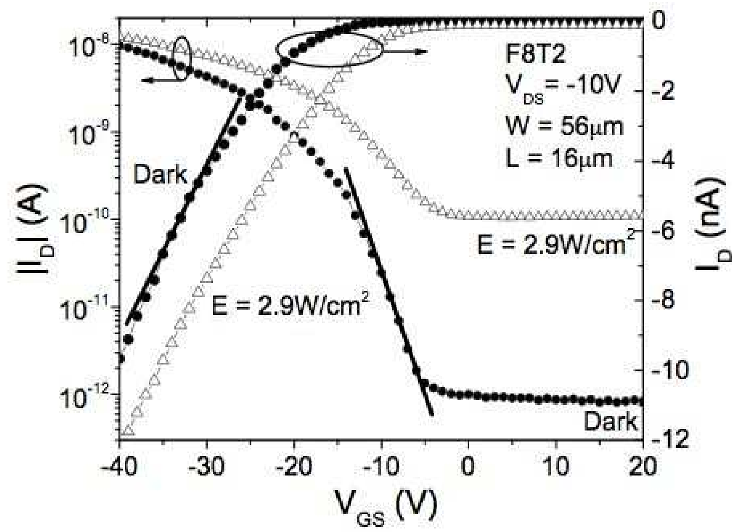

(b)

Figure 3.3: (a) Output characteristics of OFET in the dark and illuminated at $2.9W/cm^2$. (b) Transfer characteristics of OFET in the dark and illuminated at $2.9W/cm^2$

a) Exciton formation and subsequent dissociation (electric field, surface, or impurity induced) into free carriers;

b) Direct, band-to-band excitation of electrons;

c) Photoinjection of carriers from the metal source/drain electrodes into the polymer;

d) Detrapping of carriers trapped in localized gap states in the polymer.

In this work, we expect that the most likely carrier photo-generation process is through the exciton route. Photons with the proper energy are absorbed in the polymer, forming an exciton (i.e., a bound electron-hole pair) as shown schematically in Figures 3.4(a) and 3.4(b).

While we have not directly investigated the properties of the excitons that are photogenerated in F8T2, we should comment on the experimental methods that can provide insight into the kinetics and energies associated with this phenomenon. Photoluminescence of a thin film semiconductor, when performed at a very low temperature (i.e., near 4K), can provide information about the binding energy and kinetics of excitons [2]. Additionally, electro-optical absorption (i.e., field-dependent absorption) can provide further information about the binding energies and dissociation properties of excitons in a polymer film [3]. Additional methods, such as photothermal deflection spectroscopy and photoluminescence quenching in a thin-film transistor structure can further characterize the exciton by providing the sub-gap absorption spectrum and information about diffusion and dissociation of the exciton, respectively [4]. We should also note that the groups of Friend have, in numerous reports, observed the formation, trapping and dissociation of excitons in polyfluorene derivatives and blends [5, 6]. Additionally, the exciton energy and binding energy can be estimated from optical absorption combined with either cyclic voltammetry (CV), photocurrent measurements or light-induced electron spin resonance (LESR). We find that the onset of the optical absorption in F8T2 occurs near approximately 2.45eV, as

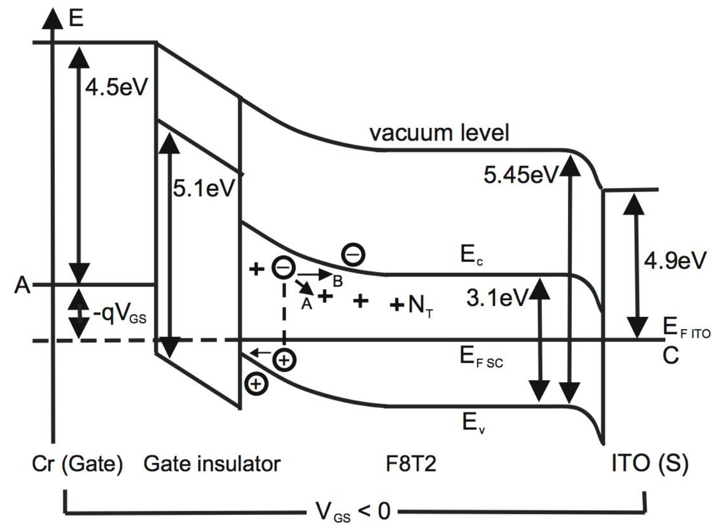

(a)

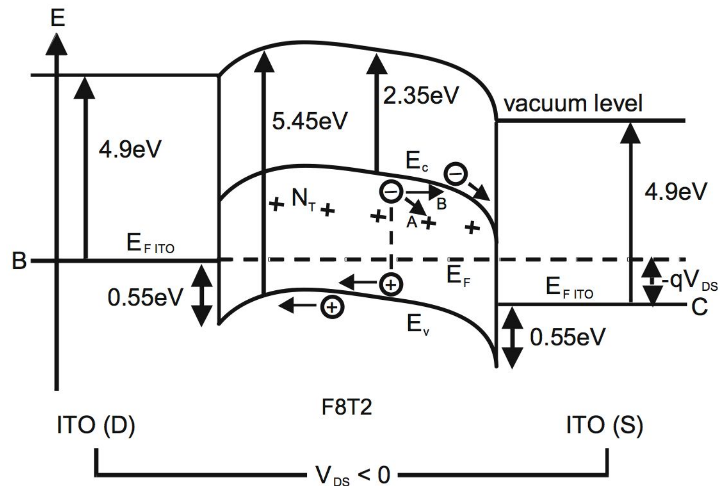

(b)

Figure 3.4: Proposed energy band diagram of OFET under illumination in the region from (a) the gate electrode to the source electrode (i.e., following the line A to C in Figure 3.1(a)) and (b) the drain electrode to the source electrode (i.e., following the line B to C in Figure 3.1(a)).

shown in Figure 3.2. By comparing this to the HOMO-LUMO gap from C-V of 2.7eV, we find a binding energy of the exciton in F8T2 to be roughly 0.3 to 0.4 eV. This binding energy is consistent with results obtained by other groups for the energetic properties of excitons in polyfluorenes [7]. These results confirm that the exciton route is a possible and probable physical mechanism that leads to the photogeneration of charge carriers in polyfluorene-based organic semiconductors.

The photo-generated exciton diffuses to a dissociation site (i.e., defect, impurity, or surface state) and dissociates into an electron and hole. Once generated, these charge carriers begin to move under the influence of the electric field (from the applied V_{DS} and V_{GS}) and in opposite directions down the channel of the OFET. With our biasing conditions, the electrons move away from the gate and drain and towards the source, while the holes move towards the gate and drain and away from the source. Some of the photo-generated electrons are trapped into, and neutralize positively charged states (N_T) that contribute to the large initial negative threshold voltage, thereby reducing the threshold voltage. The origin of these positively charged states is presently under investigation. The photo-generated holes are collected at the drain electrode (by the corresponding transfer of an electron from the drain electrode into the valence band of the polymer). A photo-current is measured that is larger than the drain current in the dark, especially when the device is operated in the OFF-state. These processes are shown schematically in the proposed energy band diagrams presented in Figures 3.4(a) and 3.4(b). Figure 3.4(a) shows the energy band diagram of a device under illumination, normal to the channel of the device (i.e., in the direction from the gate, through the gate insulator, and through the semiconductor) near the source electrode. Figure 3.4(b) shows the energy band diagram of a device under illumination, in the direction of the channel of the device (i.e., in the direction from the drain electrode, through the semiconductor, to the source electrode). When the device is oper-

ated in the strong accumulation regime, the relative effect of the illumination on the drain current is much smaller compared to its effect in the OFF-state. This can be explained by the overwhelming effect of the gate voltage on the concentration of accumulated carriers in the channel of the device, at the levels of illumination used in this study, and is explained in further detail below.

3.1.3 Experimental results and analysis

We have investigated the effect of the illumination irradiance level. Figure 3.5 presents the linear regime transfer characteristics of our OFET in the dark and under various levels of illumination up to approximately 2.9W/cm^2. From this figure, we can see that the OFF-state drain current of the device is strongly dependent on the level of illumination. As the illumination level is increased, the drain current is increased since the photogeneration rate of excitons (and therefore charge carriers) in the channel of the device increases as the illumination intensity is increased.

Figure 3.6 presents the variation of the OFF-state drain current, ON-state drain cur-

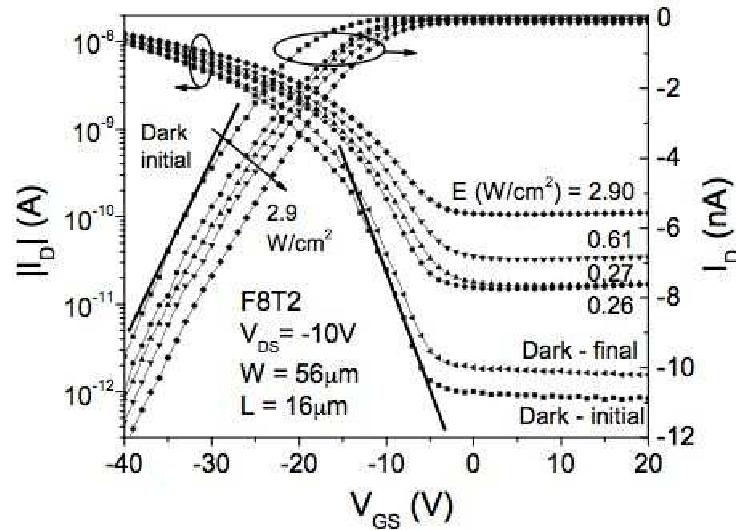

Figure 3.5: Transfer characteristics of OFET in the dark and under various irradiance levels.

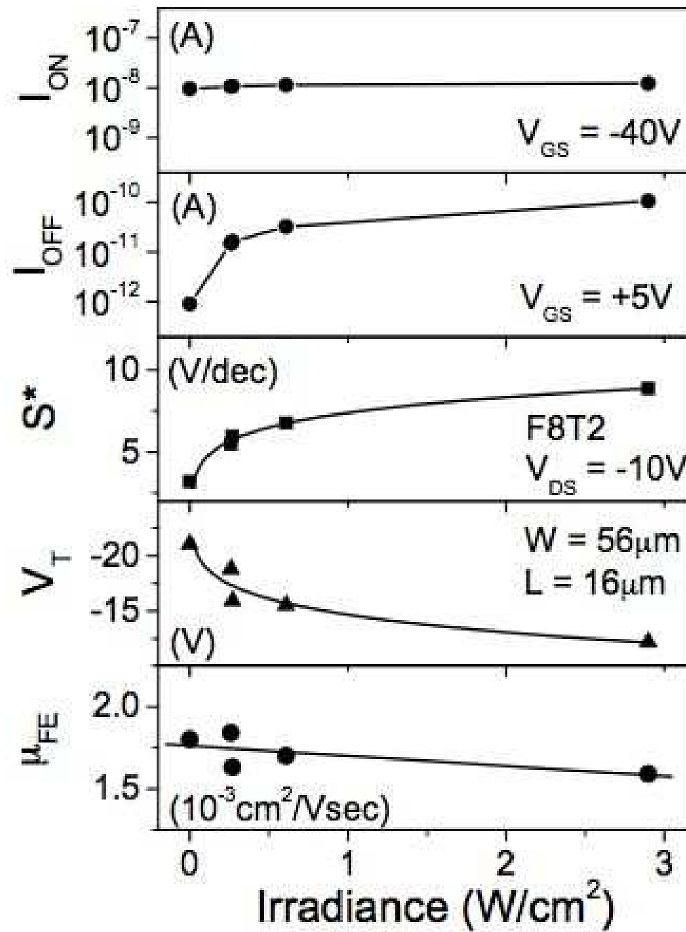

Figure 3.6: Dependence of ON-state drain current, OFF-state drain current, field-effect mobility, threshold voltage, and apparent subthreshold slope on irradiance. μ_{FE}, V_T, and S^* extracted from the data in Figure 3.5, using equations (2.2) and (2.4). Lines are provided as guides to the eye.

rent, linear regime field-effect mobility, threshold voltage and apparent subthreshold swing (S^*) with illumination irradiance. From this figure, we see that the relative change in the OFF-state drain current, as the irradiance level is increased, is much larger than the relative change in the ON-state drain current, as stated above. The other electrical parameters were extracted from the linear regime transfer characteristics, of Figure 3.5, using equations (2.2) and (2.4) from above. From Figure 3.6, it is evident that as the illumination level is increased, the threshold voltage of the device is effectively reduced and the apparent subthreshold swing is increased. We speculate that the reduction of the threshold voltage is due to the compensation of positively charged states (N_T, that contribute to the large initial negative threshold voltage) by the photo-generated electrons (i.e., the electrons are trapped by positively charged states). This effect can be understood by examining equations (2.3a) and (2.3b) for the threshold voltage of a MOSFET. If we use this equation to explain the behavior of OFETs under illumination, we see that a reduction of N_T corresponds to a reduction of Q_{eff}, which leads to a reduction of the threshold voltage. In Figure 3.7, we present the transfer characteristics plotted using the effective gate-to-source voltage (i.e., I_D versus $V_{GS} - V_T$) at various illumination levels. From this figure, we can see that, indeed, the major effect of the illumination is a reduction of the threshold voltage. Conversely, the field-effect mobility is relatively unaffected, indicating that the electronic structure of the polymer is not affected by the illumination. Additionally, we conclude that there is negligible change in temperature due to illumination of the device, since the field-effect mobility is expected to increase with temperature in conjugated polymer semiconductors [8–10]. The apparent increase in the subthreshold swing with increasing illumination can be attributed to the enhanced conductivity of the channel of the device in the OFF-state due to the increase in carrier density brought about by the illumination. This is an additive effect, in that the illumination provides another means by which to control the density of charge

carriers in the channel and can be thought of as a second gate. When either of the gates is turned off (i.e., $V_{GS} \geq 0$V applied or no incident illumination), the effect of the other gate is maximized. For instance, the ON/OFF ratio (I_{ON}/I_{OFF}) is maximum for no illumination and I_{Dillum}/I_{Ddark} is maximum for a device biased in the OFF-state. The observed result is an apparent decrease in the effectiveness of the applied gate bias over the channel (i.e., larger apparent subthreshold swing) with increasing irradiance. However, as shown in Figure 3.7, we see that the subthreshold swing of all curves, dark and illuminated, are similar. The increase in the apparent subthreshold swing is an artifact of the extraction method using equation (2.4) under illumination. Using the relation of equation (2.5), the density of states can be connected to the subthreshold swing and can be extracted from the transfer characteristics in the dark and under illumination. From Figure 3.7, we conclude that, since the subthreshold swing is not significantly affected by the illumination, the density of states in the polymer is not significantly affected by the illumination.

Alternatively, the observed results can be understood by investigating the band-

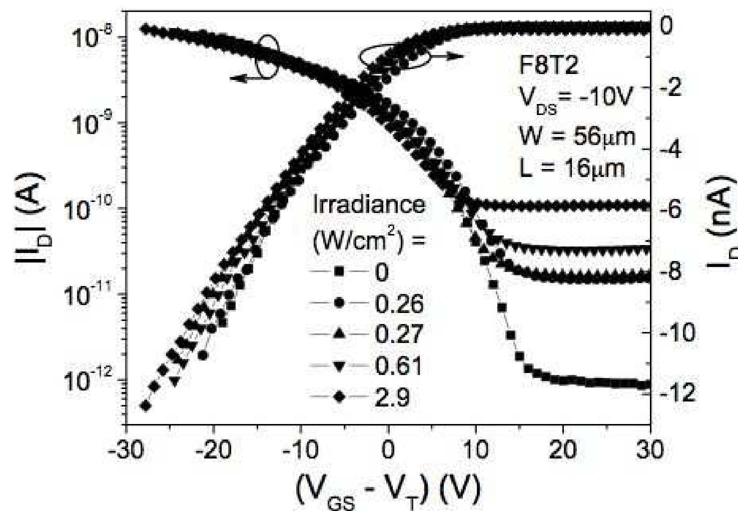

Figure 3.7: Threshold voltage-normalized transfer characteristics (i.e., I_D versus $V_{GS} - V_T$) of OFET in the dark and illuminated at various irradiance levels.

bending and energy level structure in the organic semiconductor in the direction normal to the channel of the device. This theory has been developed for thin-film transistors (TFTs) based on amorphous semiconductor materials, namely hydrogenated amorphous silicon (a-Si:H) TFTs [11–13]. The non-equilibrium situation of the illuminated device is characterized by a splitting of the equilibrium Fermi level into two quasi-Fermi levels; one for holes and one for electrons. The splitting is dependent on the intensity and energy of the incident illumination. The band-bending (i.e., the effect the gate has on the accumulated carrier concentration in the channel), at a certain gate bias, is reduced in the illuminated device due to the increased density of charge carriers in the channel from photogeneration. Experimentally, we observe this effect as a reduction in the threshold voltage and an increase in the apparent subthreshold swing.

A useful figure of merit is the responsivity (R in A/W) of the device, which can be defined as:

$$R = \frac{I_{ph}}{P_{inc}} = \frac{I_{Dillum} - I_{Ddark}}{E \times A} \tag{3.1}$$

where I_{ph} is the drain photocurrent, P_{inc} is the power incident on the channel of the device, I_{Dillum} is the drain current under illumination, I_{Ddark} is the drain current in the dark, E is the irradiance of the incident light and A is the effective device area. The effective device area, A, is calculated from the geometry of the device. A is equal to the effective channel length ($L + 2L_p$) times the effective channel width ($W + 2L_p$), where L_p is the diffusion length of the holes. For $L_p \ll L, W$, which is the case here (i.e., 100nm≪6000nm), the equation reduces to $L \times W$. A plot of R versus gate bias is shown in Figure 3.8. From this plot, we observe that the responsivity is higher in the strong accumulation regime than in the OFF-state. This is evidence of a gain mechanism in the device, since the number of photo-generated carriers mostly depends on the intensity of the incident illumination, and not on the applied gate bias. We have observed values of R in excess of 0.7mA/W for

the case of broadband illumination. This value is several orders of magnitude lower than reported responsivities of 0.1 to 0.5A/W of other organic photodetectors under monochromatic illumination [14, 15]. However, the responsivity of the present devices is expected to be significantly larger for a monochromatic light source having a photon energy corresponding to the maximum absorption of the polymer as compared to the present case in which most of the incident light is not absorbed [16, 17].

In Figure 3.9, we present the dependence of the responsivity on the illumination irradi-

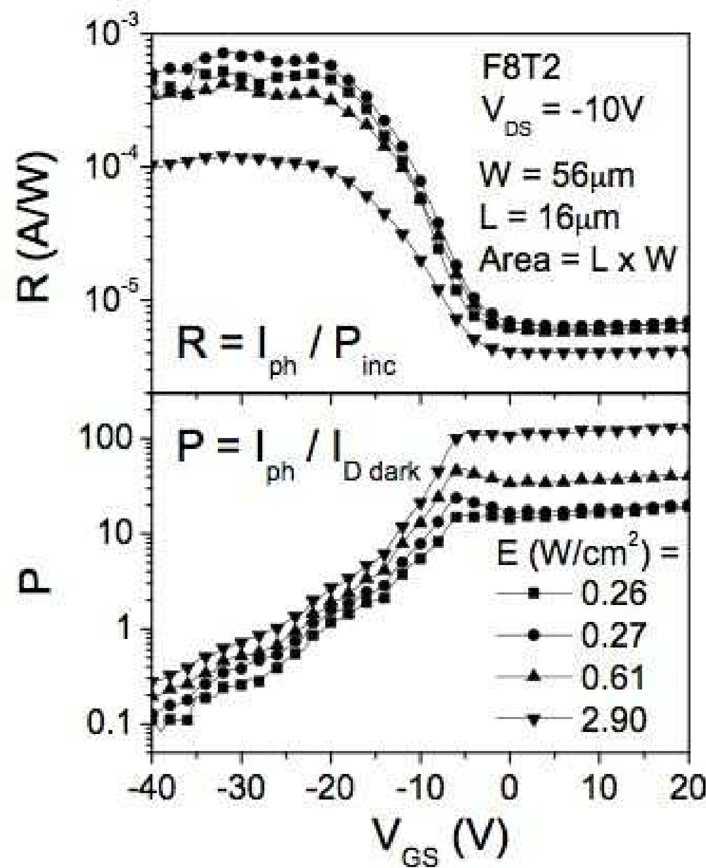

Figure 3.8: OFET responsivity (R) and photosensitivity (P) versus V_{GS} for various irradiance levels taken from data for the same device shown in Figure 3.7.

ance. We can see from this figure that the device has the highest responsivity when biased

in the strong accumulation regime, and the responsivity decreases with increasing irradiance. The decrease of responsivity as irradiance is increased is due to the saturation of the photocurrent, which can be caused by several factors. One factor influencing the photocurrent is the efficiency of charge transport through the channel of the device at higher irradiance levels. In other words, even though more excitons, and therefore more holes, are photogenerated at higher irradiance levels, these carriers may not be able to contribute to the photocurrent due to the limiting nature of the charge transport mechanisms, such as space-charge-limited currents, in the polymer. A second cause of the photocurrent saturation at higher irradiance levels is exciton-exciton annihilation, i.e., at higher irradiance levels, the enhanced density of excitons causes the excitons to interact with each other.

A second useful figure of merit is the photosensitivity (P), or signal (photo-current) to noise (dark-current) ratio, of the device, which can be approximated as [18]:

$$P = \frac{signal}{noise} = \frac{I_{ph}}{I_{Ddark}} = \frac{(I_{Dillum} - I_{Ddark})}{I_{Ddark}} \tag{3.2}$$

where all terms have been previously defined. The dependence of the photosensitivity on the gate voltage (V_{GS}) is shown in Figure 3.8. From this plot, we can see that P is a maximum in the OFF-state and is minimum in the strong accumulation regime, consistent with the observations and comments made above about the drain current under illumination. We have observed values of P in excess of 10^3 in the OFF-state at a broadband illumination level of 2.9W/cm^2. From Figure 3.8, we can also see that P is not a strong function of V_{GS} in the OFF-state. In fact, the slight dependence on V_{GS} and the little noise of the $P - V_{GS}$ curve are mainly due to the extremely low ($<10^{-12}$A) OFF-state drain current of our OFETs in the dark. The high sensitivity to illumination and non-dependence on the gate-to-source bias in the OFF-state are very useful characteristics of the device if it is to be used to detect light at low applied voltages (i.e., low power consumption). Figure 3.8 also shows the dependence of the photosensitivity on V_{GS} for several values of illumination

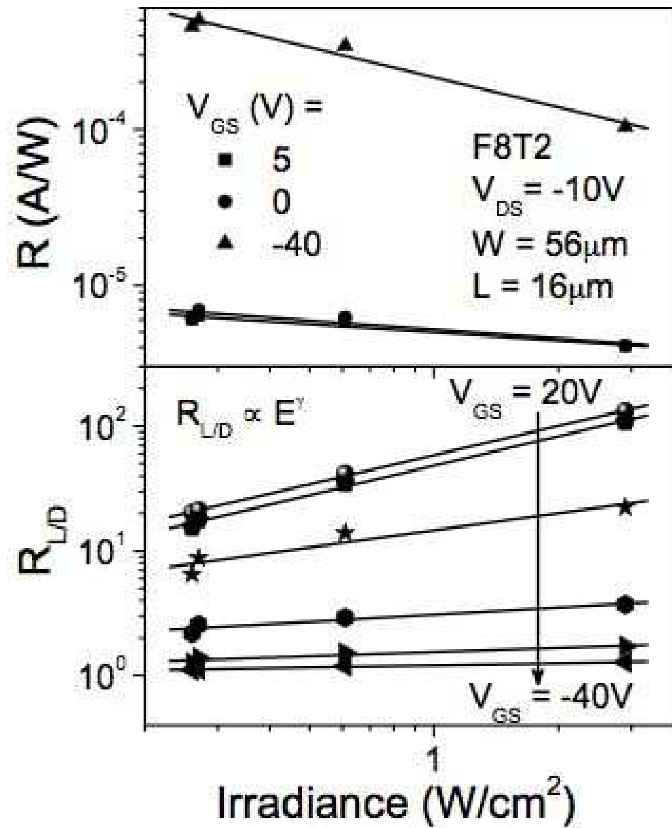

Figure 3.9: OFET responsivity (R) and photoresponse ($R_{L/D}$) versus irradiance for various V_{GS}.

irradiance. We can see that, as expected, P increases with increasing illumination irradiance. However, the photosensitivity for a device biased in the OFF-state is nearly linear with the irradiance level, giving a limited dynamic range that may not be very satisfactory for certain detector applications.

A related measure is the ratio of total drain current under illumination to drain current in the dark, which is referred to as the photoresponse and is defined as [19]:

$$R_{L/D} = \frac{I_{Dillum}}{I_{Ddark}} \tag{3.3}$$

A plot of $R_{L/D}$ versus E for various V_{GS}, as shown in Figure 3.9, shows that $R_{L/D}$ exhibits a power law dependence on the illumination according to the following equation:

$$R_{L/D} \propto E^{\gamma} \tag{3.4}$$

In this equation, E is the illumination irradiance and the γ-power exponent is a function of the applied V_{GS}. We should note that the γ power exponent described in this chapter is not directly related to the γ exponent used previously in section 2.3. We can describe the dependence of γ on V_{GS}, as shown in Figure 3.10, using a model developed by Harm, Schropp, and Verwey for TFTs based on amorphous semiconductors [11, 12, 20]. This model was formulated with the assumption that: the total density of states is constant around mid-gap; there is a symmetrical overlap of donor and acceptor states around mid-gap; the field-effect is governed by the bulk states, as opposed to the interface states; and that, under illumination, the Fermi level splits into quasi-Fermi levels (one for holes and one for electrons). We believe that these assumptions are not too specific to a-Si, the amorphous semiconductor used by Harm, et al., therefore we have applied this model to the case of our amorphous organic semiconductor-based OFET under illumination.

The dependence of γ on V_{GS}, as shown in Figure 3.10, can be modeled by the following equations:

$$\gamma(V_{GS}) = \begin{cases} \gamma_0 \left(\dfrac{V_{GC} - V_{GS}}{V_{GC} - V_{FB}} \right), & \text{for } V_{GS} < V_{FB} \text{ V} \quad (3.5a) \\ \gamma_0, & \text{for } V_{GS} > V_{FB} \text{ V} \quad (3.5b) \end{cases}$$

In this equation, γ_0 is a material dependent constant, V_{GS} is the applied gate-to-source bias, V_{FB} is the flat-band voltage (i.e., the gate voltage necessary to achieve the flat-band condition), and V_{GC} is the critical gate voltage at which the drain current under illumination is ideally equal to the drain current in the dark (i.e., $I_{Dillum}/I_{Ddark} = 1$ at V_{GC} for the ideal case) and is given by:

$$V_{GC} = \frac{\sqrt{\epsilon_{semi}} d_{ins} \beta}{\epsilon_{ins} \sqrt{\epsilon_0}} \tag{3.6}$$

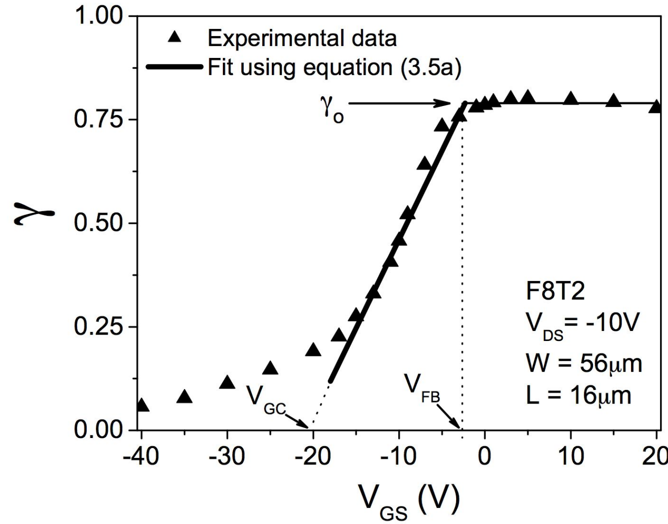

Figure 3.10: Power exponent γ (experimental and fit using equations (3.5a) and (3.5b)) versus V_{GS}

In this equation, ϵ_{semi} is the dielectric constant of the semiconductor (= 2.6), ϵ_{ins} is the effective dielectric constant of the insulator (= 2.3), d_{ins} is the effective thickness of the insulator (= 2700Å) and β is defined as:

$$\beta = \frac{\left(2N_f\right)^{3/2}}{L} \tag{3.7}$$

where L is the linear slope of the localized state distribution near the middle of the supposed band-gap and $2N_f$ is the total density of states at midgap. Note that this linear slope L is not related to the channel length L used to describe the geometry of the device. In Figure 3.10, we see that we can fit our data in the region $0 < |V_{GS}| < V_{GC}$ using equation (3.5a) with V_{GC} equal to approximately -21V. This gives a β value of approximately 7.4×10^5. If we assume a value of 10^{18}cm^{-3}eV^{-1} for $2N_f$ (estimated from equation (2.5) with $N_{SS} = 0$), we find that L is equal to 1.4×10^{21}cm^{-3}eV^{-2} from equation (3.7). From experimental data, we estimate γ_0 to be 0.8, while the fit using equation (3.5b) gives a γ_0 value of approximately 0.9. A power-law dependence on the illumination irradiance is expected when trapping and sub-sequent de-trapping, i.e., multi-step hopping, of the carriers

is involved in the channel conduction process.

Using a method similar to that of Schropp, et al [11, 12], we can extract the flat-band voltage (V_{FB}) of the OFETs from Figure 3.10. Since the density of holes in the channel does not increase for applied gate biases from the flat-band voltage to more positive voltages and the source and drain electrodes block electrons coming from the conduction band (i.e., lowest unoccupied molecular orbital, or LUMO level), the ratio of drain current under illumination over drain current in the dark is constant for positive gate voltages. As gate biases from the flat-band voltage to more negative biases are applied, the logarithm of the current ratio is approximately proportional to the band-bending at the interface, which is proportional to $V_{GS} - V_{FB}$. As did Schropp, et al, we assume that the illumination does not cause a shift in the flat-band voltage, and we extract the flat-band voltage from the crossing point of equations (3.5a) and (3.5b). We find the V_{FB} of OFETs based on F8T2 to be equal to -2.3V. According to equations (2.3a) and (2.3b), this negative value of V_{FB} is evidence of an effective charge (i.e., trapped charge) within the channel and contributes to the relatively large value of the threshold voltage of these OFETs.

In Figure 3.11, we present the ratio of drain current under illumination to drain current in the dark versus V_{DS} at several values of V_{GS} spanning the entire range of operating regimes of the device. From this figure, we can see that this ratio is relatively independent of V_{DS}, in the range of biases we have measured. The non-dependence on V_{DS} shows that this range of electric fields is substantial to aid the dissociation of the excitons into free carriers.

It should be noted that the devices undergo full recovery, at room temperature, and relax back to their original state (i.e., OFF-state drain current, threshold voltage, and subthreshold swing values equal to pre-illumination values) after the illumination is removed. This effect can be seen in Figure 3.5 where I_{Dfinal} has nearly returned to $I_{Dinitial}$. This recov-

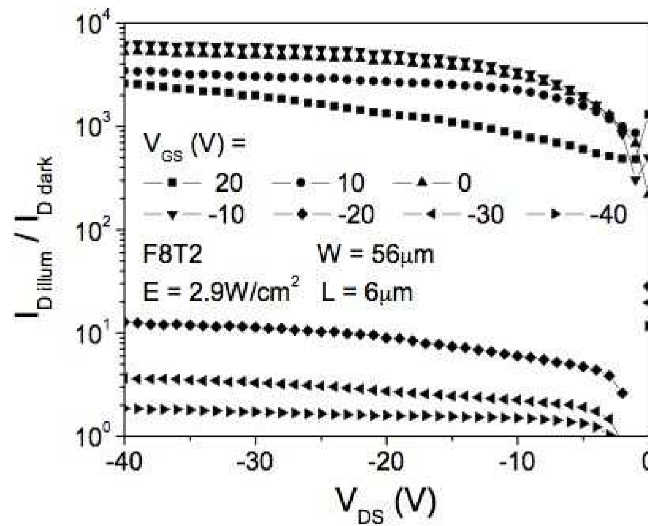

Figure 3.11: I_{Dillum} / I_{Ddark} at maximum irradiance versus V_{DS} at various V_{GS}.

ery takes several minutes, in some cases, when the device is in the air at room temperature. However, exposing the device to higher temperature or illumination at longer wavelengths (i.e., red to infrared) can accelerate the recovery process [21].

3.2 Effects of monochromatic illumination

3.2.1 Experimental setup

The transfer characteristics (drain current versus gate-to-source voltage, $I_D - V_{GS}$) and output characteristics (drain current versus drain-to-source voltage, $I_D - V_{DS}$) of the OFET were measured in the dark and under various levels of monochromatic illumination at room temperature using a Karl Suss PM8 probe station and an HP4156 semiconductor parameter analyzer (using medium integration) controlled by Interactive Characterization Software (Metrics). A 200W mercury xenon (HgXe) arc lamp (Oriel Instruments) was used as the illumination source. The incident wavelength and irradiance (or optical flux) from the HgXe lamp were controlled, using optical interference filters (FWHM < 10nm) and neutral density filters, to provide wavelengths from 435.8 to 690.7nm and irradiance

levels up to approximately $30\mu W/cm^2$ at the surface of the polymer film. After being optically filtered, the light passed through a fiber optic cable and a Mitutoyo microscope, which was used to focus the illumination to a spot size centered on the channel of the device, illuminating the entire channel. The irradiance was measured, at the same location where the device is placed in the light spot, using an International Light Si photodetector (SHD033) with a flat response filter and fiber optic probe connected to an International Light research radiometer (IL1700). All measurements were performed in ambient air at room temperature and we did not observe any dependence of the device performance on room humidity.

It is well known that the electrical characteristics of OFETs exhibit shifts due to measurement (from the application of biases) and other stresses (such as illumination) [21,22]. We have observed that the shifts in the electrical characteristics due to illumination are much more significant than the shifts due to repeated (i.e., back-to-back) measurement in the dark. To compensate for these shifts, while allowing the experiments to be carried out in a reasonable manner, we annealed the devices between measurement sets (15min at 90°C in a vacuum oven). The measurement sequence we have used is as follows. We annealed the device as described above. Then we measured the dark transfer characteristics. The illumination was then switched on and within a few seconds, the illuminated transfer characteristics were measured. This was followed by another anneal, measurement in the dark, measurement under illumination and so on. Therefore, the calculated parameters (see following sections) were found by using the illuminated characteristics compared to the immediately proceeding dark characteristics, with no annealing step between. The annealing procedure removed the shifts caused by measurement and illumination and allowed the device (and its electrical characteristics) to return to the original state (i.e., similar OFF-state drain current, threshold voltage and subthreshold slope) before proceeding with the

next measurement set, thereby providing more reliable results. Though the perturbation of the devices can be fully removed at room temperature, the elevated temperature significantly speeds up the recovery.

The data presented in this section was taken from two randomly chosen devices, one for the measurements using different wavelengths of incident illumination and one for different levels of irradiance. We have observed similar effects for all devices tested, and the device-to-device reproducibility is acceptable, given the current status of organic-based electronics. In several of the following plots, the data is noisy. We believe the noise is mainly due to the small signal amplitudes (or division by small signals for the case of the calculated parameters). The trends in the data presented here have been observed for all devices tested under these measurement conditions.

3.2.2 Device under illumination

As noted above, we have observed very strong effects of steady-state, broadband illumination on the electrical performance of a-Si:H TFTs [19] and OFETs based on F8T2 [16, 23]. In this section, we examine the effects of illumination in more detail by exploring the response of the OFETs to monochromatic illumination at different wavelengths and irradiance levels. In Figure 3.12, we present the threshold-voltage normalized transfer characteristics (drain current versus gate-to-source voltage - threshold voltage, I_D vs. $V_{GS} - V_T$). We plot the transfer characteristics in this manner in order to demonstrate that the major effects of the illumination are a reduction of the threshold voltage and an increase in the OFF-state drain current, while the field-effect mobility and subthreshold slope retain their same value as in the dark. More details on these effects, as well as the dependence on incident photon energy and irradiance are discussed in the following sections.

For the case of our devices, the most likely carrier generation process is through

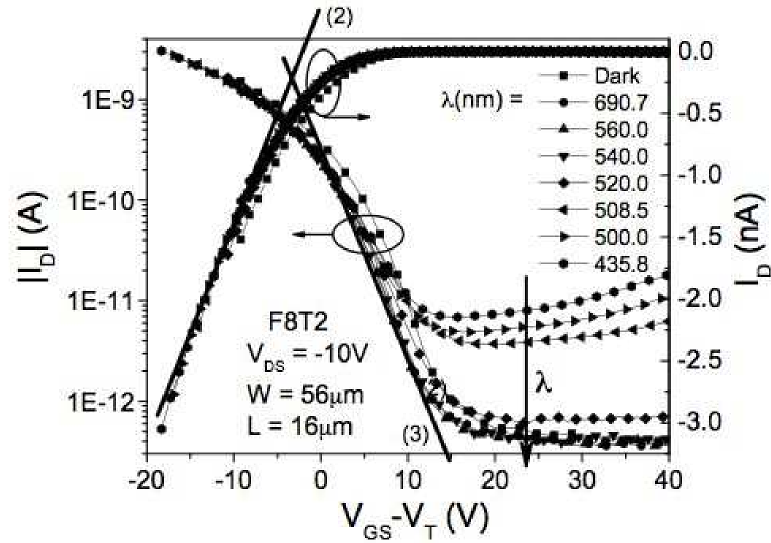

Figure 3.12: Threshold voltage-normalized transfer characteristics of OFET illuminated at different wavelengths/photon energies, measured with a constant optical flux of 5×10^{13} photons/cm^{2}sec. The straight lines are fits using equations (2.2) and (2.4).

the exciton route. Photons with the proper energy are absorbed in the polymer, forming an exciton (i.e., a bound electron-hole pair). The exciton then diffuses to a dissociation site (i.e., defect, impurity, or surface state) and dissociates into a free electron and hole. Once generated, these free charge carriers move under the influence of the applied electric fields (from the applied V_{DS} and V_{GS}) and in opposite directions through the channel of the OFET. Many of the electrons are trapped into, and neutralize positively charged traps (N_T) that contribute to the large negative threshold voltage, thereby reducing the threshold voltage. The photogenerated holes are collected at the drain electrode (by the corresponding transfer of an electron from the drain electrode into the valence band of the polymer). The drain current in the OFF-state is significantly increased, while a smaller increase in the drain current in the strong accumulation regime is observed. The significant increase of drain current in the OFF-state, when the device is under illumination, can be attributed to the enhancement of the carrier density in, and therefore the conductivity of, the chan-

nel of the device due to the photogeneration and dissociation of excitons in the polymer. When the device is operated in the strong accumulation regime, the relative effect of the illumination on the drain current is much smaller compared to the effect in the OFF-state. This can be explained by the overwhelming effect of the gate voltage on the concentration of accumulated carriers in the channel of the device, at the levels of illumination used in this study.

3.2.3 Experimental results and analysis

Dependence on photon energy

The response of the OFETs to monochromatic illumination has been investigated by measuring the transfer characteristics of a device in the dark and under monochromatic illumination at various wavelengths. Figure 3.12 shows the linear regime, threshold voltage-normalized, transfer characteristics of an OFET in the dark and illuminated at 7 wavelengths from 435.8 to 690.7nm with a constant optical flux of approximately 5×10^{13} photons/cm^{2}sec incident on the surface of the polymer film. In Figure 3.2, we show the OFF-state drain current (extracted from Figure 3.12) along with the absorption spectrum of the F8T2 polymer film. From this figure, we can see that light with energy less than 2.4eV (corresponding to the optical gap of the F8T2 films we used) is weakly absorbed and has little effect on the transfer characteristics, while light with higher energy (from 2.4 to 2.8eV) is strongly absorbed, generating more excitons, and therefore has a much larger effect. Further evidence to support this explanation is found when we plot the number of absorbed photons versus the energy of the photons as in Figure 3.2. The total number of absorbed photons was approximated using the incident photon flux, absorption coefficient (taken from Figure 3.2), the effective area of the device ($W \times L$), and the thickness of the polymer.

The dependence of the change in threshold voltage (extracted from the linear regime

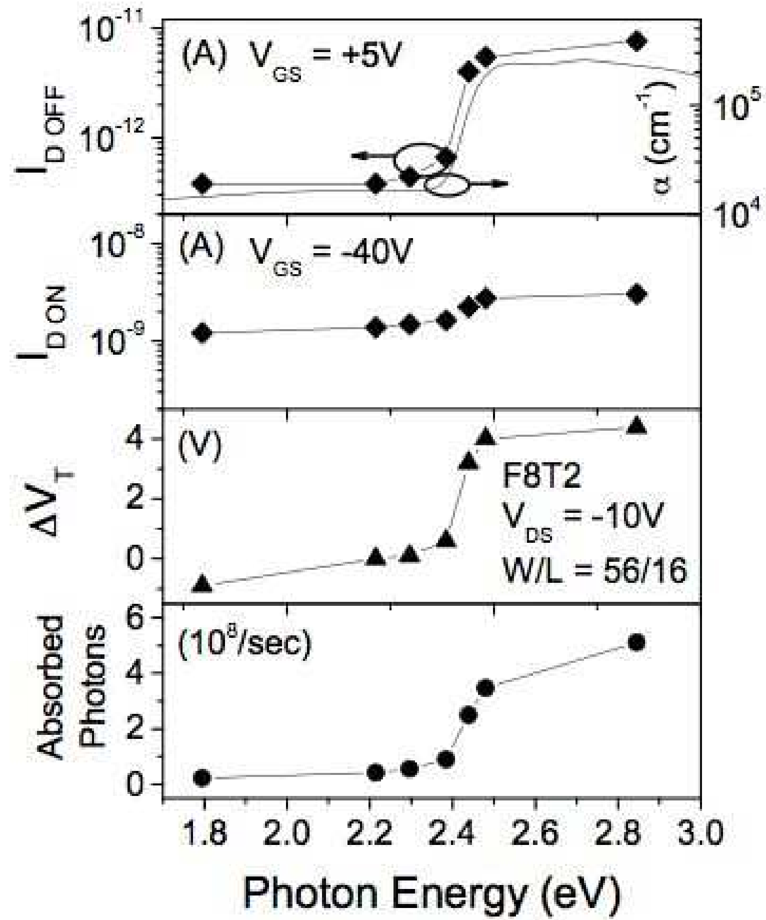

Figure 3.13: Dependence of ON-state drain current, OFF-state drain current, and the change in threshold voltage on the energy of the incident photons. Extracted from the non-threshold voltage-normalized transistor characteristics (not shown), using equations (2.2). Also shown is an estimation of the number of photons absorbed per second in the channel region of the device as a function of the photon energy.

transfer characteristics shown in Figure 3.12 using equation (2.2)) on the energy of the incident photons is shown in Figure 3.13. We can see that the change in threshold voltage is significantly larger for the strongly absorbed light, while little change is observed for light which is weakly absorbed. As explained above, some of the photogenerated electrons become trapped by and compensate positively charged traps, N_T, reducing the threshold voltage, as we have observed for strongly absorbed light and as shown in Figure 3.13 ($\Delta V_T = V_{Tillum} - V_{Tdark}$, therefore a positive ΔV_T corresponds to a reduction of the threshold voltage). N_T can be estimated from the threshold voltage to be approximately 10^{17}cm^{-3}. The change in threshold voltage of 4V, corresponds to a change in N_T, ΔN_T, of approximately 10^{16}cm^{-3}. Further evidence that charge carrier trapping is taking place is provided by the fact that, after illumination, we are able to bring the devices back to their original state (i.e., the transfer characteristics shift back to the original state) by annealing the devices at elevated temperature. The trapped electrons are detrapped faster at higher temperatures, causing the neutralized traps to become positively charged, thereby shifting the threshold voltage to its uncompensated value.

The subthreshold swing is not affected by the illumination, as can be seen in Figure 3.12, where the subthreshold swings are equal for all of the characteristics in the dark and under illumination (note the slope of the line labeled (3)). Since the subthreshold swing can be related to the density of states (both bulk states and interface states) as shown in equation (2.5), and since the subthreshold swing is not affected by the illumination, we conclude that the illumination does not affect the density of states of the polymer. Additionally, the field-effect mobility of the accumulated holes is not affected by the illumination, as can be seen from Figure 3.12 (note the slope of the line labeled (2)). This shows that the light has negligible effect on the electronic properties of the polymer film. Also, since the field-effect mobility is unchanged in these measurements, we conclude that the

observed changes in the electrical characteristics are not a result of heating effects in the polymer.

It is important to note that the major effect of illumination on these devices is the generation of excitons, and subsequently free electrons and holes in the polymer. Photons with lower energy can still be absorbed in the polymer (albeit at a much lower rate than the high energy photons), thereby creating excitons, and causing the effects we have described above, but to a much smaller degree as compared to the effects caused by the strongly absorbed photons.

A useful figure merit of a photodetector is the responsivity (*R* in A/W) of the device, which is a measure of the photo-induced signal of the device compared to the input power from the source being detected and has already been defined in equation (3.1). A plot of *R* versus gate bias for different wavelengths of incident illumination and a plot of *R* versus photon energy for different gate biases are shown in Figure 3.14 and Figure 3.15, respectively.

From these figures, we see that the responsivity increases as the device is biased into the strong accumulation regime and illuminated by strongly absorbed illumination. In fact, we observe a responsivity greater than 1A/W for devices used under these conditions, which is comparable to the responsivities of other reported organic photodetectors [14, 15, 24, 25]. For the case of the dependence on the photon energy, shown in Figure 3.15, the higher energy photons, which are strongly absorbed in the polymer, increase the carrier densities in the polymer, as described above. In the strong accumulation regime, the photogenerated holes are accumulated into the channel by the applied gate bias and cause an increase in the drain photocurrent, which in turn causes an increase in the responsivity. In the OFF-state, fewer holes are accumulated into the channel, therefore the drain photocurrent and responsivity are observed to be lower in this operating regime.

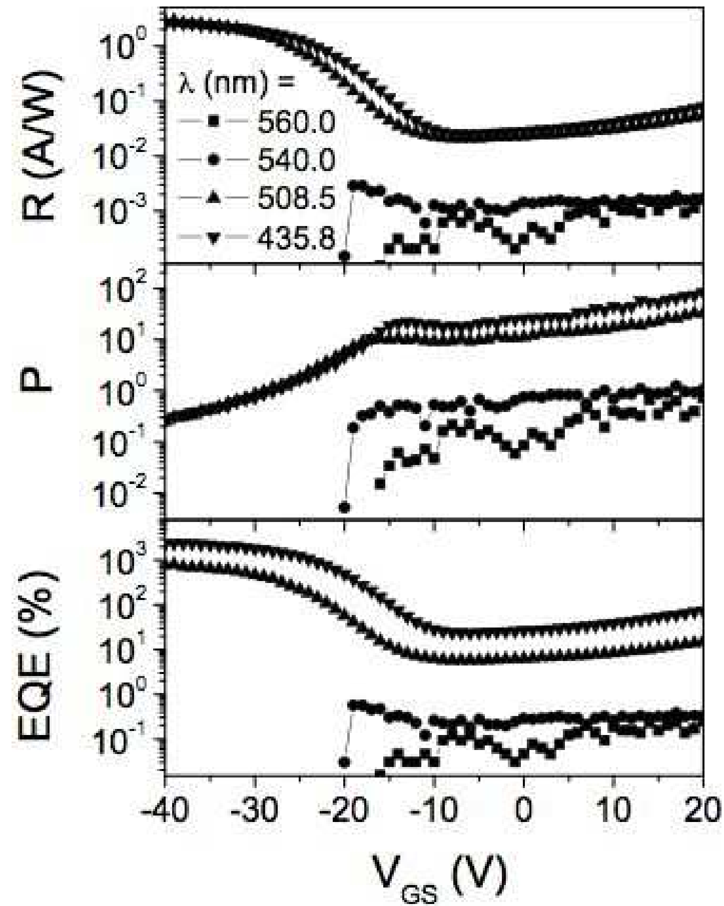

Figure 3.14: Responsivity (R), photosensitivity (P) and external quantum efficiency (EQE) versus V_{GS} of the OFET for illumination at different wavelengths/photon energies with W =56μm, L =6μm, and V_{DS} =-10V.

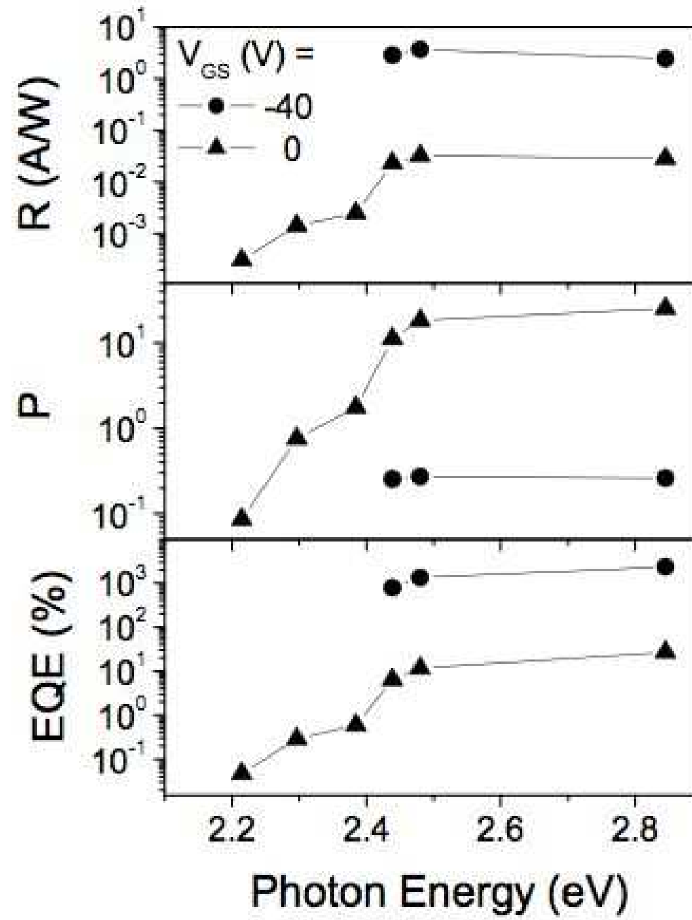

Figure 3.15: Responsivity (R), photosensitivity (P) and external quantum efficiency (EQE) versus the energy of incident photons (measured with a constant optical flux of 5×10^{13} photons/cm^{2}sec) for different biasing regimes of an OFET with W =56μm, L =6μm, and V_{DS} =-10V.

A second useful figure of merit is the photosensitivity (P), or signal (photo-current) to noise (dark-current) ratio, of the device, which was described with the approximation of equation (3.2). For the calculation of P of our devices under monochromatic illumination, we approximate the signal as the drain photocurrent of the illuminated device and approximate the noise from the drain current of the device in the dark. The dependence of the photosensitivity on the applied gate voltage for different incident wavelengths of illumination and on the energy of the incident photons for different gate biases are shown in Figure 3.14 and Figure 3.15, respectively. We observe that the photosensitivity increases as the device is biased from the strong accumulation regime into the OFF-state and illuminated by strongly absorbed illumination. This is the expected result, and can be explained by examining equation (3.2). Since the noise of this detector is related to the dark current, we expect the photosensitivity to be lower in the operating regimes where the dark current is the largest, i.e., in the strong accumulation regime, which is the observed result shown in Figure 3.15. The photosensitivity is relatively independent of the applied gate bias when the device is biased in the OFF-state. For the irradiance values used in this experiment, we find a photosensitivity near 100 for a device biased in the OFF-state.

In order to evaluate the overall efficiency of the photodetector in converting an incident optical signal (photons) into an electrical signal (electrons and holes) and allow the comparison of the performance to other photodetectors, we can determine the external quantum efficiency (EQE) of the photodetector, which can be defined as [18]:

$$EQE = \frac{I_{ph}/q}{P_{inc}/h\nu} \tag{3.8}$$

and corresponds to the ratio of collected charge carriers to the number of incident photons. The dependence of EQE on photon energy for different gate biases and on gate bias for different incident wavelengths is shown in Figure 3.14 and Figure 3.15, respectively. We see from these figures that the EQE increases as the device is biased from the OFF-state

into the strong accumulation regime and is larger for strongly absorbed illumination. In fact, an EQE greater than 100% is found for a device biased in the strong accumulation regime and subjected to strongly absorbed illumination. For the case of strongly absorbed photons, the same flux of photons is converted to a higher density of charge carriers inside the polymer, and the EQE of the device is higher, as we expect. As with the responsivity, the device is expected to accumulate and collect the excess, photogenerated holes more efficiently in the strong accumulation regime.

Several comments should be made with regards to the measurements and calculations performed to find the EQE (as well as the other figures of merit) of these devices. As noted above, under illumination, OFETs exhibit shifts in their electrical characteristics that are believed to be due to the increased carrier concentration and subsequent trapping of charge carriers. These effects, which are similar to the memory effect or persistent photoconductivity which has been observed in organic materials [26–29], are not instant compared to the timescale of the measurement and accumulate as the measurement proceeds. These effects are characterized by an accumulating change in the conductivity of the polymer film as it is exposed to illumination, which persists after the illumination has been removed. The polymer can be annealed, as described above, to facilitate relaxation to the original state, and allow better comparison of subsequent measurements. In order to overcome the cumulative effects described here, which build-up as the measurement progresses, pulsed-gate and pulsed-illumination experiments need to be performed.

Values of responsivity and photosensitivity alone provide limited information about the quality and performance of the photodetector. The sensitivity of the device can be much more completely characterized by the combination of these measures, as well as another useful figure of merit, the noise-equivalent power (NEP in $\mathrm{WHz}^{-0.5}$). The NEP is a measure of the minimum detectable optical power or, in other words, the optical power

required to produce a signal-to-noise ratio of unity. The NEP can be defined as [30]:

$$NEP = \frac{I_N}{R} = \frac{I_N \times P_{inc}}{I_{ph}} \tag{3.9}$$

where I_N is the noise current. For the determination of NEP, we used a calculated value for the noise current of the device that took into consideration the shot (or generation-recombination) noise and Johnson noise, referenced to a bandwidth of 1Hz. We determined the dependence of NEP on applied gate bias for different illumination wavelengths and incident photon energy for different gate biases. The NEP remains flat, with a value of approximately 10^{-14}WHz$^{-0.5}$, as the device is biased from the strong accumulation regime into the OFF-state and when illuminated by light which is strongly absorbed. Since the noise current is related to the drain current of the device, it is expected to be larger in the strong accumulation regime than in the OFF-state. From Figure 3.14, we see that the responsivity of the devices shows a similar variation. The result is an NEP that has little variation on the applied gate bias. The NEP is reduced for higher energy photons, since the noise current remains the same but the responsivity is increased for the higher energy photons, as described above.

In general, we humans do not like to connect a decreasing number to an increase in device performance. In contrast, we would rather connect increased performance of a device to an increasing number, therefore, we can define the specific detectivity (D^*) for these devices as [30]:

$$D^* = \frac{\sqrt{A}\sqrt{\Delta f}}{NEP} \tag{3.10}$$

where A is the effective area of the device and Δf is the referenced bandwidth (=1Hz). For an incident wavelength of 500nm, we find the specific detectivity of a device (in both the OFF-state and ON-state) to be approximately $2{\times}10^{11}$ cmHz$^{0.5}$W^{-1}.

Dependence on irradiance

To investigate the effects of monochromatic illumination further, we again measured the transfer characteristics of an OFET under illumination at a wavelength of 460nm, at different levels of irradiance. This type of experiment allowed us to explore the dependence on the number of absorbed photons, since at larger irradiance levels, it is expected that more photons are absorbed in the polymer film. These results are shown in Figure 3.16, where we plot the threshold-voltage normalized, linear regime transfer characteristics. We chose to use 460nm because it lies in the absorption peak of F8T2, and allowed a larger range of incident, and therefore absorbed, optical flux. We can see, from Figure 3.16, that the effects of the illumination increase (i.e., the OFF-state drain current increases and the threshold voltage is reduced) as the irradiance is increased, similar to the effects of broadband illumination [23]. This is the expected effect, since as the irradiance is increased, the polymer film is exposed to a higher flux of photons, thereby generating more charge carriers. The increased number of electrons causes a greater reduction of the threshold voltage, by the neutralization of the positively charged traps, while the increased number of holes causes the channel to have a higher conductivity. And, again, we see that the field-effect mobility and subthreshold swing are not affected by the illumination and have no dependence on the incident irradiance as can be deduced from Figure 3.16 (note the slopes of the lines labeled (2) and (3)). The dependence of the change in threshold voltage, ON-state and OFF-state drain currents, and number of absorbed photons on the incident irradiance are shown in Figure 3.17. Note that each parameter plotted in Figure 3.17 has a linear relationship with the number of incident photons and, assuming that the absorption coefficient is not strongly dependent on the incident photon flux in the range we use here, this is evidence that the observed effects described above are related to the number of absorbed photons.

In Figure 3.18, we plot the responsivity (found using equation (3.1)) and photosen-

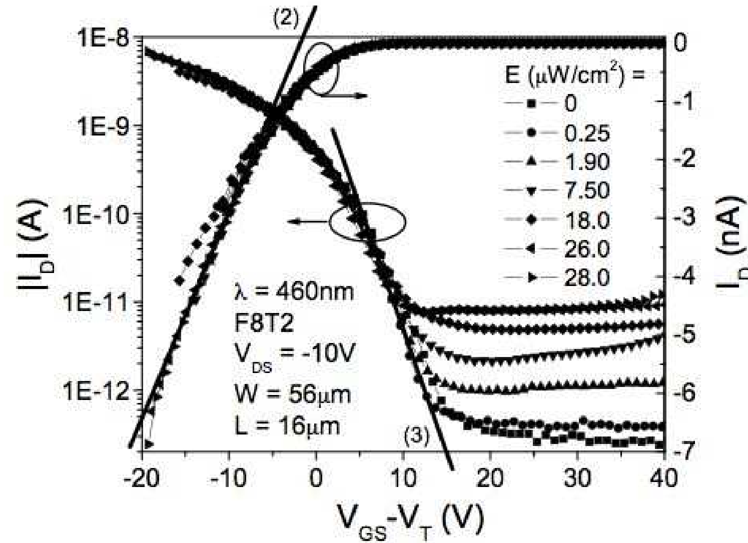

Figure 3.16: Threshold voltage-normalized transfer characteristics of OFET illuminated at a wavelength of 460nm (corresponding to maximum absorption of the F8T2 polymer film) for different irradiance levels. The straight lines are fits using equations (2.2) and (2.4).

sitivity (found using equation (3.2)) of the device as a function of applied gate bias for various irradiance levels. With the caveats stated above, regarding the memory effect of illuminated organic materials, we see that the responsivity reaches values greater than 1A/W in the strong accumulation regime and is reduced as the device is biased into the OFF-state. We can also see that the responsivity is highest for the lower irradiance levels. It is possible that this effect is due to the saturation of the drain photocurrent in the strong accumulation regime, even at low incident irradiance levels. Therefore, in the strong accumulation regime, the drain current is expected to be similar for each irradiance level, and the calculated responsivity is expected to be governed by the value of the irradiance. The photosensitivity increases as the device is biased from the strong accumulation regime into the OFF-state, is largest for the highest irradiance level, and is relatively independent of the applied gate bias in the OFF-state, corresponding to the explanation we have presented

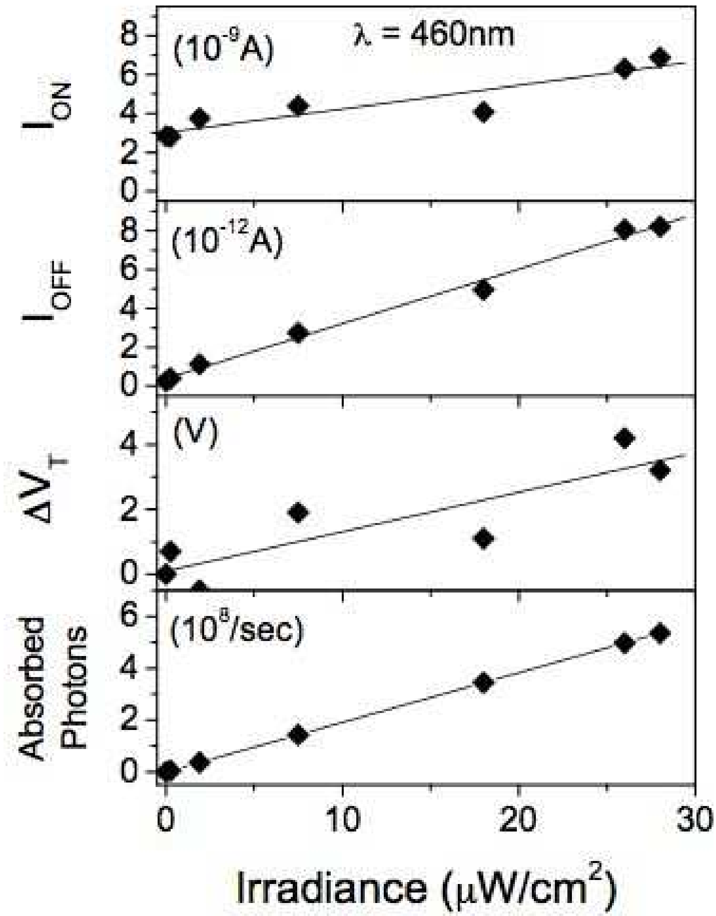

Figure 3.17: Dependence of ON-state drain current, OFF-state drain current and the change in threshold voltage on irradiance at a wavelength of 460nm. Also shown is the number of photons absorbed in the channel region of the device as a function of incident irradiance.

above.

Since the responsivity (R) is dependent on the incident power (P_{inc}), we expect and observe that the measured responsivity for the case of strongly absorbed illumination (i.e. monochromatic light of the proper energy) is much larger than the case of a device illuminated from a broadband source in which the majority of the illumination is not absorbed and therefore does not contribute to the photocurrent, as shown in Figures 3.8 and 3.18. In contrast, the photosensitivity (P) is not directly normalized by incident optical power, therefore, as shown in Figures 3.8 and 3.18, we observe that a much larger incident power of broadband illumination is necessary to produce similar photosensitivities as that measured for a much lower incident power of monochromatic illumination.

In Figure 3.18 we also plot the EQE (found using equation (3.8)) of the device as a function of applied gate bias for various irradiance levels. From this figure, we see that the EQE decreases as the device is biased from the strong accumulation regime to the OFF-state. At larger gate biases, more of the photogenerated holes are accumulated and contribute to the drain photocurrent, therefore the efficiency of the device is higher in the strong accumulation regime as compared to the OFF-state. We see from Figure 3.18 that as the irradiance is increased, the EQE decreases. For the case of these measurements, we are using a constant illumination wavelength, and therefore a constant photon energy. With the assumption that the absorption coefficient is not dependent on the incident irradiance, we see from Figure 3.17 that the number of absorbed photons retains a linear relationship with the incident irradiance. Therefore, we speculate that at the higher irradiance values, phenomena such as exciton-exciton annihilation and electron-hole recombination occur, reducing the number of photogenerated carriers that can contribute to the drain photocurrent. This, in turn, reduces the external quantum efficiency. We observed a nearly linear increase of NEP with irradiance from approximately 3×10^{-15} to 1×10^{-14} $\mathrm{WHz}^{-0.5}$ over

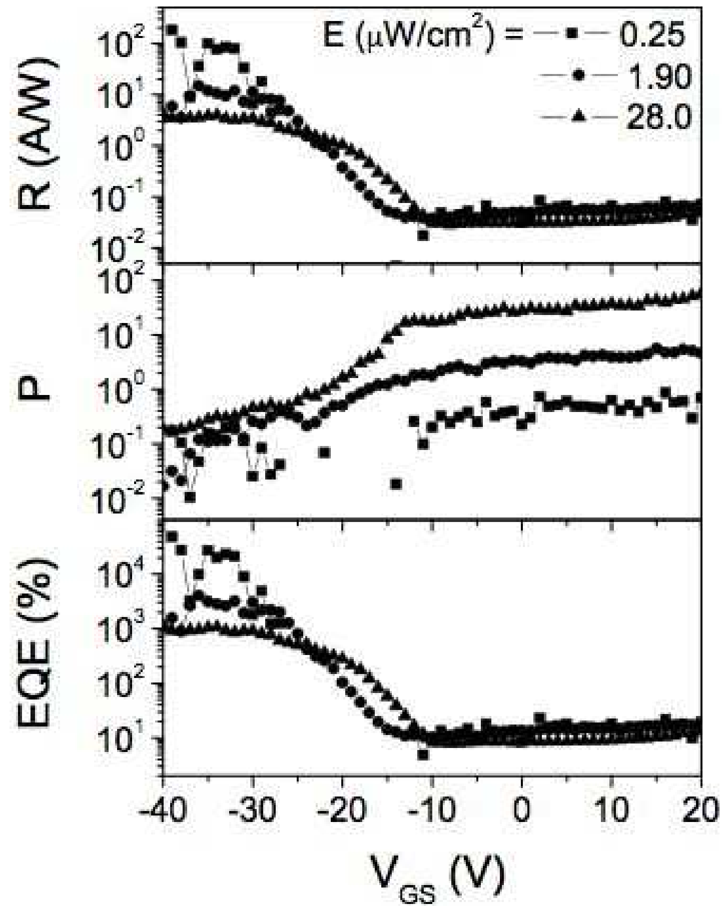

Figure 3.18: Responsivity (R), photosensitivity (P) and external quantum efficiency (EQE) of an OFET versus V_{GS} for various irradiance levels at a wavelength of 460nm with W =56μm, L =6μm, and V_{DS} =-10V.

the range of irradiance used here, at a wavelength of 460nm. Processes such as exciton annihilation or carrier recombination effectively reduce the signal that is detected by the device (i.e., the drain photocurrent is smaller than if no recombination occurs). Since the NEP is a measure of the smallest detectable optical power, if the signal is reduced in the device due to these non-idealities, the NEP is expected to increase.

Another measure, which is related to the photosensitivity, is the ratio of total drain current under illumination to drain current in the dark, which is referred to as the photoresponse and has been defined in equation (3.3). $R_{L/D}$ is a useful paramater for extracting more physical parameters from the illuminated versus dark electrical characteristics of the OFET. The dependence of $R_{L/D}$ on gate bias and incident photon energy is similar to that of the photosensitivity (i.e., increases from strong accumulation to OFF-state and for strongly absorbed illumination and is independent of the applied gate bias in the OFF-state). $R_{L/D}$ increases from nearly unity in the strong accumulation regime to approximately 75 in the OFF-state (depending on the irradiance level). In the OFF-state, this ratio is relatively independent of the gate bias. In the strong accumulation regime, the density of accumulated carriers is due mainly to the applied gate bias, as opposed to the illumination (for the range of irradiance values use here). In the OFF-state, the photogenerated charge carriers are the major contribution to the free carrier density in the channel, and $R_{L/D}$ is strongly dependent on the incident irradiance. Again, we note that the ratio exhibits a power law dependence on the irradiance, as in equation (3.4). This follows from a model, which has been developed for the photo-field effect in amorphous semiconductor-based TFTs [11, 12, 20]. The major assumptions in this model are that the total density of states around mid-gap are constant, there is a symmetric overlap of donor and acceptor states around mid-gap, and that the field-effect is governed by the bulk states and not by the interface states. It is also assumed that the Fermi level splits into quasi-Fermi levels under

illumination, which must be the case for spatially dependent carrier generation, since the carriers need to diffuse and redistribute. These assumptions do not seem unreasonable for organic materials, therefore, we assume this model to be valid for OFETs, and the results are shown in Figure 3.19.

Similar to the case for broadband illumination, the dependence of γ on V_{GS} can be de-

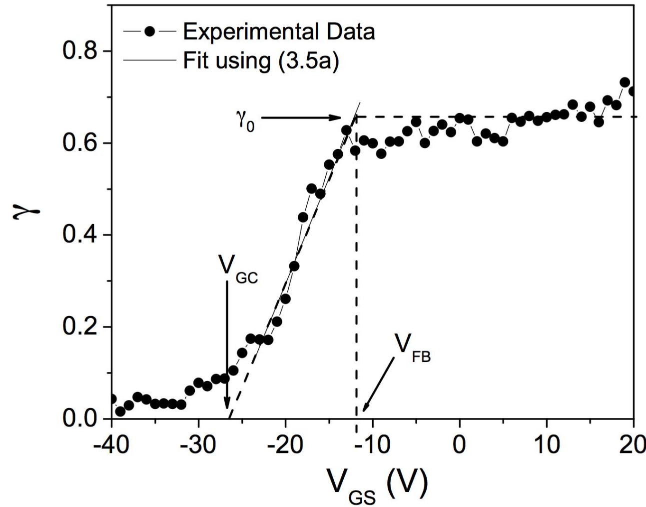

Figure 3.19: γ-factor of the OFET versus V_{GS} for various irradiance levels at a wavelength of 460nm.

scribed using equations (3.5a), (3.5b), (3.6) and (3.7). In Figure 3.19, we see that we can fit the data in the region $V_{FB} < |V_{GS}| < V_{GC}$ using equation (3.5a) with V_{GC} equal to approximately -27V. This gives a β value of approximately 9.4×10^{5}. If we assume a value of 10^{18}cm^{-3}eV^{-1} for $2N_f$ (estimated from equation (2.5) with $N_{SS} = 0$), we find that L is equal to 1.1×10^{21}cm^{-3}eV^{-2} from equation (3.7). Note that this simple calculation assumes that $N_{SS} = 0$. If $N_{SS} > 0$, then both N_f and L will be reduced to maintain the constant value of β. In the case of our devices, γ_0 from experimental data is approximately 0.6, while the fit using equation (3.5b) gives a γ_0 value of approximately 0.7.

It is possible to determine the flat-band voltage (V_{FB}) of the OFET from Figure 3.19

using a method similar to that of Schropp, et al [11, 12]. The density of accumulated holes in the channel does not increase for applied gate biases from the flat-band voltage to more positive voltages and the source and drain electrodes block electrons coming from the conduction band (LUMO). Therefore the ratio of drain current under illumination over drain current in the dark is constant for positive applied gate biases. As the gate is biased from the flat-band voltage to more negative biases, the logarithm of the current ratio is approximately proportional to $V_{GS} - V_{FB}$. As did Schropp, et al, we assume that there is no shift in the flat-band voltage under illumination. We extract the flat-band voltage from the crossing point of equations (3.5a) and (3.5b), and we find the V_{FB} of this device to be equal to -12V. As stated above, this negative value of V_{FB} is evidence of an effective charge (i.e., trapped charge) within the channel and contributes to the relatively large value of the threshold voltage of these OFETs.

3.3 Conclusion

We have studied the electrical performance of F8T2-based OFETs under monochromatic illumination, and have examined their performance as photodetectors. For these devices, the major effect of the absorbed light is a significant increase in the OFF-state drain current and a reduction of the threshold voltage by several volts, depending on the illumination conditions. The field-effect mobility and subthreshold swing are not affected by the illumination. These effects are explained by the photogeneration of excitons in the polymer, which diffuse and dissociate into free charge carriers. The effects on the OFF-state drain current and threshold voltage are dependent on the wavelength and irradiance of the incident illumination. Photons with energy below the optical-gap of the polymer are weakly absorbed, generating few excitons, and therefore have little effect on the electrical characteristics of the OFET. Whereas, higher energy photons are more strongly absorbed

in the polymer, generating a higher density of excitons, and causing larger changes in the electrical characteristics. This explanation is confirmed by examining the effects of the level of irradiance at a single photon energy on the electrical characteristics of the OFETs.

We have also presented the relevant photodetector figures of merit, such as the responsivity (R), photosensitivity (P), external quantum efficiency (EQE), noise-equivalent power (NEP) and specific detectivity of these devices, with typical values greater than 1A/W, 100, 100%, less than 10^{-14}WHz$^{-0.5}$, and approximately 2×10^{11} cmHz$^{0.5}$W^{-1} respectively, depending on the illumination and bias conditions. The dependence of these parameters on photon energy, irradiance, and applied gate bias have also been presented and explained. From a system point-of-view, it is generally desirable to have a detector with the highest sensitivity. The responsivity and photosensitivity indicate the sensitivity of the device, however, they do not take the noise into account. Therefore, to be more specific about the performance of the detector, the key figure of merit is usually quoted as the detectivity or specific detectivity, which we have described and has been related to the noise equivalent power above. For comparison, we note that, in general, the inorganic photodetector counterparts (i.e., InAs- and PbS-based photodiodes) provide responsivity greater than 1A/W, external quantum efficiency of 100%, and specific detectivity greater than 2×10^{11} cmHz$^{0.5}$W^{-1} in the visible range of wavelengths.

We propose the use of a model developed for amorphous semiconductor-based TFTs under illumination to aid in the description of the effects of illumination on the OFETs. Our results agree well with this proposed model. Using this method, we find a flat-band voltage (V_{FB}) of approximately -12V for these F8T2-based OFETs.

References

[1] P. J. Reucroft, “Photocarrier generation mechanisms in polymers,” in *Photoconductivity in Polymers: An Interdisciplinary Approach*, A. V. Patsis and D. A. Seanor, Eds. Westport, CT: Technomic Publishing Co., Inc., 1976.

[2] G. Leising, S. Tasch, and W. Graupner, “Fundamentals of electroluminescence in paraphenylene-type conjugated polymers and oligomers,” in *Handbook of Conducting Polymers*, T. A. Scotheim, Ed. New York: Dekker, 1998.

[3] N. Kirova and S. Brazovskii, “Optical and electrooptical absorption in conducting polymers,” *Thin Sol. Films*, vol. 403-404, pp. 419–424, 2002.

[4] P. Dyreklev, O. Inganas, and J. P. adn H. Stubb, “Photoluminescence quenching in a polymer thin-film field-effect luministor,” *J. Appl. Phys.*, vol. 71, pp. 2816–2820, 1992.

[5] C. Silva, A. S. Dhoot, D. M. Russell, M. A. Stevens, A. C. Arias, J. D. MacKenzie, N. C. Greenham, R. H. Friend, S. Setayesh, and K. Müllen, “Efficient exciton dissociation via two-step photoexcitation in polymeric semiconductors,” *Phys. Rev. B*, vol. 64, p. 125211, 2001.

[6] A. C. Morteani, R. H. Friend, and C. Silva, “Exciton trapping at heterojunctions in polymer blends,” *J. Chem. Phys.*, vol. 122, p. 244906, 2005.

[7] M. A. Stevens, C. Silva, D. M. Russell, and R. H. Friend, “Exciton dissociation mechanisms in the polymeric semiconductors poly(9,9-dioctylfluorene) and poly(9,9-dioctylfluorene-co-benzothiadiazole),” *Phys. Rev. B*, vol. 63, p. 165213, 2001.

[8] A. R. Brown, C. P. Jarrett, D. M. deLeeuw, and M. Matters, “Field-effect transistors made from solution-processed organic semiconductors,” *Synth. Met.*, vol. 88, pp. 37–55, 1997.

[9] M. C. J. M. Vissenberg and M. Matters, “Theory of the field-effect mobility in amorphous organic transistors,” *Phil. Rev. B*, vol. 57, pp. 12 964–12 967, 1988.

[10] G. Horowitz, R. Hajlaoui, R. Bourguiga, and M. Hajlaoui, “Theory of the organic field-effect transistor,” *Synth. Met.*, vol. 101, pp. 401–404, 1999.

[11] R. E. I. Schropp, A. O. Harm, and J. F. Verwey, “A refined theoretical analysis of photofield-effect measurements in a-Si:H thin-film transistors,” *Phil. Mag. B*, vol. 53, pp. 431–444, 1986.

[12] A. O. Harm, R. E. I. Schropp, and J. F. Verwey, “The photofield effect in a-Si:H thin-film MOS transistors: Theory and measurement,” *Phil. Mag. B*, vol. 52, pp. 59–70, 1985.

[13] C. van Berkel and M. J. Powell, “Photo-field effect in a-Si:H thin-film transistors,” *J. Appl. Phys.*, vol. 60, pp. 1521–1527, 1986.

[14] J. Gao, F. Hide, and H. Wang, "Efficient photodetectors and photovoltaic cells from composites of fullerenes and conjugated polymers: photoinduced electron transfer," *Synth. Met.*, vol. 84, pp. 979–980, 1997.

[15] G. Yu, Y. Cao, J. Wang, J. McElvain, and A. J. Heeger, "High sensitivity polymer photosensors for image sensing applications," *Synth. Met.*, vol. 102, pp. 904–907, 1999.

[16] M. C. Hamilton, S. Martin, and J. Kanicki, "Effect of monochromatic illumination on organic polymer thin-film transistors," *Proc. of the IDRC 2003*, pp. 14–17, 2003.

[17] M. C. Hamilton and J. Kanicki, "Organic polymer thin-film transistor photosensors," 2004, to be published.

[18] P. Bhattacharya, *Semiconductor Optoelectronic Devices*, 2nd ed. Upper Saddle River, NJ: Prentice Hall, 1997.

[19] J. D. Gallezot, S. Martin, and J. Kanicki, "Photosensitivity of a-Si:H TFTs," *Proc. of the IDRC 2001*, pp. 407–410, 2001.

[20] G. Fortunato, L. Mariucci, and C. Reita, "Physics of metal/insulator/amorphous semiconductor structures," in *Amorphous & Microcrystalline Semiconductor Devices - Materials and Device Physics*, J. Kanicki, Ed. Boston, MA: Artech House, Inc., 1992.

[21] A. Salleo and R. A. Street, "Light-induced bias stress reversal in polyfluorene thin-film transistors," *J. Appl. Phys.*, vol. 94, pp. 471–479, 2003.

[22] R. A. Street, A. Salleo, and M. L. Chabinyc, "Bipolaron mechanism for bias-stress effects in polymer transistors," *Phil. Rev. B*, vol. 68, p. 085316, 2003.

[23] M. C. Hamilton, S. Martin, and J. Kanicki, "Thin-film organic polymer phototransistors," *IEEE Trans. Electron Devices*, vol. 51, pp. 877-885, 2004.

[24] K. S. Narayan and N. Kumar, "Light responsive polymer field-effect transistor," *Appl. Phys. Lett.*, vol. 79, pp. 1891–1893, 2001.

[25] K. S. Narayan and T. B. Singh, "Nanocrystalline titanium dioxide-dispersed semiconducting polymer photodetectors," *Appl. Phys. Lett.*, vol. 74, pp. 3456–3458, 1999.

[26] S. Dutta and K. S. Narayan, "Nonexponential relaxation of photoinduced conductance in organic field effect transistors," *Phys. Rev. B*, vol. 68, p. 125208, 2003.

[27] A. Fujii, M. Yoneyama, K. Ishihara, S. Maeda, and T. Murayama, "Memory effect of an organic photoconductor and its application to a neuron model," *Appl. Phys. Lett.*, vol. 62, pp. 648–650, 1993.

[28] M. Hiramoto, T. Imahigashi, and M. Yokoyama, "Photocurrent multiplication in organic pigment films," *Appl. Phys. Lett.*, vol. 64, pp. 187–189, 1994.

[29] A. Thander and B. Mallik, "Observation of persistent photoconductivity at room temperature in ferrocene-doped poly(methyl methacrylate) thin films containing chloroform molecules," *Solid State Commun.*, vol. 121, pp. 159–164, 2002.

[30] E. L. Dereniak and D. G. Crowe, *Optical Radiation Detectors*, 1st ed. New York: John Wiley & Sons, 1984.

CHAPTER 4

HYSTERESIS IN THE ELECTRICAL CHARACTERISTICS OF PF-BASED OFETS

In this section, we describe a study of measurement-induced shifts (hysteresis) in the transfer characteristics and output characteristics of organic field-effect transistors. We believe that this hysteresis is related to the charge carrier trapping in the organic polymer, at or near the semiconductor to gate insulator interface, and is triggered by the accumulation of a large density of carriers in the channel of the device due to the applied gate bias. We show that the hysteresis width and the corresponding hysteresis charge depend strongly on the maximum applied gate-to-source bias, but do not exhibit a strong dependence on the measurement time nor the applied drain-to-source voltage. We have also investigated the dependence of the hysteresis width on temperature and incident illumination and these results provide further insight into this phenomenon.

4.1 Hysteresis in the electrical characteristics of OFETs

Hysteresis in the electrical transfer characteristics of organic devices, especially transistors, is a commonly observed effect that has been either directly or indirectly reported by several research groups. Scheinert et al proposed that, in the devices with inorganic insulators they studied, the major cause of the hysteresis appeared to be movement of

mobile ions (i.e., intentionally or unintentionally doped species) in the polymer semiconductor layer that results in a shift of the flat-band voltage [1, 2]. Klauk et al investigated the use of a pentacene-based organic transistor with an organic insulator [3]. This device structure provided enhanced mobility, however, it also exhibited a significant amount of hysteresis, which has been attributed to the accumulation of a space charge, possibly in the form of mobile ions, at the interface between the dielectric insulator and the organic semiconductor. Uemura et al provided a solution to this problem by introducing an insulator treatment based on a clay mineral that adsorbs the ions, thereby reducing the observed hysteresis effects [4].

More recently, charge trapping in the organic semiconductor layer has been introduced as the explanation for the observed hysteresis in the transfer characteristics of pentacene-based OFETs with untreated inorganic insulators (such as SiO_2, Al_2O_3 and $LaAlO_3$) [5, 6] and with an organic insulator (polymer electrolyte) [7]. Recent results for the case of polymer semiconductors showed that the surface modification of an inorganic insulator (SiO_2) with octadecyltrichlorosilane (OTS) could reduce the hysteresis effects for devices based on rr-P3HT, but, for the case of short channel devices, hysteresis was still observed for devices based on PQT-12 [8, 9].

Additionally, hysteresis effects in the current-voltage characteristics of various two- and three-terminal device structures have been used to demonstrate devices for memory applications [10–16]. In general, the three terminal memory devices utilize a polarizable or ferroelectric gate insulator to provide the bistability.

In this section, we describe a study of the hysteresis in the electrical characteristics as it pertains to a defined-gate device based on a polyfluorene derivative active layer and the effects of the applied gate bias, measurement temperature and incident illumination.

4.1.1 Experimental results and analysis

Dependence on gate and drain bias

The F8T2-based OFET structures with an a-SiN:H insulator exhibit significant hysteresis in their transfer characteristics. We have investigated various circumstances that affect the observed hysteresis. We measured the transfer characteristics of our devices by cycling the gate-to-source voltage (V_{GS}) and thereby taking the device from the OFF-state, to the ON-state for various maximum V_{GS} (V_{GSmax}), and back to the OFF-state as shown in Figure 4.1. We have observed an apparent shift, or hysteresis, in the transfer characteristics from higher to lower V_{GS} values. Note that, contrary to the above statement, the device was not annealed between measurements, which explains why there is an overall shift in the characteristics (i.e., ideally, for devices annealed between measurements, there should be minimal residual threshold voltage shift and the OFF to SA portions of the curves would be more closely in line, while the SA to OFF portion is expected to be shifted depending on the maximum applied gate bias). To investigate the cause of the hysteresis in the transfer characteristics, we made similar measurements but varied the gate-to-source voltage step and hence the total measurement time, since the time per step is constant, as shown in Figure 4.2(a). From these results, we observed that the hysteresis width does not appear to depend on the measurement time and therefore should not be attributed to a persistent type of device aging caused by this short range of measurement times. In light of recent results presented by Salleo et al [18], it seems reasonable to suggest that the hysteresis is caused by charge carriers (i.e., holes) that exist in shallow, localized states within the channel region and are relatively easily removed from the channel once the gate bias is removed. We note the difference between this mechanism and the formation of and trapping of holes into deep localized states that would correspond to a persistent shift, or device aging. These effects are described in more detail below.

We have observed different values of the shift for samples based on different poly-

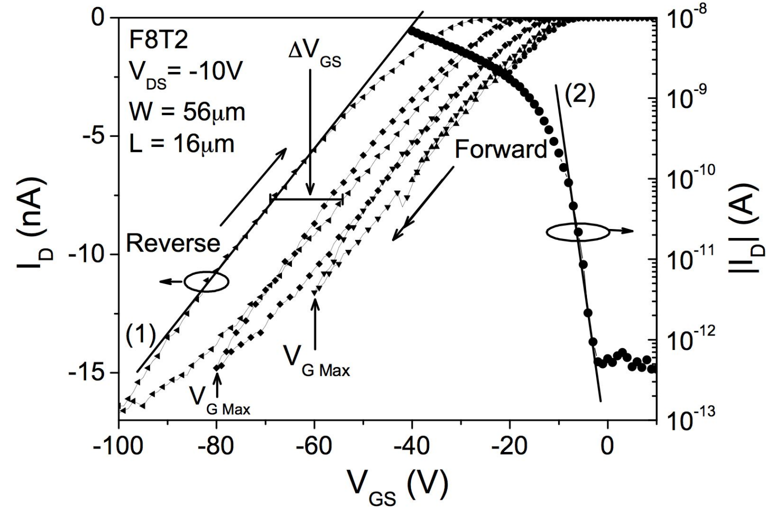

Figure 4.1: Transfer characteristics (measured from OFF to Strong Accumulation (SA) to OFF) of device measured to different maximum V_{GS} (V_{GMax}). Also shown for reference is transfer characteristics of OFET on semilog scale. Lines are fits to equations (1) and (2). For this device, L = 16μm, W = 56μm and the source/drain-gate overlap is approximately 5μm.

mers, but using the same device size and structure. These results lead us to believe that the shift is due to charge trapping in the organic polymer film, most likely in the channel region near the interface with the gate insulator (a-SiN$_x$:H). As a qualitative measure of the amount of hysteresis, we define the density of trapped charge that can account for the shift of the transfer characteristic, or hysteresis charge, as:

$$Q_{hyst} = C_{ins} \times \Delta V_{GS} \tag{4.1}$$

where C_{ins} is the gate insulator capacitance (F/cm^2) and ΔV_{GS} is the hysteresis width (V) for a constant value of I_D. The value of I_D was selected to ensure that the different values of Q_{hyst} were extracted under similar OFET operating conditions (i.e., at some point in the strong accumulation regime). Q_{hyst} does not necessarily have a specific physical meaning, though it is a measure of the threshold voltage shift and this is described in

more detail below. We can clearly see, from Figures 4.1 that Q_{hyst} depends strongly on the maximum gate voltage applied during the measurement of the device. Therefore, when the gate voltage is swept in the forward direction (OFF-state to ON-state, the first half of our measurement), the charge accumulation/trapping and accompanying transfer characteristic shifts occur gradually as the measurement progresses, i.e., as the magnitude of the gate-to-source voltage is increased. Whereas, if the gate voltage is swept in the reverse direction (ON-state to OFF-state, the second half of our measurement), the majority of charge accumulation/trapping and the corresponding shift in the transfer characteristics occur immediately when the measurement begins (i.e., at the point of maximum V_{GS}). One possible explanation for this phenomenon is that the accumulated charge, which is induced by and depends on the applied gate bias, is accumulated into localized states (i.e., traps) in the organic semiconductor at or near the interface between the active organic semiconductor layer and the gate insulator layer, thereby leading to a shift in the threshold voltage of the transistor which is evident in the transfer characteristics ($I_D - V_{GS}$) of the device. To further investigate the hysteresis, we measured the OFF-ON-OFF transfer characteristics in a back-to-back manner as shown in Figure 4.2(b). In this measurement, we observed that the second forward characteristic (OFF to ON) is not as shifted as the first reverse characteristic (ON to OFF). This evidence supports the explanation of the cause of the hysteresis as shallow, easily reversible, localization of charge carriers in the band-tail states of the organic semiconductor, at or near the interface between the organic semiconductor and gate insulator layers and not persistent device aging, since the majority of the shift is immediately reversible (i.e., the shift does not persist from one characteristic to the next).

We have also measured the output characteristics ($I_D - V_{DS}$) of our devices by cycling the drain-to-source voltage (V_{DS}) from $V_{DS} = 0$V, to $V_{DS} = V_{GS}$ (saturation regime), and

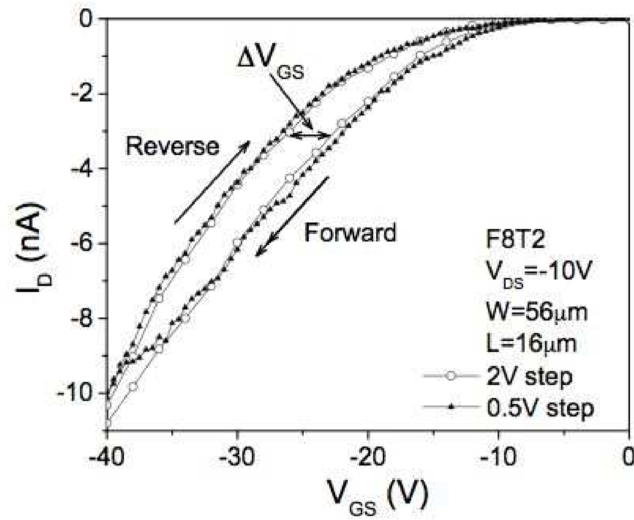

(a)

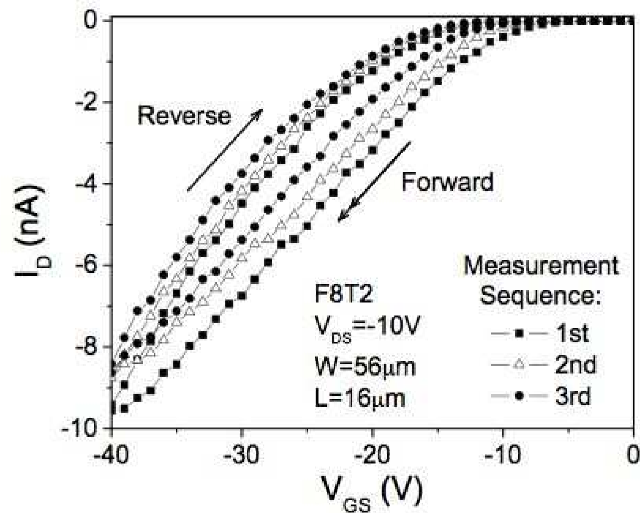

(b)

Figure 4.2: (a) Transfer characteristics (from OFF to ON to OFF) for different total measurement time (i.e., varying step time, with same number of steps). (b) Transfer characteristics (from OFF to ON to OFF) measured back-to-back, with no time delay between measurements.

back to $V_{DS} = 0$V. The results for measuring to a single maximum V_{DS} for several values of V_{GS} are shown in Figure 4.3(a). Additionally, Figure 4.3(b) shows the results for measuring to a different maximum value of V_{DS} for a single value of V_{GS}. From these figures, we can see that there is no appreciable hysteresis in the output characteristics as the drain to source voltage is swept in the reverse and then forward directions while the gate to source voltage is held constant. This does not contradict the ideas stated above concerning the transfer characteristics. The output characteristics are measured at a constant gate voltage; therefore all of the charge trapping and any accompanying threshold voltage shift occur immediately when the measurement begins and the resulting curve does not depend on the direction in which it is measured. More importantly, a threshold voltage shift would not be seen as a hysteresis in the output characteristic ($I_D - V_{DS}$) curves, which would correspond to a shift in V_{DS}, not in V_{GS}. It should be noted that the slight shift in the output characteristic (for V_{DS} from 0 to high V to 0) may be attributed to measurement-induced device aging since the device is held at a relatively high V_{GS} for an extended period of time, which may allow a significant amount of irreversible (i.e., persistent) charge trapping to take place. These results show that further investigation of the hysteresis phenomenon should focus on the change of the drain current with gate bias (i.e., transfer characteristics) rather than the change of the drain current with drain bias (i.e., output characteristics).

The hysteresis charge as a function of maximum applied gate bias, taken from Figure 4.1 using equation 4.1 is presented in Figure 4.4. As noted above, the hysteresis charge is strongly dependent on the maximum applied gate bias as shown here. A best fit of the experimental data shown in this figure is of the form:

$$Q_{hyst} = Q_o + A \cdot e^{b \cdot V_{GSmax}} = -1.8 \times 10^{-8} + 1.4 \times 10^{-8} e^{(0.02 \cdot V_{GSmax})} \tag{4.2}$$

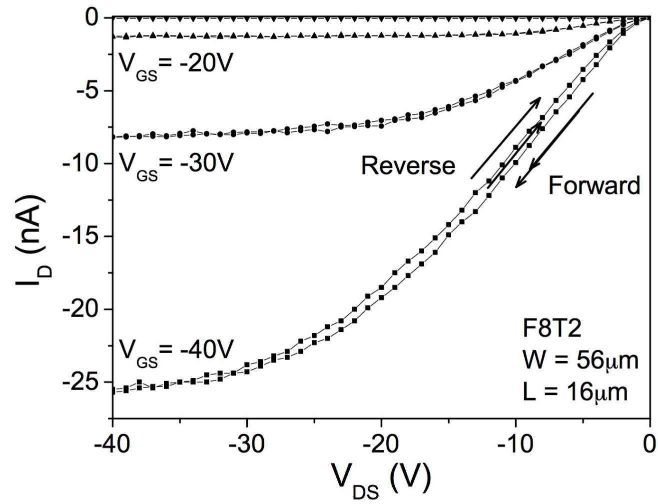

(a)

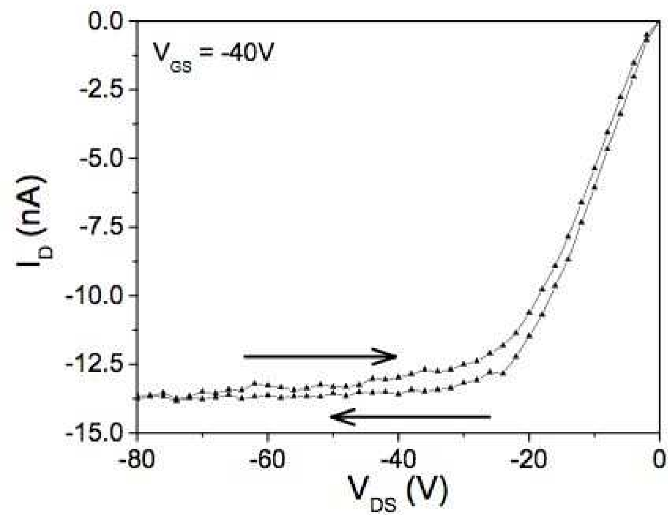

(b)

Figure 4.3: (a) Output characteristics (V_{DS} = 0V to V_{DS} = -highV to V_{DS} = 0V) for same $V_{DS\,max}$ and different V_{GS}. (b) Output characteristics (V_{DS} = 0V to V_{DS} = -highV to V_{DS} = 0V) to a larger $V_{DS\,max}$.

However, a similar, but simpler exponential form, such as:

$$Q_{hyst} = A \cdot e^{b \cdot V_{GSmax}} = 4.9 \times 10^{-9} e^{(0.03 \cdot V_{GSmax})} \tag{4.3}$$

can provide a similar fit of the experimental data and is also shown in Figure 4.4 for reference. From these results, we observe that the hysteresis charge exhibits an exponential dependence on the applied gate bias.

To continue with this study, we have characterized the effects of temperature and illu-

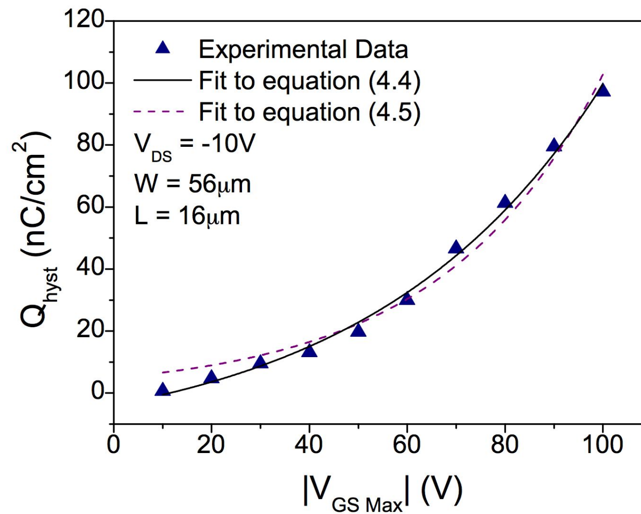

Figure 4.4: Q_{hyst} as a function of V_{GSmax}, taken from the data of Figure 4.1, with two different exponential fits.

mination (both irradiance and wavelength) on the hysteresis in the linear regime transfer characteristics of a device. The results are presented below.

4.1.2 Dependence on temperature

We have previously described the effects of temperature on the electrical performance of the F8T2-based OFETs used in this study [19]. In Figure 4.5(a), we present results obtained for a device hysteresis characteristics measured over a range of temperatures. From this figure, we can see that the most notable effect of increasing the temperature is

an increase in the ON-state drain current, due to the thermal activation of the field-effect mobility of the device with an activation energy of approximately 0.2eV. The OFF-state drain current was observed to be thermally activated with a similar activation energy, as well and it is important to note that the threshold voltage of these devcies exhibit little dependence on the temperature. Additionally, while the ON-state drain current increases with temperature, the hysteresis charge shows almost no thermal dependence as shown in Figure 4.5(c). Since it is apparent that the major effect of temperature is on the transport of carriers within the channel and not necessarily on the level of accumulation of carriers in the channel, these results are further evidence that the amount of hysteresis is mostly dependent on the level of charge carrier accumulation.

4.1.3 Dependence on illumination

Earlier, we described the effects of broadband and monochromatic illumination on the electrical performance of OFETs [20, 21]. In Figures 4.6(a) and 4.8(a), we present the transfer characteristics, exhibiting hysteresis, for devices measured under various wavelengths of illumination and various levels of irradiance of strongly absorbed illumination, respectively. From these plots, we see that the hysteresis charge exhibits an appreciable dependence on both the wavelength and the irradiance of the incident illumination.

Since we expect strongly absorbed light to generate more charge carriers in the channel than weakly absorbed illumination, and since the hysteresis charge is dependent on the level of charge density in the channel, we expect (and observe) that the hysteresis charge follows the absorption coefficient curve as shown in Figure 4.6(b). Additionally, as shown in Figure 4.7(a), we see that the hysteresis exhibits a linear dependence on the absorption coefficient. Furthermore, we can estimate the number of absorbed photons from:

$$N_{abs} \approx N_{inc}\left(1 - e^{-\alpha \cdot d}\right) \cdot A \cdot t \tag{4.4}$$

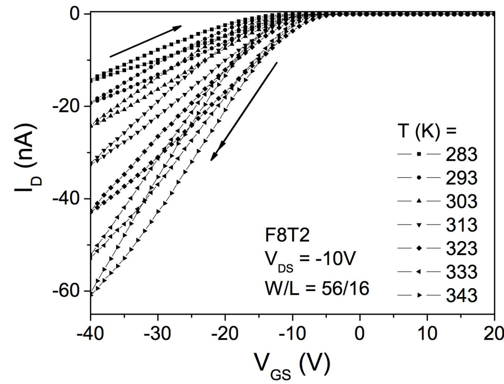

(a)

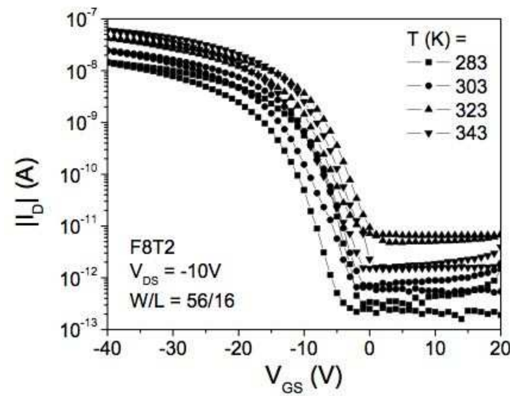

(b)

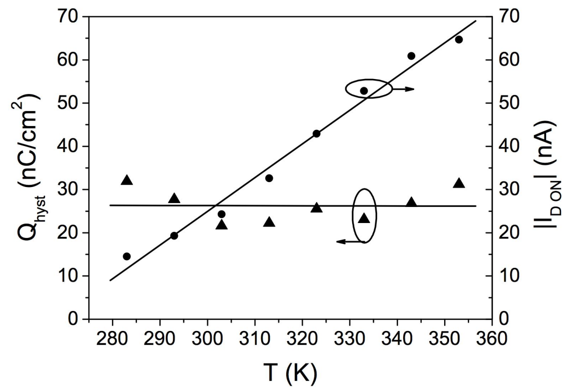

(c)

Figure 4.5: Transfer characteristics (from OFF to ON to OFF) for device measured at different temperatures on (a) linear and (b) semilog scales. (c) Q_{hyst} (as defined in the text) and $|I_{ON}|$ as functions of the measurement temperature for the data presented in Figure 4.5(a).

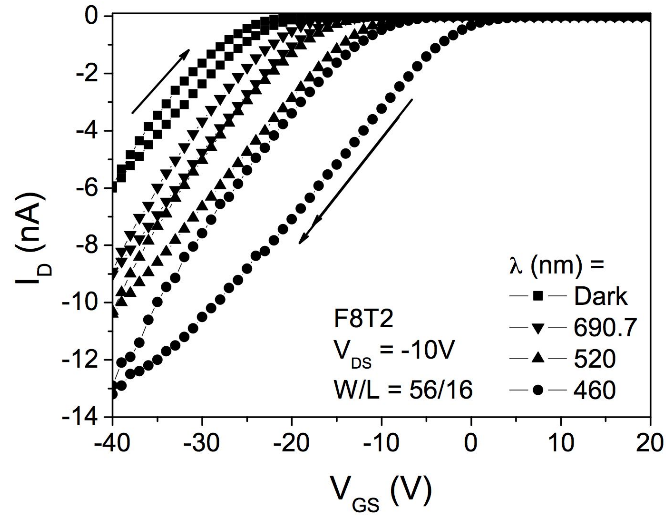

(a)

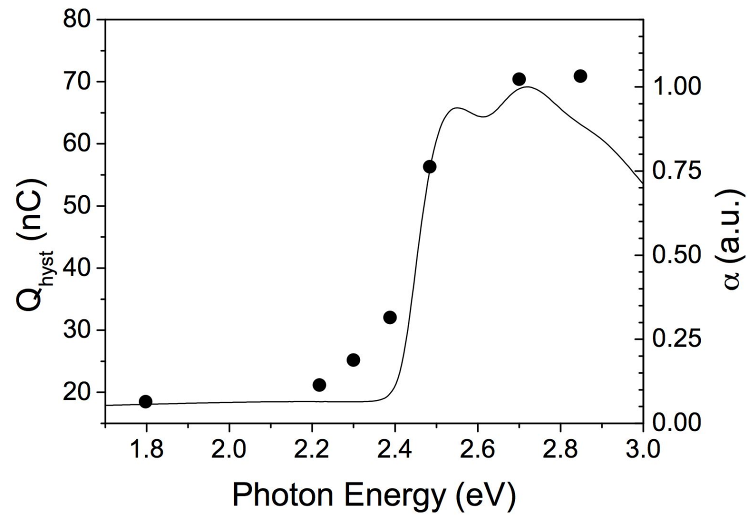

(b)

Figure 4.6: (a) Transfer characteristics (measured from OFF-SA-OFF, double arrow corresponds to first portion of measurement) of a device measured under illumination at different wavelengths for the same photon flux. (b) (filled circles) Dependence of hysteresis charge (taken from data presented in Figure 4.6(a) and (line) absorption coefficient on the energy of the incident photons.

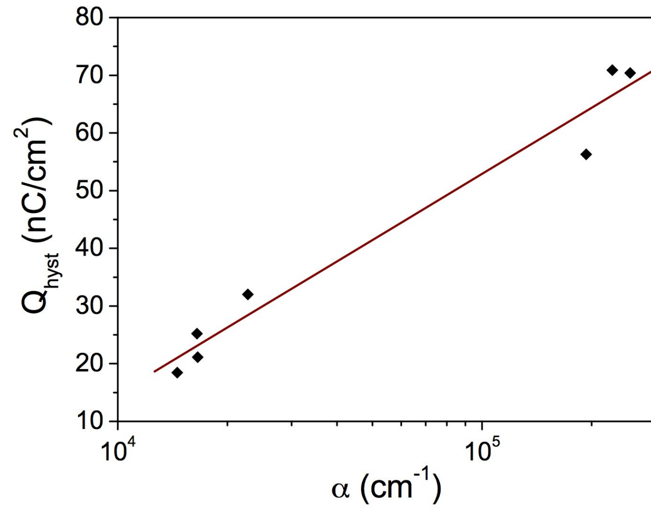

(a)

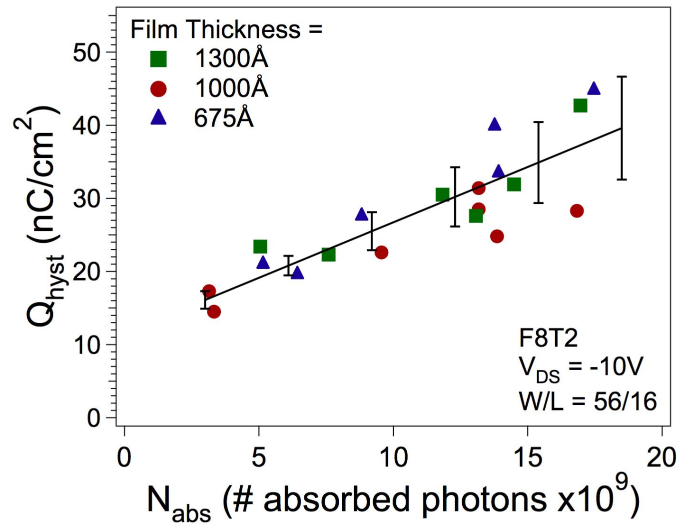

(b)

Figure 4.7: Hysteresis charge versus (a) absorption coefficient and (b) number of absorbed photons for devices of different thickness.

where α is the absorption coefficient of the polymer layer for the incident wavelength of the illumination (cm^{-1}) , N_{inc} is the incident flux of the monochromatic illumination photons ($\#/cm^2s$) , t is the time required to complete the measurement (s) and d is the thickness of the polymer layer (cm). When the data are presented as in Figure 4.7(b), the hysteresis charge shows a linear dependence on the number of absorbed photons. There is no observable dependence on film thickness, within the range of thicknesses we have used here.

The hysteresis charge, taken from Figure 4.8(a), is shown versus the irradiance level of 460nm illumination in Figure 4.8(b). We chose 460nm since it is within the range of strongly absorbed wavelengths. Since we expect that the higher irradiance should increase the charge carrier density in the channel due to a higher density of photogenerated carriers and since the hysteresis charge is dependent on the level of carrier density in the channel, the observed result of increasing hysteresis charge with increasing irradiance is the expected result.

4.2 Reduction of hysteresis

It has been observed that the hysteresis of similar devices can be reduced through the use of an organic insulator with a low dielectric constant [22], as well as through the use of inorganic insulators [6]. Veres, et al., have proposed that the localization of charge carriers in the vicinity of the channel region, which can lead to the observed hysteresis, can be enhanced by the increased energetic disorder and broadening of the semiconductor density of states due to dipolar disorder effects from an insulator with inherent polarization [22]. In other words, polarization at the surface of the insulator increases the (already present) energetic disorder within the organic semiconductor, near the interface, which leads to increased hysteresis. The use of insulators with low surface polarization (whether it is an

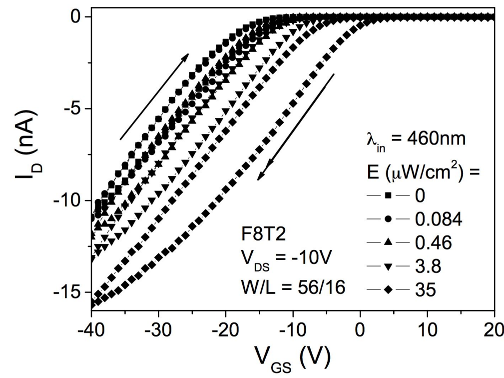

(a)

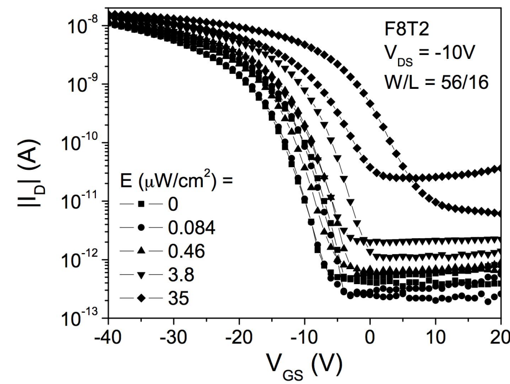

(b)

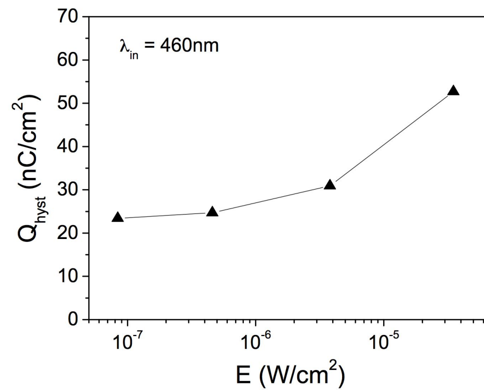

(c)

Figure 4.8: Transfer characteristics (from OFF to ON to OFF) for a device under monochromatic illumination at 460nm and different irradiance values shown on (a) linear and (b) semilog scales. (c) Q_{hyst} taken from transfer characteristics of Figure 4.8(a) measured under different illumination conditions.

organic or inorganic insulator) is therefore expected to allow a reduction of the hysteresis. We have observed that the hysteresis can be significantly reduced, if not eliminated through the use of a low temperature thermally cross-linkable organic gate insulator. This material can be cross-linked at temperatures as low as 100°C and possesses a relative dielectric constant of approximately 3.7. The transfer characteristics of two devices, one with only a thermally grown silicon oxide layer and one with similar structure but with the addition of a thin layer of Merck gate insulator (between the silicon oxide and F8T2), are presented in Figure 4.9. Each device uses the heavily doped Si substrate as the unpatterned gate electrode and thermally evaporated Au interdigitated top source and drain contacts.

These devices did exhibit a significant amount of gate leakage, which was similar

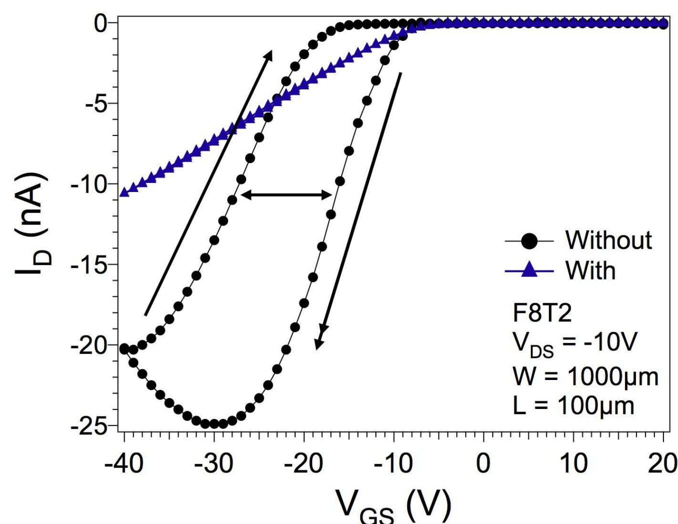

Figure 4.9: Linear regime transfer characteristics for two devices. Black circles are for a device using only SiO_2 as a gate insulator and blue triangles are for a device with the addition of an organic insulator between the SiO_2 and F8T2.

for each device, even with the addition of the organic insulator. The figure that is more important than the actual value of the gate leakage is the ratio of desired drain current to undesired gate leakage current, which can be thought of as a kind of signal to noise ratio.

For F8T2 devices with un-patterned gate electrodes, we note that the gate leakage current is of the same magnitude as the drain current, and affects the measurement of the drain current at high gate-to-source biases (above approximately -25V here). However, despite this non-ideality, we can see from the figure above that the addition of the Merck insulator reduces the hysteresis to well below our measurement uncertainties for gate voltage sweeps from OFF-ON-OFF. Additionally, note the linearity of the linear curve for the device with organic insulator compared to that for the device without the organic insulator. When the curves in Figure 4.9 are corrected by normalizing with capacitance (as shown in Figures 4.10(a) and 4.10(b), we find that the field-effect mobility is the same for each device, but the threshold gate charge is significantly reduced for the device with the organic insulator interlayer. The subthreshold swings of the devices (taken from the charge-normalized plots) show that the modified device turns on faster with gate charge. We also note that the normalization has no effect on the observed (and extracted) hysteresis of each curve. These results demonstrate that the reduction of charge trapping (localization) at the active layer/gate insulator interface, through the use of an organic (or otherwise low-κ) interlayer, has a profound effect on the electrical performance of the device by eliminating the hysteresis and reducing the threshold charge as well as the subthreshold swing.

4.3 Conclusion

All of these results support the idea that the hysteresis charge is dependent on the density of charge carriers in the channel. Additionally, it appears that the hysteresis may be tied to or result in a gate-bias-dependent threshold voltage, which is thought to arise from charges being trapped into surface states/interfacial traps. For example, as we bias the device from OFF to SA, charge carriers gradually fill up surface states causing a gradual shift in the threshold voltage. However, as we bias the device from SA to OFF, we expect most

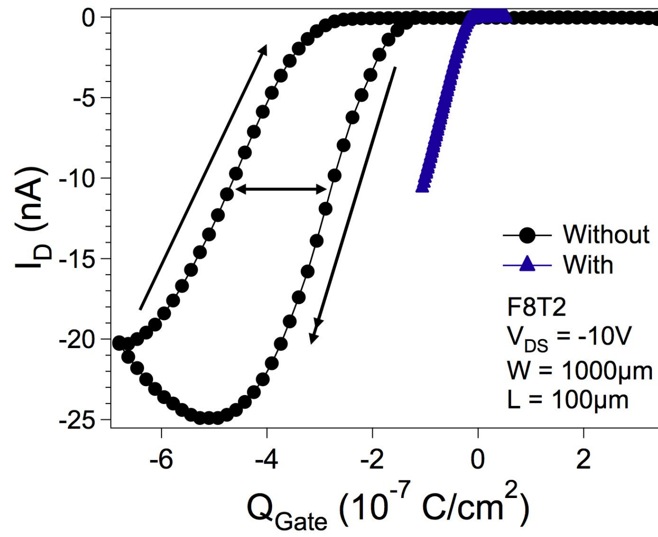

(a)

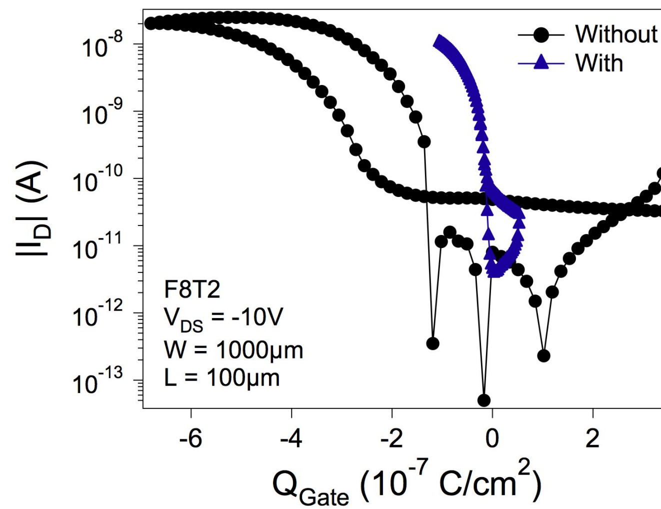

(b)

Figure 4.10: Normalized linear regime transfer characteristics of devices from Figure 4.9 plotted on (a) linear-linear and (b) semi-log scales to allow visual comparison of field-effect mobility, threshold charge and subthreshold swing.

of the change in threshold voltage (charge trapping into surface states/interfacial traps) to occur near the beginning of the measurement causing the observed behavior for the measurement in this direction. As we continue to move towards the OFF-state, the charges may/may not begin to be (slowly) liberated from these states. This is a possible explanation for the different threshold voltages observed for measurements from OFF to SA and SA to OFF, as well as the non-ideal curvature of the measurement from OFF to SA.

We have studied the hysteresis in the electrical characteristics of our organic field-effect transistors. While we observe significant hysteresis in the transfer characteristics, we see no appreciable hysteresis in the output characteristics. We have shown that the hysteresis width, which can be related to a hysteresis charge, depends strongly on the maximum gate-to-source voltage used, but not on either the measurement time nor the drain-to-source voltage. This leads us to believe that the hysteresis is related to the charge carrier trapping in the organic polymer, at or near the organic semiconductor / gate insulator interface, which is triggered by the accumulation of a large density of carriers in the polymer channel of the device.

Finally, we note that the hysteresis in the transfer characteristics of the F8T2-based devices is eliminated by the use of an organic insulator layer between the inorganic insulator and the active layer. This interlayer effectively reduces the threshold gate charge (related to the threshold voltage of the device) and reduces the gate-charge normalized subthreshold swing, while the field-effect mobility of the device remains relatively unchanged.

References

[1] S. Scheinert, G. Paasch, S. Pohlmann, H.-H. Hörhold, and R. Stockmann, “Field effect in organic devices with solution-doped arylamino-poly-(phenylene-vinylene),” *Solid-State Electron.*, vol. 44, pp. 845–853, 2000.

[2] S. Scheinert and W. Schliefke, “Analyzes of field effect devices based on poly(3-octylthiophene),” *Synth. Met.*, vol. 139, pp. 501–509, 2003.

[3] H. Klauk, G. Schmid, W. Radlik, W. Weber, L. Zhou, C. D. Sheraw, J. A. Nichols, and T. N. Jackson, “Contact resistance in organic thin film transistors,” *Solid-State Electron.*, vol. 47, pp. 297–301, 2003.

[4] S. Uemura, M. Yoshida, S. Hoshino, T. Kodzasa, and T. Kamata, “Investigation of surface modification of polymer as an insulator layer of organic fet,” *Thin Solid Films*, vol. 438-439, pp. 378–381, 2003.

[5] P. V. Pesavento, R. J. Chesterfield, C. R. Newman, and C. D. Frisbie, “Gated four-probe measurements on pentacene thin-film transistors: Contact resistance as a function of gate voltage and temperature,” *J. Appl. Phys.*, vol. 96, pp. 7312–7324, 2004.

[6] S. Yaginuma, J. Yamaguchi, K. Itaka, and H. Koinuma, “Pulsed laser deposition of oxide gate dielectrics for pentacene organic field-effect transistors,” *Thin Solid Films*, vol. 486, pp. 218–221, 2005.

[7] M. J. Panzer, C. R. Newman, and C. D. Frisbie, “Low-voltage operation of a pentacene field-effect transistor with a polymer electrolyte gate dielectric,” *Appl. Phys. Lett.*, vol. 86, p. 103503, 2005.

[8] L. A. Majewski and M. Grell, “Organic field-effect transistors with ultrathin modified gate insulator,” *Synth. Met.*, vol. 151, pp. 175–179, 2005.

[9] M. L. Chabinyc, J.-P. Lu, R. A. Street, Y. Wu, P. Liu, and B. S. Ong, “Short channel effects in regioregular poly(thiophene) thin film transistors,” *J. Appl. Phys.*, vol. 96, pp. 2063–2070, 2004.

[10] D. M. Taylor and C. A. Mills, “Memory effect in the current-voltage characteristic of a low-bandgap conjugated polymer,” *J. Appl. Phys.*, vol. 90, pp. 306–309, 2001.

[11] L. P. Ma, J. Liu, and Y. Yang, “Organic electrical bistable devices and rewritable memory cells,” *Appl. Phys. Lett.*, vol. 80, pp. 2997–2999, 2002.

[12] H. E. Katz, X. M. Hong, A. Dodabalapur, and R. Sarpeshkar, “Oranic field-effect transistors with polarizable gate insulators,” *J. Appl. Phys.*, vol. 91, pp. 1572–1576, 2002.

[13] T. Kodzasa, M. Yoshida, S. Uemura, and T. Kamata, “Memory effects of pentacene mfs-fet,” *Synth. Met.*, vol. 137, pp. 943–944, 2003.

[14] S. Kolliopoulou, D. Tsoukalas, P. Dimitrakis, P. Normand, H.-L. Zhang, N. Cant, S. D. Evans, S. Paul, C. Pearson, A. Molloy, and M. C. Petty, “A multi-stack insulator silicon-organic memory device with gold nanoparticles,” *ESSDERC ’03*, pp. 477–480, 2003.

[15] R. Schroeder, L. A. Majewski, and M. Grell, “All-organic permanent memory transistor using an amorphous, spin-cast ferroelectric-like gate insulator,” *Adv. Mater.*, vol. 16, pp. 633–636, 2004.

[16] E. Mizuno, M. Taniguchi, and T. Kawai, “Ambipolar organic field-effect transistor using gate insulator hysteresis,” *Appl. Phys. Lett.*, vol. 86, p. 143513, 2005.

[17] R. F. Pierret, *Semiconductor Device Physics*. Reading, MA: Addison-Wesley, 1996.

[18] A. Salleo, F. Endicott, and R. A. Street, “Reversible and irreversible trapping at room temperature in poly(thiophene) thin-film transistors,” *Appl. Phys. Lett.*, vol. 86, p. 263505, 2005.

[19] M. C. Hamilton, S. Martin, and J. Kanicki, “Field-effect mobility of organic polymer thin-film transistors,” *Chem. Mater.*, vol. 16, pp. 4699–4704, 2004.

[20] ——, “Thin-film organic polymer phototransistors,” *IEEE Trans. Electron Devices*, vol. 51, pp. 877–885, 2004.

[21] M. C. Hamilton and J. Kanicki, “Organic polymer thin-film transistor photosensors,” *IEEE J. Select. Topics Quantum Electron.*, vol. 10, pp. 840–848, 2004.

[22] J. Veres, S. D. Ogier, S. W. Leeming, D. C. Cupertino, and S. M. Khaffaf, “Low-k insulators as the choice of dielectrics in organic field-effect transistors,” *Adv. Funct. Mater.*, vol. 13, pp. 199–204, 2003.

CHAPTER 5

BIAS - TEMPERATURE STRESS AND INSTABILITIES OF PF-BASED OFETs

In general, the electrical properties of electronic devices are expected to change over the lifetime of the device, resulting in a degradation of the electrical performance of the device. It is important to minimize the device instability, to facilitate the development of reliable devices and applications. In order to develop robust devices that exhibit the smallest degradation over time, there is a need to investigate the effects of and understand the cause of the device degradation.

In this chapter, we describe the study of the instabilities of OFETs. The instability mechanisms are investigated through the means of bias-temperature stress (BTS) experiments, in which the device is subjected to a specified gate bias for a specified amount of time and at a specified temperature. We present the results of the effect of stress time, stress bias and stress temperature.

5.1 Bias -temperature stress of OFETs

It has been observed by many authors that the electrical performance of this class of devices can change significantly with time due to the electrical instabilities of the devices [1–6]. The electrical stability of OFETs is an important factor regardless of which

application is considered. For example, in active matrix flat panel display addressing, a threshold voltage shift of the OFET could result in a reduction of the pixel luminance unless it is compensated by the use of specific pixel electrode circuits.

In this section, we present the results of our study of the electrically- and thermally-induced instabilities of a polymer-based OFET through the use of accumulation (i.e., negative) bias-temperature stress [7,8]. For the case of negative DC BTS over long time scales (10^4sec), we have used both interrupted and non-interrupted stress methods measured over a range of temperatures (293K < T_{st} < 353K). The major observable effect is a shift of the threshold voltage to more negative values as the stress time accumulates, causing a decrease in the drain current at a specific applied gate bias. The observed dependence on stress temperature is analyzed in terms of the kinetics of the stress mechanism. This analysis is performed by unifying the threshold voltage shift curves through either the normalization of the accumulated stress time by a thermally activated time constant for the stress or by using a thermalization energy. The observed bias stress effects are reversible at room temperature in the dark. However, recovery of the device is accelerated at elevated temperatures and by illumination with strongly absorbed illumination, as has been observed by others [5], indicating charge trapping/de-trapping as the general stress/recovery mechanism.

5.1.1 Experimental methods

The bias temperature stress experiments and transfer characteristics measurements (drain current versus gate-to-source voltage, $I_D - V_{GS}$) of the OFET were performed in the dark, at various temperatures using a Karl Suss PM8 probe station, and an HP4156 semiconductor parameter analyzer controlled by Interactive Characterization Software (Metrics). The transfer characteristic measurements performed in this study were measured

from the strong accumulation (i.e., ON-state) to the OFF-state to provide the most reliable and repeatable results. A Signatone QuietTemp temperature controller and hot-chuck were used to control the temperature of the devices between 283K and 353K. All measurements were performed in ambient atmosphere.

5.1.2 Experimental results and analysis

DC BTS

Conventional bias temperature stress (BTS) experiments have been performed, in which the device is subjected to a constant (DC) gate bias for a given stress time, at a given stress temperature. At several pre-selected times, the stress is interrupted and the linear regime transfer characteristics are measured, followed by the continuation of the electrical stress. Transfer characteristics obtained after such a stress at room temperature are shown in Figure 5.1. We can clearly see in Figure 5.1 that a negative (i.e., accumulation) BTS, during which the device is biased in the accumulation regime, has a very large effect on the threshold voltage but does not significantly affect the field-effect mobility or subthreshold swing as shown in Figure 5.2. This is consistent with BTS experiments performed on inorganic devices, as well as other organic devices [2, 6, 8–14].

On the other hand, after a positive (i.e., depletion) BTS, during which the device is in the OFF-state, the electrical characteristics become degraded (threshold voltage shifts and subthreshold swing increases) for accumulated stress times up to approximately 1000 sec , as shown in Figure 5.3. However, as we can see in Figure 5.4, as the stress is continued to longer accumulated stress times, the device appears to begin to return to the normal, unstressed state. The threshold voltage and subthreshold swing return to pre-stressed values. One possible explanation for this observation is that the stress we are observing is due to the measurement of the device when the stress is interrupted and is not necessarily due to the applied positive gate bias.

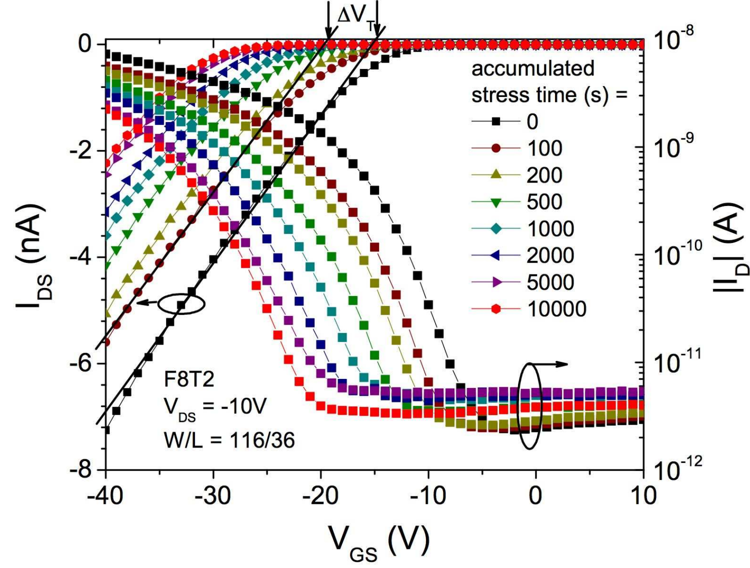

Figure 5.1: Typical linear regime transfer characteristics taken before and between bias stressing episodes. ΔV_T is defined in this plot as the voltage shift between the extracted threshold voltage before stressing and after stressing to a certain time.

We should note that, in both cases, the electrical performance of the device is restored after relaxation. In this study, we have focused on the negative electrical stress experiments. More precisely, we have investigated the dependence of the threshold voltage shift obtained after negative bias temperature stress with the stress parameters, i.e., stress time, stress voltage and stress temperature and relate the results to the distribution of trapped charge carriers with energy. The threshold voltage shift is defined as:

$$\Delta V_T(t_{st}) = V_T(t_{st}) - V_T(0) \tag{5.1}$$

where $V_T(t)$ is the threshold voltage extracted from the transfer characteristics of the OFET in the linear regime at the accumulated stress time t. It should be noted that this value of ΔV_T is similar to the voltage shift obtained by looking at a constant current in the subthreshold regime of the transfer characteristics. We have observed that the threshold voltage shift versus accumulated stress time curves can be fit by the following stretched exponential equation, based on the analysis developed for amorphous semiconductor-based

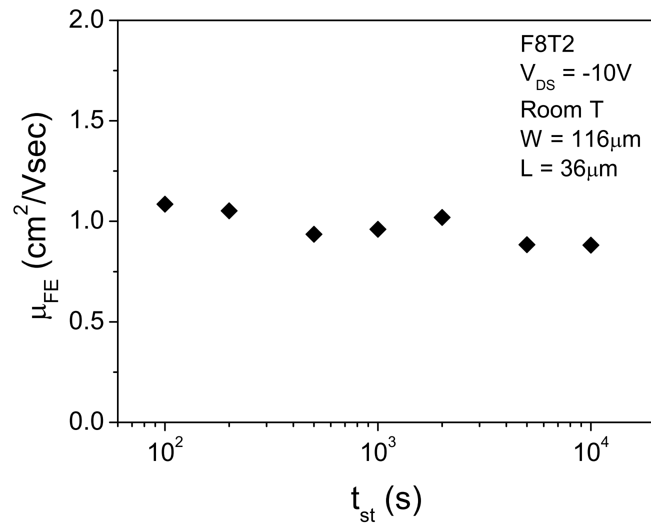

(a)

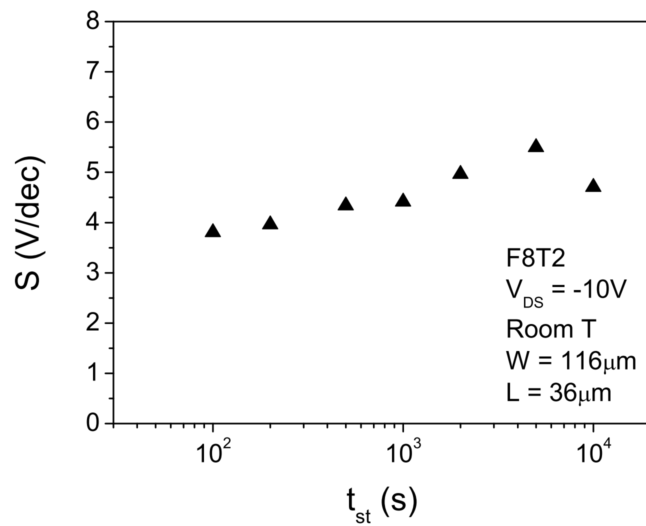

(b)

Figure 5.2: (a) Field-effect mobility and (b) subthreshold swing versus accumulated stress time for a DC accumulation BTS experiment, extracted from the data presented in Figure 5.1.

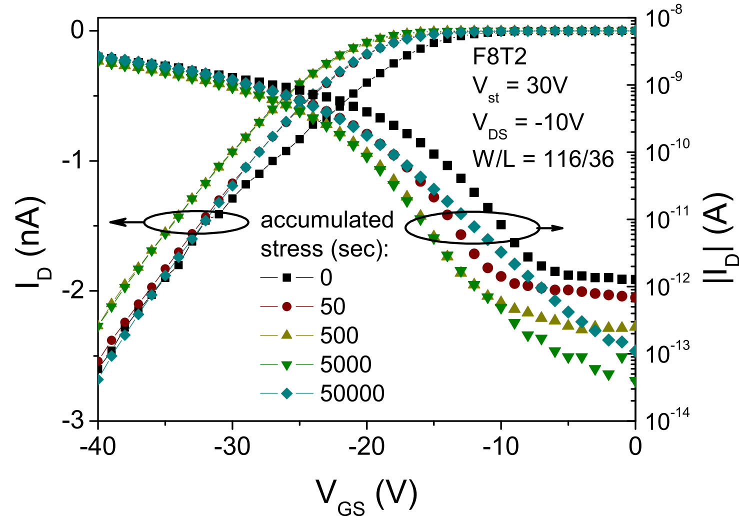

Figure 5.3: Typical linear regime transfer characteristics taken before and between DC depletion bias stressing episodes. ΔV_T is defined in this plot as the voltage shift between the extracted threshold voltage before stressing and after stressing to a certain time.

TFTs [10, 15–17]:

$$|\Delta V_T| = |B| \cdot \left(1 - e^{-\left(\frac{t}{\tau}\right)^{\beta}}\right) \tag{5.2}$$

where B, β and τ are fitting parameters that can depend on the stress voltage and stress temperature. In other amorphous semiconductor-based TFTs, B is strongly dependent on the stress voltage and has often been expressed by one of the following equations:

$$B = (V_{ST} - V_{Ti}) \tag{5.3a}$$

$$B \propto (V_{ST} - V_{Ti})^{\alpha} \tag{5.3b}$$

where α is a parameter associated with the density of states of the active layer semiconductor. For low temperature values (i.e., $T_{st} \lesssim 350$K), the fitting parameter β increases linearly with the stress temperature [10]:

$$\beta = T_{st}/T_o^* - \beta_o \tag{5.4}$$

where β_o and T_o^* are material-dependent parameters.

Figure 5.5a shows our experimental data obtained for OFETs subjected to different

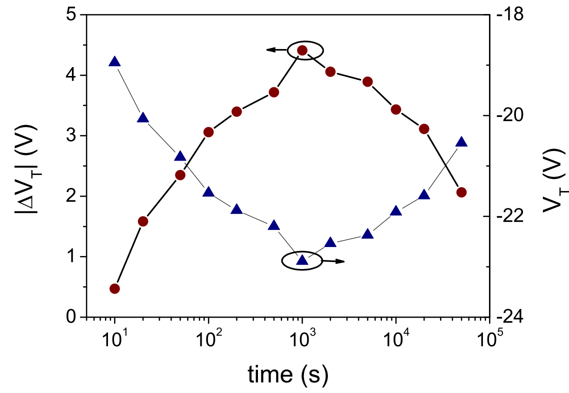

(a)

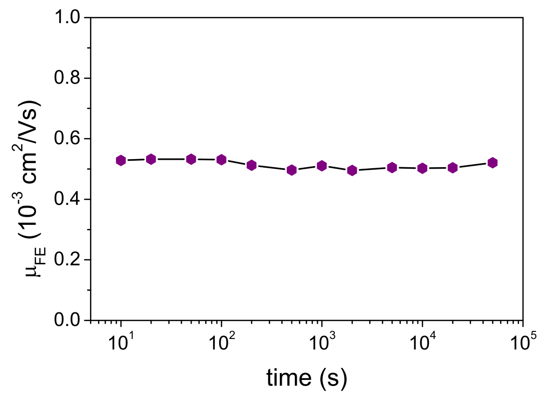

(b)

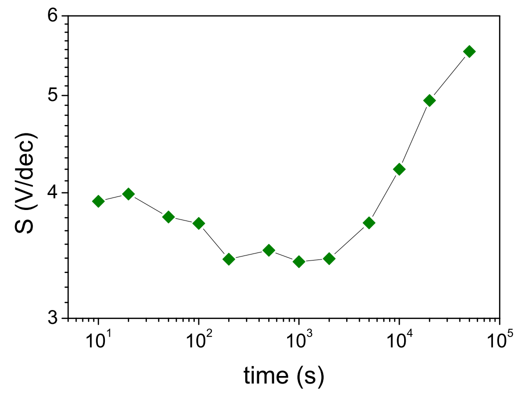

(c)

Figure 5.4: (a) Threshold voltage shift, (b) field-effect mobility and (c) subthreshold swing versus accumulated stress time for a DC depletion BTS experiment, extracted from the data presented in Figure 5.3.

BTS conditions and the corresponding fits to equation (5.2). We have obtained very acceptable fits using this equation for a significant range of stress voltages and stress temperatures.

We have also investigated the effect of the stress voltage and stress temperature on the

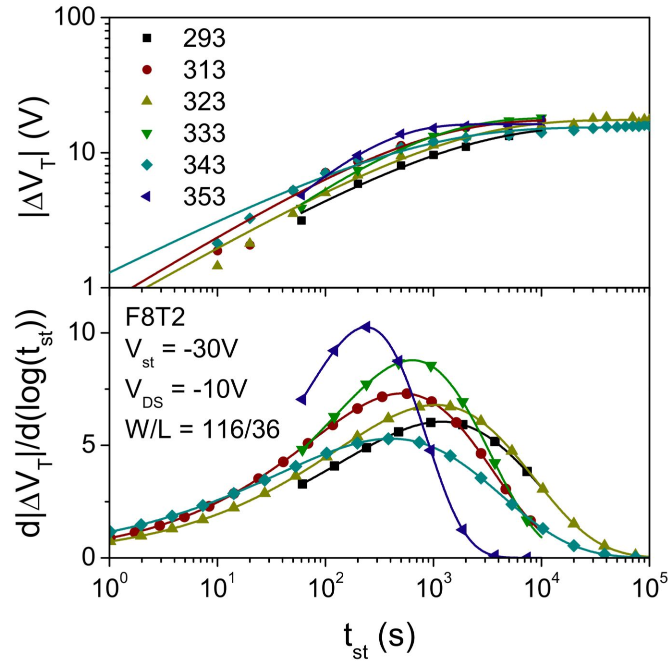

Figure 5.5: (a) Threshold voltage shift versus accumulated stress time for same OFET stressed at different stress temperatures. (b) Derivative of stretched exponential curves as a function of accumulated stress time, showing peak/inflection point times.

three fitting parameters and find similar dependencies as described by the equations above. The parameter β is roughly independent of the stress voltage and, similar to the case for BTS of other amorphous semiconductor-based TFTs (i.e., a-Si:H TFTs) β exhibits a slight increase with increasing temperature as shown in Figure 5.6 [10]. For stress temperature values higher than approximately 350K, we have observed that β saturates. As shown in Figure 5.6, the parameter τ decreases, exhibiting a power law dependence, with the stress voltage. In addition, τ has been shown to be activated in temperature with an activation energy E_τ that is associated with the barrier energy that the carriers need to overcome before

they become trapped [6, 13, 22]. The B parameter does not appear to depend strongly on stress/measurement temperature, but is strongly dependent on the applied stress bias. This is reasonable since B describes the saturation value of the shift of the threshold voltage.

Fitting the data of Figure 5.5(a)a with the stretched exponential equation gives a

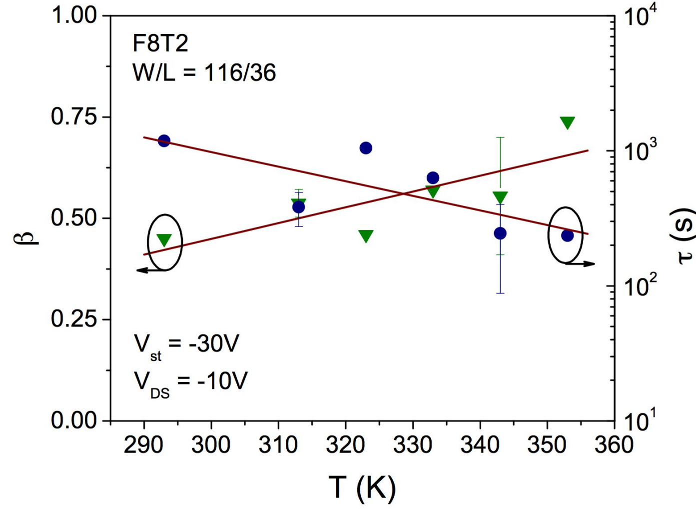

Figure 5.6: β and τ (taken from the stretched exponential fits) as a function of temperature.

smoother set of data for which we take the derivative to get the time to the inflection point (t_{peak}). In other words, we calculate:

$$\frac{d\left(|\Delta V_T|\right)}{d\left(logt\right)} \tag{5.5}$$

and plot this as a function of accumulated stress time as shown in Figure 5.5(b). We observed that the peak time t_{peak} and the τ parameter from the stretched exponential fits, shown in Figure 5.7, are both activated with temperature. This makes physical sense, since we expect that the bias-stress will occur faster at elevated temperature. The activation energy of the peak time is approximately 0.2eV, and was found from:

$$t_{peak} = t_o \cdot e^{E_a/kT_{st}} = \nu_o^{-1} \cdot e^{E_a/kT_{st}} \tag{5.6}$$

Additionally, a value of t_o of approximately 0.4s corresponding to a value of ν_o of 2.5Hz is

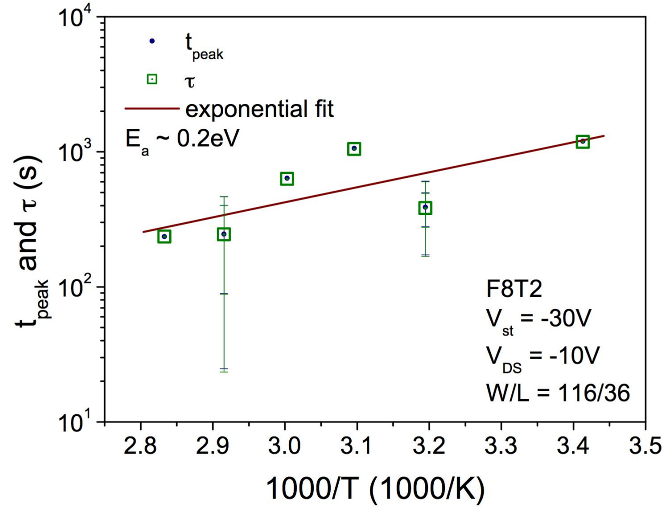

Figure 5.7: Arrhenius plot of peak/inflection time constant and τ.

found. An E_a of approximately $0.2eV$ has also been observed for the field effect mobility of F8T2-based OFETs. We expect that this energy corresponds to a charge trapping state around 0.2eV above the valence band and this is described in more detail below.

In Figure 5.8, we plot the threshold voltage shift as a function of the normalized accumulated stress time (i.e., $t^*_{st} = t_{st}/t_{peak}$). From this figure, we see that all of the curves unify. This result is evidence that the stress mechanism is similar throughout this range of temperatures and the observed differences caused by different stress temperatures arise from the kinetics of the mechanism.

Alternatively, as shown in Figure5.9(a), we can plot the threshold voltage shift as a function of the thermalization energy, which is defined as:

$$E_{st} = kT_{st} ln\left(\nu \cdot t_{st}\right) \tag{5.7}$$

where T_{st} is the temperature at which the BTS was performed, ν is the attempt-to-escape frequency and t_{st} is the accumulated stress time. The value of ν was chosen to give the best overlap of the curves, and can also be estimated from the equation above using ν_o. Here, we use $\nu = 10Hz$, a relatively slow frequency, possibly demonstrating that the physical

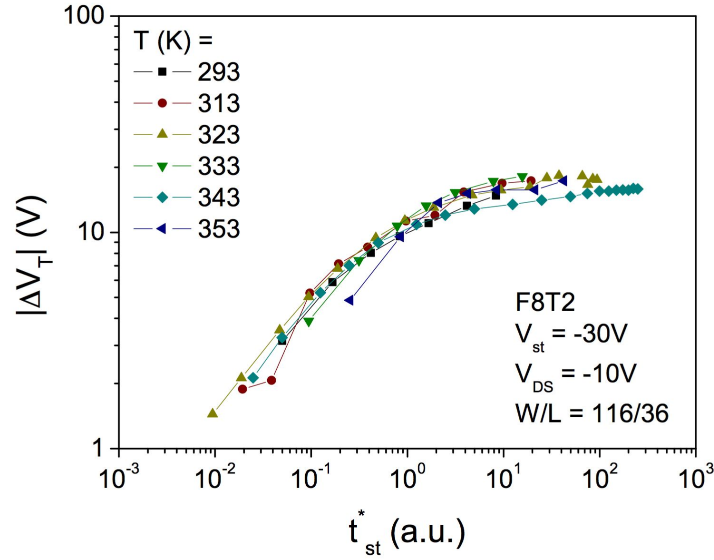

Figure 5.8: Threshold voltage shift versus normalized stress time for BTS at different stress temperatures.

mechanism responsible for the threshold voltage shift is slow (i.e., slow charge carrier movement as they are trapped and de-trapped).

A plot of the derivative of the stretched exponential fit curves versus stress energy as defined above (using $\nu = 10Hz$) is shown in Figure 5.9(b). According to Jackson , et al., [9, 16] the threshold voltage shift is related to the defect density (or, for the current case, trapped charge carriers) through the relation:

$$N(t) - N(0) = \Delta N = \frac{C_i}{l_d} [V_T(t) - V_T(0)] \tag{5.8}$$

where C_i is the insulator capacitance and l_d is the accumulation layer thickness. Or stated another way [16, 19]:

$$\Delta N_D \propto \frac{\epsilon_o \epsilon_{ins}}{q d_{ins}} \Delta V_T \tag{5.9}$$

These results state that the threshold voltage shift is directly proportional to the change in defect (trapped charge) density. Therefore to get the plot shown in Figure 5.9b, we used the same value of the derivative as before, but plotted the data as a function of energy. This

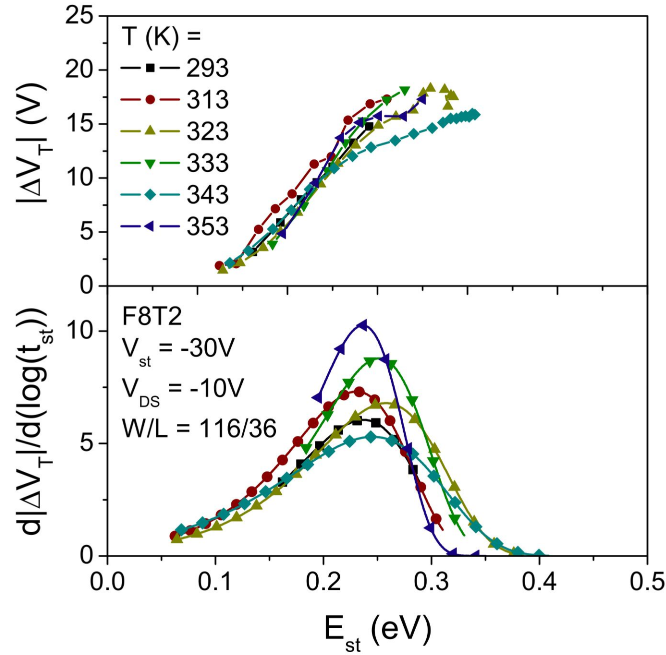

Figure 5.9: (a) Threshold voltage shift versus stress energy for BTS different temperatures. (b) Density of traps filled (or states formed) per unit energy as a function of the thermalization energy.

gives us a measure of the distribution of trapped charge carriers with energy, i.e.,:

$$\frac{dN}{dE} \propto \frac{d\left(|\Delta V_T|\right)}{d\left(logt\right)} \tag{5.10}$$

Interestingly, we also see that the curves appear to reach a maximum value around 0.25eV, which is near the activation energy of the time constants, and again, is expected to correspond to a charge trapping state at this energy above the valence band.

As noted above, we also observe a complete removal of the bias stress effects at room temperature and in the dark. However, recovery of the device is much faster at elevated temperatures and with strongly absorbed illumination, as has been observed by others [5]. These results are indicative of charge trapping/de-trapping as the general stress/recovery mechanism, though the exact physical nature of the charge trapping state is still under investigation.

AC BTS

The majority of bias stress studies on organic-based transistors found in the literature are for DC bias stress [1–4, 6, 18, 20, 21]. In this section we present our study of the effect of a pulsed (AC) bias stress signal applied to the gate and drain terminals and describe the observed effects on the electrical instabilities of OFETs based on a polymeric semiconductor. We have investigated the effects of AC BTS in both the accumulation and depletion regimes over a range of pulse frequencies and duty cycles. In each case, the observed effect is a threshold voltage shift, while the field-effect mobility remains constant. In general, and as discussed in the previous section on DC BTS, the bias stress-induced instabilities in organic semiconductors has been explained by the trapping of charge carriers in trap states within the organic semiconductor.

We have performed AC BTS for both the accumulation state (negative AC BTS) and depletion state (positive AC BTS) of F8T2-based OFETs. For these stress measurements, the gate and drain were pulsed at a certain predetermined frequency between 0Hz (DC) and 100Hz and a certain duty cycle between 100% and 1%, while the source was held constant as the common electrode. For the negative AC BTS, the gate electrode was pulsed with $V_{GS} = V_{ST} =$ -30V and for the positive AC BTS, the gate electrode was pulsed with $V_{GS} = V_{ST} =$ +30V. For each stress, the drain was pulsed with $V_{DS} =$ -10V at the same frequency and duty cycle. A schematic of the gate-to-source and drain-to-source bias stress signals is presented in Figure 5.10. The stress was interrupted at certain times to allow the measurement of and the observation of the progression of the linear regime transfer characteristic, as shown in Figure 5.11. Conventional BTS experiments performed in this manner allow the extraction and determination of the evolution of the threshold voltage, field-effect mobility and subthreshold swing as the bias stress progresses.

In general, as presented in Figure 5.11, the major effect of the AC BTS is a con-

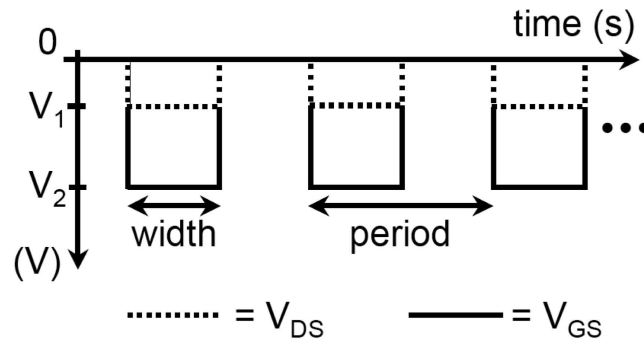

Figure 5.10: Schematic diagram of gate and drain bias pulse signals used in this work. Note that the dashed line corresponds to the drain-to-source bias pulse signal, the solid line corresponds to the gate-to-source bias pulse signal and $V_{DS} = V_{GS} = 0$ between pulses.

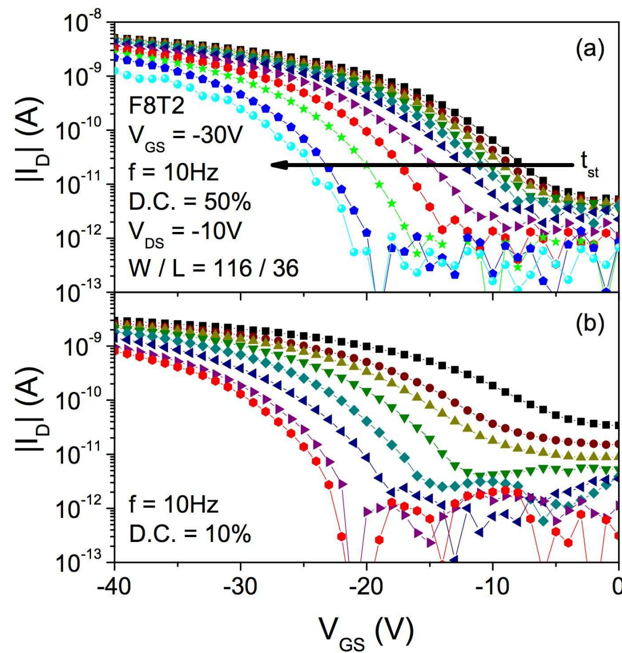

Figure 5.11: Representative evolution of the transfer characteristics measured during the interruptions of a bias stress performed with an AC gate bias frequency of 10Hz and duty cycles of (a) 50% and (b) 10% .

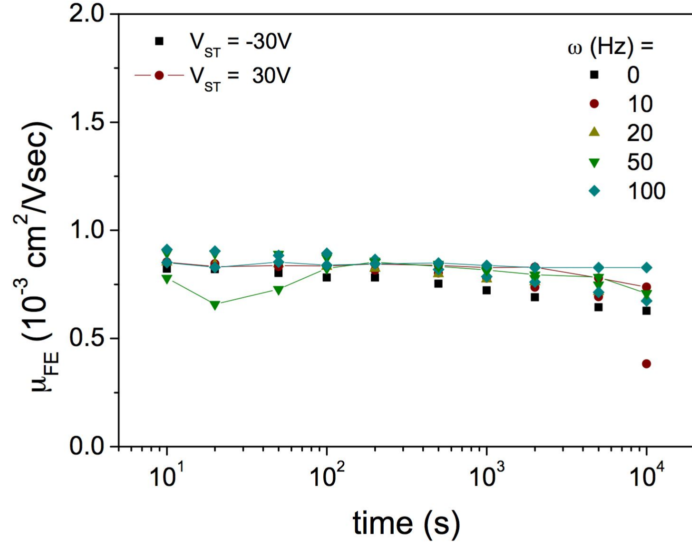

Figure 5.12: Variation of field-effect mobility taken from the data presented in Figure 5.11(a), as well as for AC BTS measurements performed at a duty cycle of 50 % at other frequencies.

tinuous threshold voltage shift as the stress progresses, similar to the case of DC BTS. The field-effect mobility remains constant throughout the duration of the stress and is not significantly affected by the negative (nor negative) AC BTS as shown in Figure 5.12. From Figure 5.11, we see that the subthreshold swing decreases (improves) as the stress progresses. A reasonable explanation for this observation is that as the AC bias-stress progresses, trap states near the Fermi level in the F8T2 become filled, allowing the device to turn on "faster" with gate bias below threshold, although we did not observe this same feature for the case of DC BTS presented above.

In Figure 5.13, we present the variation of the threshold voltage shift with the effective accumulated stress time. Here, we define the threshold voltage shift as:

$$\Delta V_T(t_{st}) = V_T(t_{st}) - V_T(0) \tag{5.11}$$

and the effective accumulated stress time is defined as:

$$t_{eff} = t_{st} \cdot D.C. \tag{5.12}$$

where *D.C.* is the duty cycle of the bias signals and is defined as:

$$D.C. = pulse\ width/pulse\ period \tag{5.13}$$

and the pulse width and pulse period are defined as in Figure 5.10. We see from Figure 5.13(a) that, for the range of pulse frequencies used, during negative AC BTS the threshold voltage shift is relatively independent of the pulse frequency and gives similar results to that found for the negative DC BTS. For the positive AC BTS, we observe that, for this device, there is a small negative threshold voltage shift which maximizes relatively quickly (compared to the negative BTS case). It also appears that during further stressing, the threshold voltage shift begins to swing back towards a positive threshold voltage shift. For the range of pulse frequencies used here, the threshold voltage shift does not seem to exhibit any discernable dependence on the pulse frequency.

We present the evolution of the threshold voltage shift with accumulated stress time for the case of negative AC bias stress signals, performed at the same frequency with different duty cycles, in Figure 5.13(b). As plotted in this figure, it is difficult to detect any trend in the results. However, when the threshold voltage shift is plotted versus the total time (i.e., real time, not normalized with the duty cycle), as in Figure 5.14, we see that the bias stress effects exhibit a dependence on the total amount of stress time.

We have fit the data of Figure 5.14 to the stretched exponential equation (5.2), based on the analysis developed for amorphous semiconductor-based TFTs and described in detail above. For the data of Figure 5.14, we find values of $|B|$, β, and τ to be approximately 15.3V, 0.46 and 874sec, respectively.

The observed dependence of the threshold voltage shift on the total stress time is an interesting result which goes against the expected result that the threshold voltage shift should only depend on the actual time the gate bias is being applied (i.e., t_{eff}). These results can be compared to the results found for poly(thiophene) transistors by Salleo , et

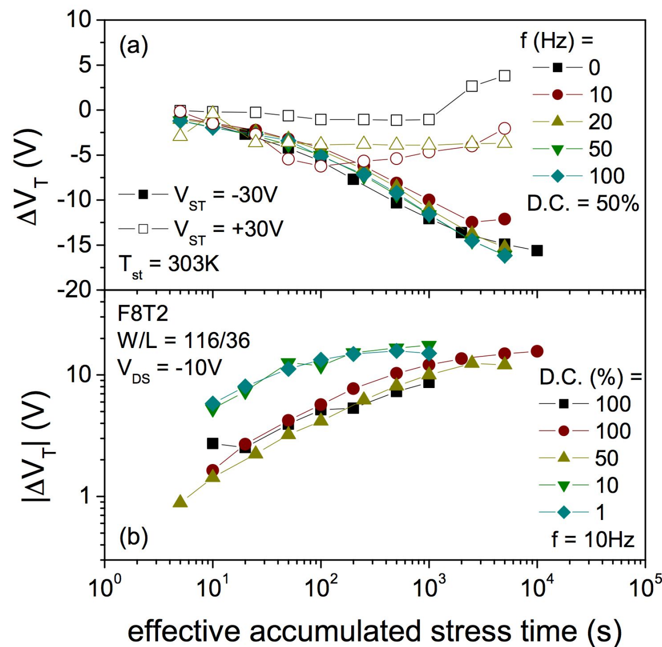

Figure 5.13: (a) Threshold voltage shift for negative AC (filled symbols) and positive AC (open symbols) BTS, performed using a range of pulse frequencies, plotted versus effective accumulated stress time (i.e., taking into account that for pulsed signals at 50% duty cycle, the effective bias time is half of the total stress time). (b) Threshold voltage shift versus effective accumulated stress time for BTS performed using a range of gate bias stress pulse signal duty cycles.

al., in which there exists a residual (or, in the words of the author, “irreversible”) stress effect after the stress bias is removed and the device is allowed to recover unperturbed for several hours [22]. For the present case, however, this residual stress is observed during the bias stress, because the device is apparently unable to recover during the “OFF” portion of the bias stress signal. Even more, the device appears to continue to be stressed during the ”OFF”-time. A possible explanation for this effect is that the carriers remain in the channel of the device, even after the gate-to-source bias has been removed (i.e., the ”OFF” portion of the gate bias pulse signal). This can be caused by the removal of the drain-to-source bias, as well as to the relatively low field-effect mobility of the holes in F8T2. We observe this effect for duty cycles down to 1% for OFETs based on F8T2. We expect that these

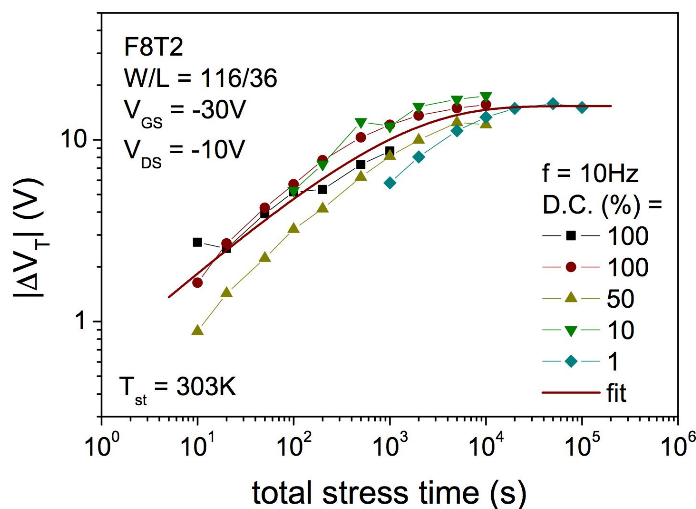

Figure 5.14: Threshold voltage shift versus total stress time for BTS performed using a gate bias stress pulse signal with a range of duty cycles. The solid, interpolating line represents a stretched exponential fit to the average of the experimental data.

results are further evidence of deep charge trapping within the organic semiconductor as the physical mechanism responsible for the electrical instabilities of these devices.

5.2 Maximum operating temperature

Another important environmental variable to which OFETs will be subjected is temperature. It is well documented and commonly assumed that since the field-effect mobility of most organic semiconductors used in OFETs is thermally activated, increased temperature operation is beneficial, or at least not detrimental to the performance of the OFETs [23–27]. However, besides the observation of accelerated bias-stressing at elevated temperature as shown above, there appears to be another means by which the electrical performance of the OFETs is degraded at elevated temperature. As shown in Figure 5.15(a) and 5.15(b), we observe that the field-effect mobility is effectively reduced for devices operated above approximately 60 to 65°C(333 to 338K). Although not specifically mentioned, similar results can be found in the references mentioned above, i.e., there appears

to be a decrease in the field-effect mobility for elevated temperatures near 65°C. To eliminate the possibility of the gate bias effecting the morphology of the material at higher temperatures (i.e gate-polling effects), we show in Figure 5.15(c) the characteristics of a device measured with the gate floating. In this figure, we still observe a reduction in the drain current at elevated temperature.

These results are for devices with active layer material that has been subjected to a maximum annealing temperature of 90°C(in vacuum) during device processing and post-measurement annealing sessions, allowing reliable device measurement up to approximately 90°C. We have observed similar results for devices that have been annealed and electrically tested to gradually higher temperatures (90°C- 110°C- 130°C).

We note several effects due to annealing and testing the device at gradually higher temperature. First, we see that the baseline field-effect mobility (i.e., that taken from device measured well below the annealing temperature) is reduced as the annealing temperature is increased. Another major effect is that even though the device has been annealed to higher temperature, the field-effect mobility is still a maximum for devices measured below 70°C. We expect that this reduction in mobility is caused by changes in the morphology of the organic semiconductor. However, attempts to discern these small changes (i.e., through temperature dependent X-ray diffraction (XRD) and differential scanning calorimetry (DSC) over the range of temperature used for the electrical characterization) did not produce any definite results. Since extremely small changes in morphology can result in substantial changes in electrical performance, it seems reasonable that experimentally undetectable changes in the morphology of the films used here may still be responsible for the reduction in device performance we have observed. Nevertheless, the subject of maximum operating temperature is an important characteristic of device performance and these results demonstrate that OFETs based on polymeric materials could have

an upper operating temperature limit much lower than anticipated strictly from a material degradation point-of-view.

5.3 Conclusion

We have studied the electrically induced instabilities of organic field-effect transistors based on solution-deposited F8T2. The main consequence of negative bias temperature stress is a shift of the threshold voltage to more negative values, while the field-effect mobility and subthreshold swing are relatively unaffected. These observations are explained in terms of charge carrier trapping in the disordered organic semiconductor active layer. We have used an analysis technique based on the dispersion of carriers among a range of trap states, in order to extract an estimation of the trap state distribution. We find that this distribution is centered at approximately 0.25eV above the valence band of the organic semiconductor and propose that this corresponds to a distribution of trap states centered at this energy.

As a complementary experiment, we have studied the electrically induced instabilities of organic field-effect transistors based on solution-deposited F8T2 by performing AC bias temperature stress experiments for a range of bias stress signal frequencies and duty cycles and investigating the evolution of the resulting threshold voltage shift. We find that the threshold voltage shift does not exhibit the expected dependence on the effective accumulated stress time, rather it depends on the total duration of the stress measurement. This result is explained in terms of deep trapping of charge carriers in combination with relatively low charge carrier mobility within the organic semiconductor, keeping the device from recovering during the "OFF" portion of the bias stress signal.

Additionally, we have noted that the electrical performance of the F8T2-based OFETs,

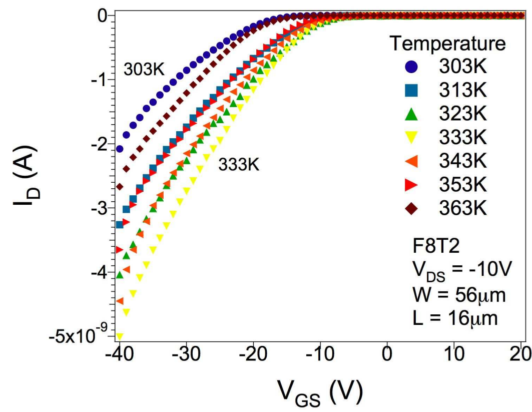

(a)

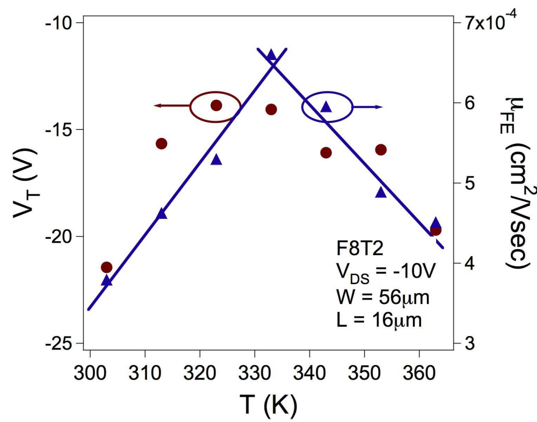

(b)

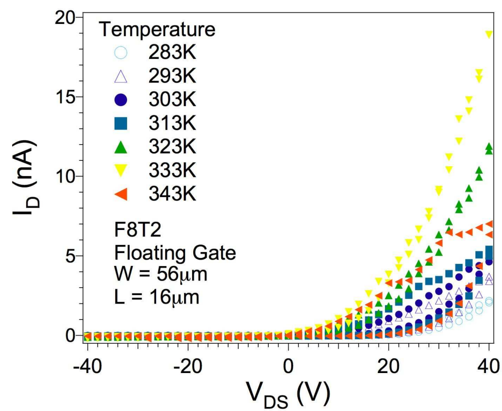

(c)

Figure 5.15: (a) Linear regime transfer characteristics for device measured at several different temperatures. (b) Threshold voltage and field-effect mobility extracted from data in Figure 5.15(a). (c) Drain current versus drain-to-source bias (for floating gate electrode) measured at different temperatures.

as well as OFETs based on other organic semiconductors, appears to increase, peak and then decrease as the temperature of the device is increased. Though we believe that this is due to small changes in the morphology of the organic film, experiments to detect such changes were not fruitful. This effect could have profound influence on the development of commercial applications based on this type of devices, since, it is expect that in most applications, the devices will be subjected to temperatures in excess of the peak performance temperature.

References

[1] A. R. Brown, C. P. Jarrett, D. M. deLeeuw, and M. Matters, "Field-effect transistors made from solution-processed organic semiconductors," *Synth. Met.*, vol. 88, pp. 37–55, 1997.

[2] W. A. Schoonveld, J. B. Oostinga, J. Vrijmoeth, and T. M. Klapwijk, "Charge trapping instabilities of sexithiophene thin film transistors," *Synth. Met.*, vol. 101, pp. 608–609, 1999.

[3] S. J. Zilker, C. Detcheverry, E. Cantatore, and D. M. de Leeuw, "Bias stress in organic thin-film transistors and logic gates," *Appl. Phys. Lett.*, vol. 79, pp. 1124–1126, 2001.

[4] S. Martin, L. Dassas, M. C. Hamilton, and J. Kanicki, "Time dependence of organic polymer thin-film transistors current," *Proc. of the SPIE*, vol. 5217, pp. 7–15, 2003.

[5] A. Salleo and R. A. Street, "Light-induced bias stress reversal in polyfluorene thin-film transistors," *J. Appl. Phys.*, vol. 94, pp. 471–479, 2003.

[6] H. L. Gomes, P. Stallinga, F. Dinelli, M. Murgia, F. Biscarini, D. M. de Leeuw, T. Muck, J. Geurts, L. W. Molenkamp, and V. Wagner, "Bias-induced threshold voltage shifts in thin-film organic transistors," *Appl. Phys. Lett.*, vol. 84, pp. 3184–3186, 2004.

[7] M. C. Hamilton, S. Martin, L. Dassas, and J. Kanicki "Time and temperature dependence of the drain current of PF-based OFETs," *Conference Digest of DRC*, vol. 63rd, pp. 139–140, 2004.

[8] M. C. Hamilton, and J. Kanicki "DC Bias-Temperature Stress of Polyfluorene-Based Organic Field-Effect Transistors," *submitted for publication*, 2005.

[9] W. B. Jackson, J. M. Marshall, and M. D. Moyer, "Role of hydrogen in the formation of metastable defects in hydrogenated amorphous silicon," *Phys. Rev. B*, vol. 39, pp. 1164–1179, 1989.

[10] F. R. Libsch and J. Kanicki, "Bias-stress-induced stretched-exponential time dependence of charge injection and trapping in amorphous thin-film transistors," *Appl. Phys. Lett.*, vol. 62, pp. 1286–1288, 1993.

[11] C.-S. Chiang, J. Kanicki, and K. Takechi, "Electrical instability of hydrogenated amorphous silicon thin-film transistors for active-matrix liquid-crystal displays," *Jpn. J. Appl. Phys.*, vol. 37, pp. 4704–4710, 1998.

[12] D. Knipp, R. A. Street, A. Völkel, and J. Ho, "Pentacene thin film transistors on inorganic dielectrics: Morphology, structural properties, and electronic transport," *J. Appl. Phys.*, vol. 93, pp. 347–355, 2003.

[13] A. Salleo and R. A. Street, "Kinetics of bias stress and bipolaron formation in polythiophene," *Phys. Rev. B*, vol. 70, p. 235324, 2004.

[14] S. Martin, L. Dassas, M. Hamilton, and J. Kanicki, "Electrical instabilities and relaxation of organic polymer thin-film transistors," *Proc. of the IDRC 2003*, pp. 22–25, 2003.

[15] J. Kakalios, R. A. Street, and W. B. Jackson, "Stretched-exponential relaxation arising from dispersive diffusion of hydrogen in amorphous silicon," *Phys. Rev. Lett.*, vol. 59, pp. 1037–1040, 1987.

[16] W. B. Jackson, "Role of band-tail carriers in metastable defect formation and annealing in hydrogenated amorphous silicon," *Phys. Rev. B*, vol. 41, pp. 1059–1075, 1990.

[17] R. S. Crandall, "Defect relaxation in amorphous silicon: Stretched exponentials, the meyer-neldel rule, and the staebler-wronski effect," *Phys. Rev. B*, vol. 43, pp. 4057–4069, 1991.

[18] R. A. Street, A. Salleo, and M. L. Chabinyc, "Bipolaron mechanism for bias-stress effects in polymer transistors," *Phil. Rev. B*, vol. 68, p. 085316, 2003.

[19] S. C. Deane, R. B. Wehrspohn, and M. J. Powell, "Unification of the time and temperature dependence of dangling-bond-defect creation and removal in amorphous-silicon thin-film transistors," *Phys. Rev. B*, vol. 58, pp. 12 625–12 628, 1998.

[20] I. Torres, D. M. Taylor, and E. Itoh, "Interface states and depletion-induced threshold voltage instability in organic metal-insulator-semiconductor structures," *Appl. Phys. Lett.*, vol. 85, pp. 314–316, 2004.

[21] J. Yuan, J. Zhang, J. Wang, D. Yan, and W. Xu, "Study on the instability of organic field-effect transistors based on fluorinated copper phthlocyanine," *Thin Sol. Films*, vol. 450, pp. 316–319, 2004.

[22] A. Salleo, F. Endicott, and R. A. Street, "Reversible and irreversible trapping at room temperature in poly(thiophene) thin-film transistors," *Appl. Phys. Lett.*, vol. 86, p. 263505, 2005.

[23] D. Hertel, H. Bässler, U. Scherf, and H. H. Hörhold, "Charge carrier transport in conjugated polymers," *J. Chem. Phys.*, vol. 110, pp. 9214–9222, 1999.

[24] G. Horowitz, M. E. Hajlaoui, and R. Hajlaoui, "Temperature and gate voltage dependence of hole mobility in polycrystalline oligothiophene thin-film transistors," *J. Appl. Phys.*, vol. 87, pp. 4456–4463, 2000.

[25] M.-S. Nam, A. Ardavan, R. J. Cava, and P. M. Chaikin, "Intrinsic electronic transport properties of organic field-effect transistors based on single crystalline tetramethyltetraselenafulvalene," *Appl. Phys. Lett.*, vol. 83, pp. 4782–4784, 2003.

[26] M. C. Hamilton, S. Martin, and J. Kanicki, "Field-effect mobility of organic polymer thin-film transistors," *Chem. Mater.*, vol. 16, pp. 4699–4704, 2004.

[27] R. A. Street, J. E. Northrup, and A. Salleo, "Transport in polycrystalline polymer thin-film transistors," *Phil. Rev. B*, vol. 71, p. 165202, 2005.

CHAPTER 6

PHOTODISCHARGE INVESTIGATION OF THE DENSITY OF STATES IN PF-BASED OFETS

The photodischage method was first used by Hepburn , et al., when they used it to investigate the kinetics of metastable defect states in a-Si:H TFTs [1, 2]. In this experiment, a transistor is biased for a certain time such that charge carriers are trapped within the device (i.e., electrons are trapped and defect states are created in a-Si:H). After a certain preselected delay time, the device is subjected to an illumination pulse, of which the photon energy and flux is proper to generate a sufficient density of free charge carriers. One species of photogenerated charge carriers (i.e., holes in a-Si:H) diffuses towards the gate insulator and annihilates the trapped electrons, while the other species (i.e., electrons in a-Si:H) travels in the opposite direction out the source and drain electrodes and can be measured as a transient current pulse. By varying the gate bias application time, delay time and device temperature, the kinetics of the trap states can be investigated and the density of these trap states can be estimated.

Other methods, such as deep level transient spectroscopy (DLTS) and thermally stimulated currents (TSC) have been used to characterize the trap states in organic semiconductors. In general, these two methods have been performed on either diode structures (i.e., organic light-emitting diodes, OLEDs) or metal-insualtor-semiconductor (MIS) structures.

For example, several groups have investigated the trap states of the light-emitting polymer poly-(p-phenylene-vinylene) (PPV), and its derivatives, and found that hole trap concentrations of 10^{14} to 10^{15} cm^{-3} at energies of 0.1 to 0.5eV above the valence band (or HOMO level) exist in this material [3–6]. TSC and DLTS studies of the defect states in pentacene diodes and MIS structures revealed a range of both electron and hole trap states with similar concentrations ($\backsim 10^{15}$) in the range of 0.2 to 1.0eV above the valence band [7, 8]. These methods have also shown use in determining trap and defect states caused by variations in processing conditions and molecular synthesis [9, 10], as well as detecting the creation and disappearance of a trap state as the doping level of a small organic material was increased [11].

For the first time, we have studied the defect kinetics of trap states in F8T2-based OFETs using the photodischarge technique. By varying the measurement conditions, including bias time, bias level and device temperature, we can estimate the density and energetic distribution of the trapped charge carriers. We find that the trapped charge carriers are centered at a narrow level, approximately 0.3eV above the valence band. This method provides promising and reliable results.

6.1 Experimental methods

The photodischarge measurements were performed at various temperatures using a Karl Suss PM8 probe station, and an HP4156 semiconductor parameter analyzer. A Signatone QuiteTemp temperature controller and hot-chuck were used to control the temperature of the devices between 283K and 353K. All measurements were performed in ambient atmosphere.

A schematic diagram of the photodischarge measurement set-up and a schematic of the measurement timeline used to perform each of the photodischarge experiments described

in this work are shown in Figures 6.1(a) and 6.1(b), respectively. For the photodischarge measurements of TFT structures, the source and drain electrodes are tied together and the gate is biased with respect to the source/drain connection. The source and drain connection is connected to the input of an Ithaco 1211 preamplifier (powered by internal batteries for reduced noise operation) in order to provide a voltage signal that could be measured with an oscilloscope. We have used an HP4156 semiconductor parameter analyzer to provide the gate bias signal for a certain time, t_g. After a certain delay time, t_d, an HP8110A function generator is used to trigger an electronic shutter (UniBlitz SD-1000), which opens to provide an illumination pulse with a width of approximately 200msec from a 200W Oriel HgXe arc lamp. This light pulse travels through a fiber optic cable into the microscope of the Karl Suss PM8 probe station and is focused to a spot size centered on and approximately the same size as the device under test. At the same time, the signal from the HP8110A triggers an HP54615B oscilloscope to measure the output voltage transient from the Ithaco 1211 current preamplifier.

6.2 Experimental results and analysis

6.2.1 Dependence on applied gate voltage

As noted above, the illumination pulse photogenerates charge carriers that perform the duty of a probe signal and cause a transient current pulse that is input into a current amplifier in order to generate a corresponding voltage signal. Representative transient voltage signals taken from the oscilloscope are presented in Figure 6.2 for a gate bias of -50V and a range of gate bias application times. This voltage signal is measured with an oscilloscope and is converted back to a current signal, which is then integrated to yield the total residual charge, Q, for each gate-bias application and delay time combination

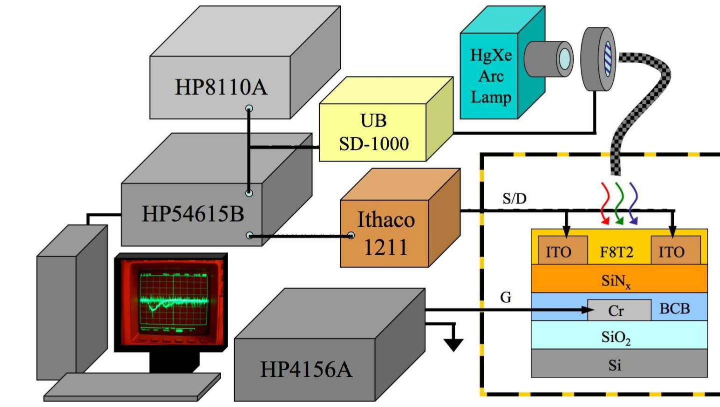

(a)

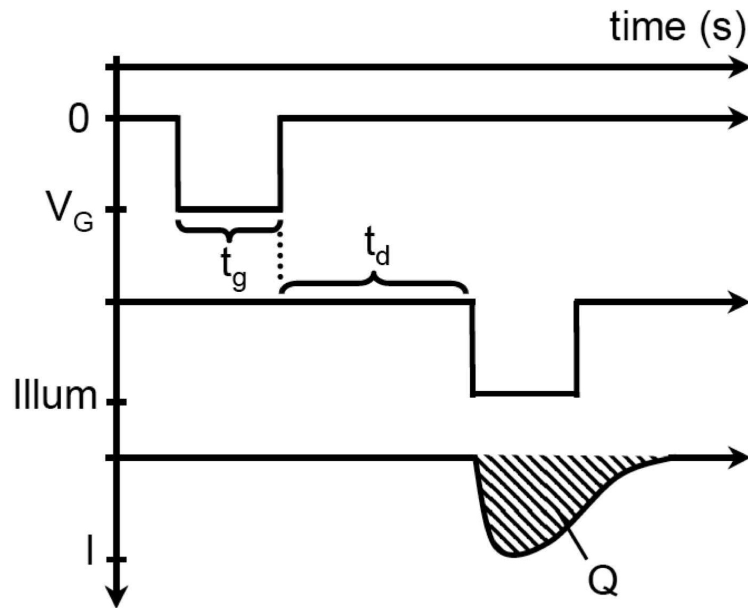

(b)

Figure 6.1: (a) Experimental set-up used to perform the photodischarge measurements. The dashed line around the schematic device structure corresponds to the electromagnetic shield around the probe-station used in the experiment. (b) Timescale of the photodischarge experiments showing the gate bias pulse for t_g, delay time t_d, illumination pulse, resulting current transient $I(t)$and residual charge Q.

according to:

$$I(t) = \frac{dQ}{dt} \Rightarrow Q = \int_0^{t_1} I(t)\,dt \tag{6.1}$$

where, for the case here, Q is found from:

$$Q = \int_0^{0.4} V_{scope}(t)\,[V] \cdot 10^{-9} \left[\frac{\frac{C}{s}}{V}\right] \cdot \frac{1}{1.602 \times 10^{-19}} \left[\frac{q}{C}\right] dt \tag{6.2}$$

where 10^{-9} is the amplification factor from the settings of the Ithaco 1211 current amplifier (i.e., $10^{-10} * 10 = 10^{-9}$).

The dependence of the residual charge on the applied gate bias, for a device at 303K,

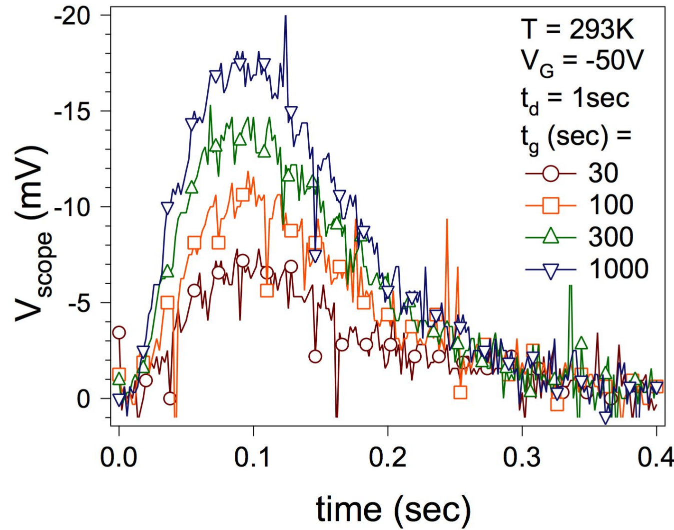

Figure 6.2: Representative set of voltage pulses as observed on the oscilloscope corresponding to the photo-discharging of the remaining filled trap states after the given gate bias application times and a delay time of approximately one second. Similar results were observed for other measurement temperatures.

is presented in Figure 6.3. We note that the residual charge exhibits the expected dependence on applied gate bias, i.e., it increases as the magnitude of gate bias increases as shown in Figure 6.3(a). For gate biases above the threshold voltage, approximately -15V, the residual charge increases with gate bias application time, while below threshold there is little increase in residual charge. For the dependence of residual charge on delay time, t_d, shown in Figure 6.3(b), we note a similar dependence for the characteristics measured

with initial applied gate bias above threshold, which show a relatively slow charge carrier detrapping with time at this temperature. However, we note that, for the case of the measurement with below threshold applied gate bias, the residual charge is reduced at a much faster rate. These results are evidence that the percentage of available trap states filled after a certain gate-bias application time is dependent on the applied gate bias, as expected. For the case of near- and below-threshold gate bias, we expect that the carriers occupy a small percentage of the available trap states in the material near the source and drain electrodes, which can be relatively easily depopulated at slightly above room temperature. While, for the case of applied gate bias significantly above the threshold voltage, the charge carriers occupy a much larger percentage of the available trap states.

The general expression for the residual trapped charge after time t for a distribution of trap states is given by $N(E)$ [1]:

$$Q(t) = Q_o \int \frac{N(E)}{N_t} exp\left[\frac{-t}{\tau(E,T)}\right] dE \tag{6.3}$$

where Q_o is the "charge prefactor" and corresponds to the amount of trapped charge immediately after the gate bias is removed, $N(E)$ is a function describing the energetic distribution of trap states and N_t is proportional to the total number of trap states and is calculated using:

$$N_t = \int N(E)\, dE \tag{6.4}$$

A characteristic time (i.e., average escape time) can be expressed using:

$$\tau(E,T) = \nu^{-1} exp(E/kT) \tag{6.5}$$

where ν is the attempt-to-escape frequency and is explained in more detail below.

Finally, the expression we have used for the normal (Gaussian) distribution of trap states with energy is:

$$N(E) = \frac{e^{-(E-E_o)/2\Delta E^2}}{\Delta E\sqrt{2\pi}} \tag{6.6}$$

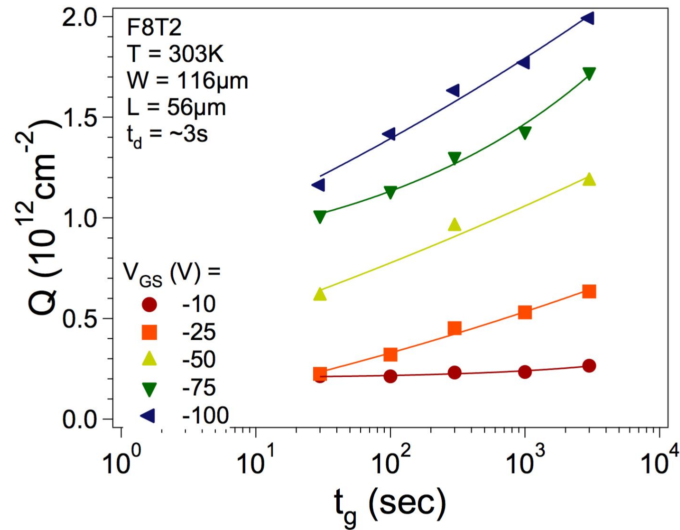

(a)

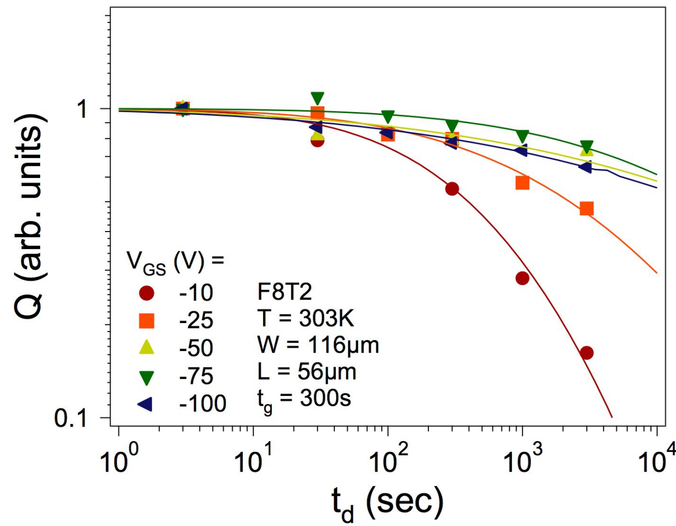

(b)

Figure 6.3: (a) Extracted residual charge as a function of gate bias application time for a range of gate bias levels at room temperature. The points correspond to the experimentally determined data and the lines are provides as guides to the eye. (b) Extracted residual charge as a function of delay time after a gate bias application at different voltages for 300 sec. The points correspond to the experimentally determined data and the lines correspond to the best least squares fit of the equations given in the text.

where, for the case described here, E_o is the center energy of the supposed normal distribution of trap states in the material and ΔE is the width (i.e., full-width at half-maximum) of the distribution. These parameters are described in more detail below.

The experimental data shown in Figure 6.3(b) has been fit using this set of equations along with the assumption of a normal (Gaussian) distribution of trap states. An iterative process that involved choosing initial fitting parameters to input into the Matlab code (see the Appendix) was used to generate the linear least squares fits (solid lines) shown in Figure 6.3(b). More specifically, this process consists of the following steps (both user controlled and automated program steps are included):

1. Initialize variables (i.e., Temperature, etc.).
2. Load experimental data and set Q_o equal to $Q_{t=0}$.
3. Choose valid initial guesses for E_o, ΔE and ν.
4. Create distribution of trap states based on these parameters and equation (6.6).
5. Generate fit based on equations (6.3), (6.4), and (6.5).
6. Calculate the residuals (i.e., difference between fit and experimental data) and the square of the residuals to get a measure of the validity of the fit.
7. Determine values of E_o, ΔE and ν that give the least square of the residuals for this iteration.
8. Return to 3 and use newly determined values of E_o, ΔE and ν as the initial values for this iteration.
9. Continue with this process until the desired level of fit accuracy is achieved.

Fits have been performed in this manner and are shown in Figure 6.3(b). The resulting dependencies of the fit parameters on the applied gate bias is shown in Figure6.4. The center energy of the trap distribution E_o has very little dependence on applied gate bias and has an average value slightly above 0.3eV. The energetic width of the trap distribution

ΔE appears to exhibit a slight increase with increasing gate bias magnitude and has a value near 75meV. The apparent spreading of the trap state energetic distribution with an increase of gate bias may be due to the fact that a growing portion of the density of states becomes occupied as the magnitude of the gate bias is increased. As noted above, the residual charge increases with increasing magnitude of gate bias as expected and as shown in Figure 6.4(b). The attempt-to-escape frequency ν does not exhibit any discernible dependence on the gate bias, though its value near 50Hz is relatively low compared to the values obtained for inorganic semiconductors [1]. We should note that a low value of ν, near 10Hz, was found for the analysis of the BTS experiments described in an earlier chapter.

We see from Figure 6.3(b), that applied gate biases significantly above the threshold voltage (i.e., $\gtrsim$ 20V) result in similar dependences on the delay time. To further investigate and gain some insight into the kinetics of the trap states, we perform the photodischarge measurements using a gate bias of -50V and vary the temperature of the device. We expect that increased temperature will speed-up the discharge of the traps, resulting in a smaller amount of residual charge at the same delay time but for higher temperatures. As we see in the next section, this is indeed the observation we make.

6.2.2 Dependence on temperature

General results that exhibit the dependence of the residual charge on gate bias application time and temperature are presented in Figure 6.5. From this figure, we observe the expected result that the amount of residual charge increases as the gate bias application time increases.

In Figure 6.6(a), we present experimental results for the photodischarge experiment performed for a range of delay times and device temperature. As expected, we see that the amount of residual charge decreases as the allowed relaxation time (i.e., delay time)

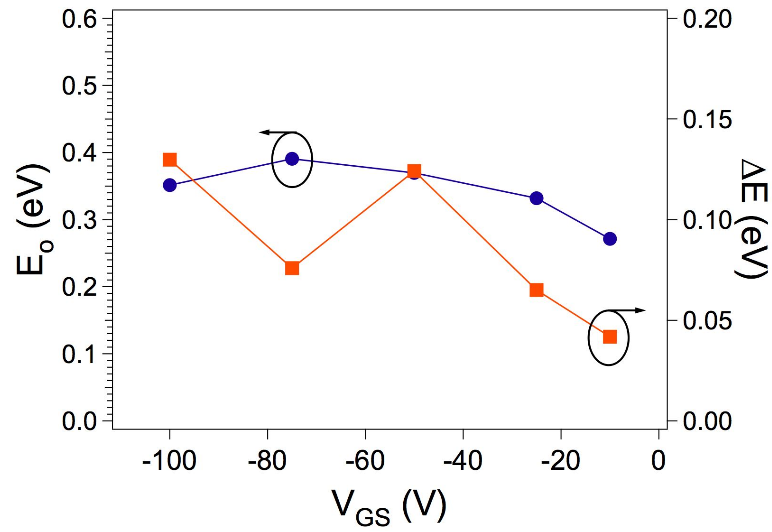

(a)

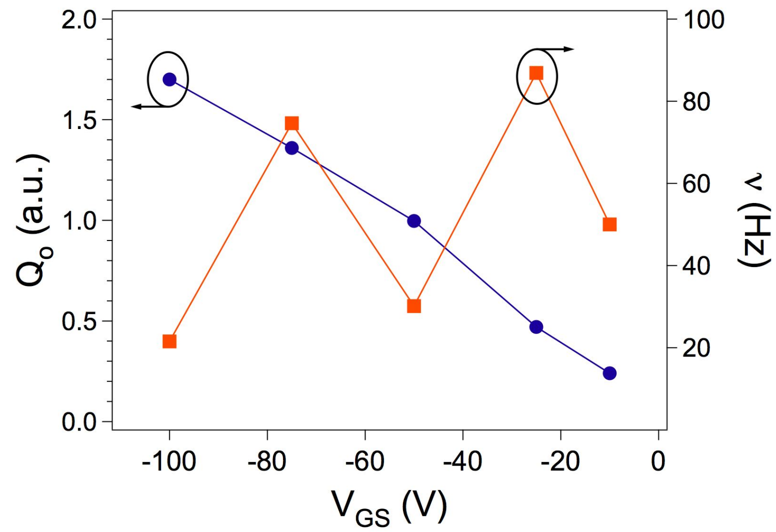

(b)

Figure 6.4: The dependence of the fit parameters ((a) E_o and ΔE and (b) ν and Q_o on gate bias.

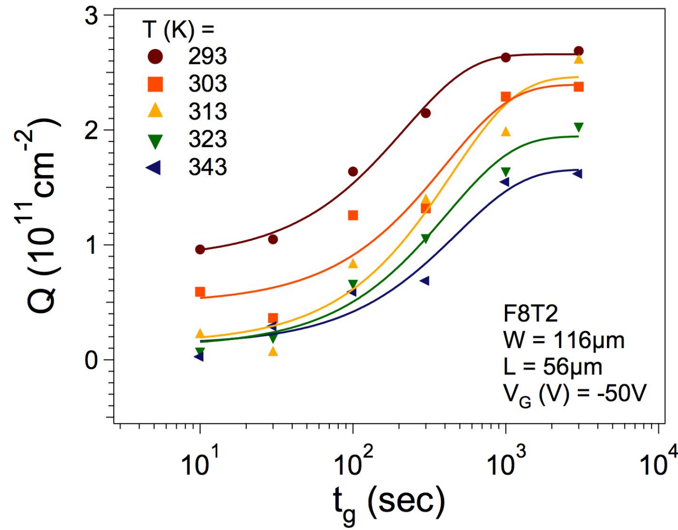

Figure 6.5: Residual charge versus gate bias application time for delay time of approximately 3 sec. Points are experimental data and lines are fits that serve as guides to the eye.

increases. Additionally, we note that this relaxation is faster with elevated temperature.

In Figure 6.6(b), we present the extracted residual charge as a function of the normalized delay time. This normalized delay time was found by dividing the delay time by the corresponding temperature dependent characteristic time given by equation 6.5. From this figure, we observe that the residual charge curves follow a similar trend and the observed differences in Figure 6.6(a) are simply due to the kinetics of the charge de-trapping at different temperatures.

Fits to the experimental data of Figure6.6(a) were performed using the same method as that which was described above. In Figure 6.7, we present the variation of the fit parameters with temperature. We can glean interesting observations from these figures. Most notably is the extremely small temperature dependence of the center energy of the trap state distribution, which has an average value of approximately 0.3eV. The energetic spread of the trap state distribution exhibits a slightly larger dependence on temperature, decreases with temperature, and has an average value of approximately 23meV, corresponding to a

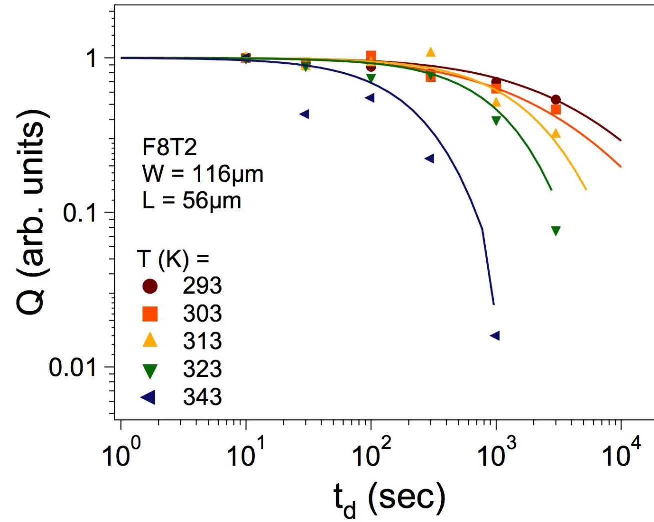

(a)

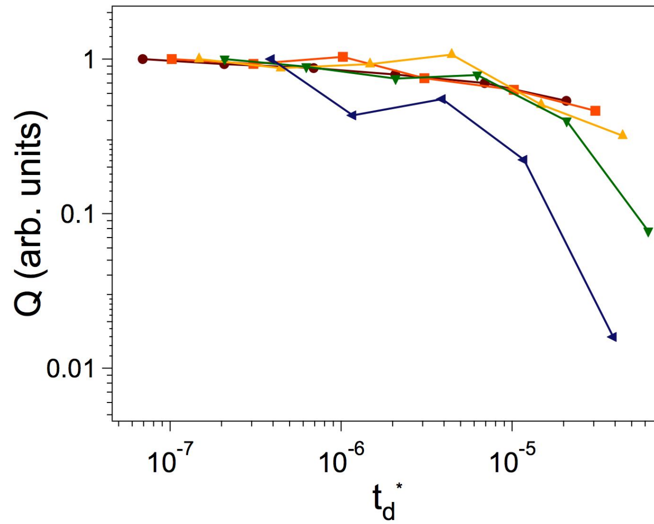

(b)

Figure 6.6: (a) Extracted residual charge as a function of delay time after a gate bias application of -50V for 300 sec for the same device measured at different temperatures. The points correspond to the experimentally determined data and the lines correspond to the best least squares fit of the equations given in the text. (b) Extracted residual charge plotted versus the normalized delay time.

temperature of approximately 350K. We also observe that the attempt-to-escape frequency, ν, is again relatively low and exhibits a linear dependence on and increases with temperature. The increase with temperature could be expected, since this parameter is roughly equal to the inverse of the average time taken by a charge carrier to be de-trapped. The "charge prefactor" of the fit corresponds to Q_o in equation 6.3. This parameter decreases slightly with temperature and this may be due to experimental limitations since at least several seconds pass between the end of the gate bias application and the beginning of the illumination pulse. We expect that a more sensitive experimental set-up could correct this problem.

The results from the parameter extraction and curve fitting described above allow us to estimate the shape of the density the trap states as shown in Figure 6.8. In other words, this is the normal distribution that provides the best fits of the temperature- and gate voltage-dependent date presented above. In this figure, we have shown the HOMO-LUMO gap of F8T2 and note that the trap states are centered at approximately 0.3eV above the LUMO (i.e., valence band) with a full-width at half-maximum of approximately 23meV. The slope of the band edges is schematic and simply indicates that there are expected band-tail states due to the amorphous nature of the semiconductor. The trap level of 0.3eV fits well with the activation energies of the field-effect mobility and with the results from the analysis of the BTS results described in an earlier chapter, providing a consistent set of data on the trap state distribution.

Finally, we should note that no meta-stability of the trap states has been observed for devices based on F8T2. In other words, the residual charge found for a measurement taken immediately after a previous measurement is the same as that found for the first measurement. If the trap states were meta-stable, we would expect to observe a greater amount of residual charge for the second measurement since the states formed in the first

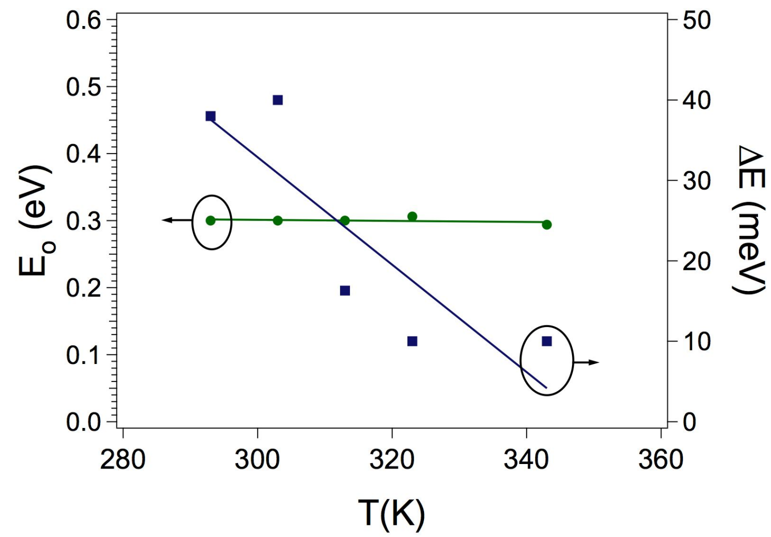

(a)

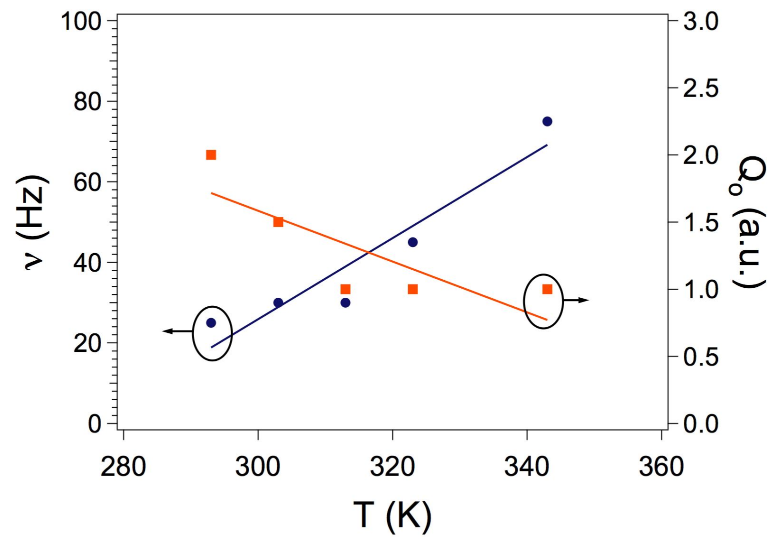

(b)

Figure 6.7: The dependence of the fit parameters ((a) E_o and ΔE and (b) ν and Q_o on temperature, points are actual data, lines are guides.

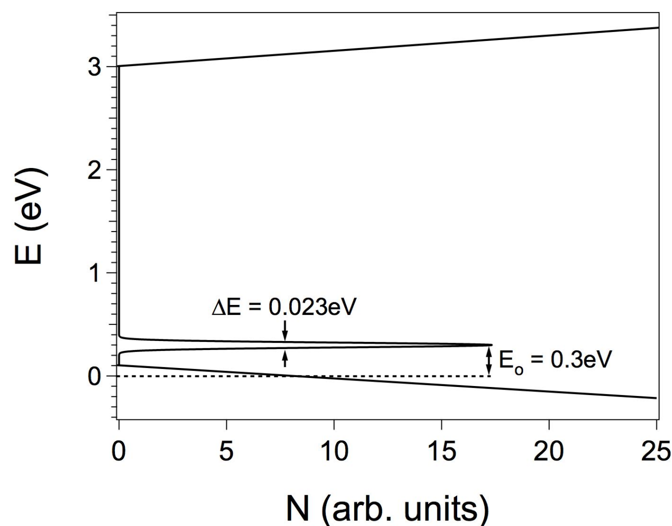

Figure 6.8: Density of states extracted from the photodischarge measurement described in this paper assuming a normal (Gaussian) distribution of trap states above the valence band.

measurement were not intentionally annealed-out.

6.3 Conclusion

In this chapter we have described the results of the photodischarge measurement performed on an F8T2-based OFET. This method has been described in detail and has been used to characterize the density of trap states and the trap state kinetics of the active organic semiconductor. By investigating the dependence of the residual charge on gate bias application time, delay time, temperature and applied gate bias, we have observed a relatively narrow trap state distribution at approximately 0.3eV above the valence band (HOMO level). This method shows promise for use as a characterization tool for comparing the trap state distribution and device performance of devices based on a variety of organic semiconductors and gate insulators.

References

[1] A. R. Hepburn, J. M. Marshall, C. Main, M. J. Powell, and C. van Berkel, "Eratta: Metastable defects in amorphous-silicon thin-film transistors," *Phys. Rev. Lett.*, vol. 56, pp. 2215–2218, 1986.

[2] ——, "Metastable defects in amorphous-silicon thin-film transistors," *Phys. Rev. Lett.*, vol. 57, p. 1192, 1986.

[3] J. Scherbel, P. H. Nguyen, G. Paasch, W. Brütting, and W. Schwoerer, "Temperature dependent broadband impedance spectroscopy on poly-(p-phenylene-vinylene) light-emitting diodes," *J. Appl. Phys.*, vol. 83, pp. 5045–5055, 1998.

[4] H. L. Gomes, P. Stallinga, H. Rost, A. B. Holmes, M. G. Harrison, and R. H. Friend, "Analysis of deep levels in a phenylenevinylene polymer by transient capacitance methods," *Appl. Phys. Lett.*, vol. 74, pp. 1144–1146, 1999.

[5] E. J. W. List, C. H. Kim, J. Shinar, A. Pogantsch, G. Leising, and W. Graupner, "Charged defects in highly emissive organic wide-band-gap semiconductors," *Appl. Phys. Lett.*, vol. 76, pp. 2083–2085, 2000.

[6] T. P. Nguyen, J. Ip, O. Gaudin, and R. B. Jackman, "Determination of localized trap parameters in organic semiconductors using charge based deep level transient spectroscopy (q-dlts)," *Eur. Phys. J. Appl. Phys.*, vol. 27, pp. 219–222, 2004.

[7] Y. S. Yang, S. H. Kim, J.-I. Lee, H. Y. Chu, L.-M. Do, H. Lee, J. Oh, T. Zyung, M. K. Ryu, and M. S. Jang, "Deep-level defect characteristics in pentacene organic thin films," *Appl. Phys. Lett.*, vol. 80, pp. 1595–1597, 2002.

[8] S. Kuniyoshi, S. Naruge, M. Iizuka, M. Nakamura, K. Kudo, and K. Tanaka, "Thermally stimulated current of pentacene schottky diodes," *Synth. Met.*, vol. 137, pp. 895–896, 2003.

[9] A. Hepp, N. von Malm, R. Schmechel, and H. von Seggern, "Effects of process parameters on trap distributions in organic semiconductors," *Synth. Met.*, vol. 138, pp. 201–207, 2003.

[10] A. Kadashchuck, R. Schmechel, H. von Seggern, U. Scherf, and A. Vakhnin, "Charge-carrier trapping in polyfluorene-type conjugated polymers," *J. Appl. Phys.*, vol. 98, p. 024101, 2005.

[11] W. Weise, T. Keith, N. von Malm, and H. von Seggern, "Trap concentration dependence of percolation in doped small molecule organic molecules," *J. Appl. Phys.*, vol. 98, p. 043511, 2005.

CHAPTER 7

CONCLUSIONS AND FUTURE WORK

7.1 Summary

Over the past several years, there have been significant improvements made in the performance of organic thin-film transistors, based on small molecules, oligomers and polymers. These improvements are due to the development of high performance organic semiconductor material, suitable device structures, as well as through the improvement in our understanding of how organic-based electronics work. By this last statement, we mean, improved theories of the charge carrier dynamics, improved understanding of the effects of material morphology, improved understanding of the effects of the various interfaces in the devices, and so on.

While there have been great strides made on these subjects in the recent past, it is obvious that there is still a lot of work to be done before a complete understanding of the important physical mechanisms and operating principles of these devices can be developed. The goal of this work is to provide to the organic electronics community, especially those concerned with organic tfield-effect transistors, thorough and well-developed models, experimental results and analysis. It is hoped that the results presented in this thesis will further the current understanding of the fundamental physical mechanisms occuring in and the operation principles of organic field-effect transistors.

In this thesis, various issues associated with polyfluorene derivative-based organic field-effect transistors (OFETs) have been discussed. More specifically, we have presented our investigation of the following:

- The DC electrical characteristics, performance, models and parameter extraction.
- The effects of illumination (both broadband and monochromatic) on the electrical characteristics, as well as the use of these devices as photodetectors.
- The hysteresis in the electrical characteristics of these devices.
- The instability mechanisms, studied by means of BTS.
- The kinetics and energetic distribution of the density of trap states of the organic polymer active layer.

In Chapter 2, we described the device structure and examined the DC electrical performance and characterization of the device. The main device structure studied is a patterned-gate, gate-planarized, inverted, coplanar thin-film transistor with the organic polymer F8T2 as the active layer semiconductor. The validity of electrical performance parameter extraction methods were studied and it was concluded that the inclusion of a field-dependent mobility provide the most reliable results. We used a model based on dispersive charge carrier transport in amorphous semiconductors and examined the temperature dependence of the electrical characteristics to find an activation energy of approximately 0.3eV for the field-effect mobility of holes in F8T2. We characterized the source and drain contact resistance and intrinsic device performance using standard electrical characterization methods, as well as the transmission line method. From this analysis, we found that the contact and channel resistances are very similar with values near $10^9\Omega$. We also observed that the contacts present Schottky-type behavior at low V_{DS}, which changes to a space charge limited current-type of behavior at higher V_{DS}. Additionally, we found that the main device structure studied here shows promise as a good candidate for high-voltage

(i.e., high-field) applications.

In addition to the DC performance characterization, the effects of broadband and monochromatic illumination on the electrical characteristics and performance of the F8T2-based OFETs was characterized and explained in Chapter 3. We found that, due to the photoconductive nature of the active layer, the major effect of the illumination was the photogeneration of excitons, which subsequently dissociate into charge carriers, and a corresponding reduction of the threshold voltage and increase in the OFF-state drain current, resulting in a diminished control of the gate over the channel. The illumination does not affect the field-effect mobility. The observed effects are explained by exciton and the photo-field effect theory for amorphous semiconductors. The photo-field effect theory provides information about the density of states, including an estimation of the density and slope of the gap states near the position of the Fermi levels under illumination. We also used this method to find an estimate of the flat-band voltage of approximately -10V. The performance of this device as a photodetector was characterized and we found a responsivity of approximately 1A/W in the ON-state, a photosensitivity of greater than 100 in the OFF-state, an external quantum efficiency greater than 100%, and a noise equivalent power of 10^{-14} WHz$^{-0.5}$. Based on these results, we found that OFETs can be very sensitive to the illumination depending on the absorption spectrum of the active layer. This effect can be beneficial if the device is to be used as a photodetector, however, in many of the proposed applications of OFETs, the exposure to illumination should be minimized in order to maintain control over the performance of the device.

The subject of Chapter 4 was the hysteresis in the electrical characteristics of the F8T2-based OFETs. Hystersis shifts of greater than 5V can be observed. This undesired effect is indicative of poor device stability and prohibits the use of these devices in commercial applications. Through gate-bias-, temperature- and illumination-dependent studies, we

found that the amount of hysteresis is strongly dependent on the density of charge carriers in the channel and is a relatively easily reversed charge trapping effect. Additionally, we found that with the addition of an organic insulator between the inorganic insulator and the organic semiconductor, the hysteresis could be eliminated. These results lead us to the conclusion that the hysteresis is related to the charge carrier trapping in the organic polymer, at or near the organic semiconductor / gate insulator interface, which is triggered by the accumulation of a large density of carriers in the polymer channel of the device.

Further studies of the instabilities were presented in Chapter 5, where we performed and analyzed the effects of negative/positive, DC/AC bias temperature stress on the F8T2-based OFETs and observed that the major effect is a threshold voltage shift. The DC bias and temperature dependence of the instabilities followed a stretched-exponential dependence for bias stress effects in amorphous semiconductors and allowed the determination of the distribution of trap states centered near 0.25eV above the valence band (HOMO-level). Negative AC BTS showed a dependence on the total stress time, demonstrating the combination of several physical phenomena, including slow carrier transport and the existence of few reversible and many irreversible trap states. Additionally in this chapter, we have noted that the electrical performance of the F8T2-based OFETs, as well as OFETs based on other organic semiconductors, appears to increase, peak and then decrease as the temperature of the device is increased. This effect could have profound influence on the development of commercial applications based on this type of devices, since, it is expect that in most applications, the devices will be subjected to temperatures in excess of the peak performance temperature.

Finally, in Chapter 6, we presented the first known use of the photodischarge method to investigate the energetic distribution and kinetics of the trap states in the organic semiconductor. Through a study of the dependence of the residual charge on gate bias application

time, delay time, temperature and applied gate bias, we have observed a relatively narrow trap state distribution at approximately 0.3eV above the valence band (HOMO level).

It is interesting to note that the major results obtained from this set of experiments and analyses provide a relatively consistent picture of the density of states of the organic semiconductor active layer material, which governs the operation of the F8T2-based devices. However, as is always the case, there appears to still be much more we can learn about this unique class of materials, in addition to the development of applications that will allow these devices based on these materials to be commercialized. Several ideas for future directions are summarized in the next, and final, section.

7.2 Future directions

There is still much work to be done before a complete understanding of the fundamental physics and operating mechanisms of organic-based electronics can be reached. It seems reasonable that the following fabrication and characterization experiments could continue to push the field in the right direction:

- Development and synthesis of conjugated organic molecules with enhanced environmental stability.
- Reduction of device size to enter the realm of having one or a few trapped electrons.
- Characterization of material with and without trapped charge (i.e. through the use of in situ electron spin resonance) in order to more closely determine the properties of the trapped charge (i.e. polaron vs. bipolaron).
- Further characterization of the density of trap states through the use of methods such as deep level transient spectroscopy (DLTS) and thermally stimulated current (TSC), especially when used to compare the trap state properties and charge transport properties of a range of organic semiconductors with different molecular structures, as

well as for devices with different structures.

It is obvious that the current status of the performance of organic-based electronics prohibits the direct competition of these devices and applications with the inorganic-based electronic systems. However, in the not-so-distant future, it seems reasonable that this class of materials and devices will find their way into many useful and interesting applications. We can imagine applications such as:

- Fully-organic and fully-integrated organic photodetectors and circuitry.
- Organic-based photovoltaics on curved and flexible substrates for use in non-flat geometries.
- Integration of organic devices into biological applications such as drug delivery systems, sensory integration systems, and rf-monitoring systems.
- Organic semiconductor-based lasers.

APPENDIX

```
\% Qfit303gratest50.m
\% Mike Hamilton
\% 09/16/2005

\% Matlab script to determine the least squares fit of the residual
\% charge (from the photodischarge measurement) versus delay
\% time.
\% This program is specifically for T = 303K, however, other
\% programs exist for other temperatures, or this program can
\% easily be modified to be use with the desired user inputs of
\% temperature, time and residual charge values.
\% This program calls a function called ‘‘normdist.m’’ that is defined
\% here for reference function y = normdist(x,m,s)
\% y = (exp((-(x-m).^2)./(2*s.^2)))/(s*sqrt(2*pi));

\% Initialize and load t and Q data
clear all;
t=[3;30;300;3000];
Q303data=[0.00997375;0.00816;0.00791187;0.00724688];

\% Ask user for intitial guess of fitting parameters, after running once,
\% the user should input the output values as the new guesses
\% (i.e. it’s an iterative process) and continue performing this process
\% until the square of the residuals isn’t changing much.
Eo1=input(’Initial guess of E_{o} (eV) = ( > 0 and < 2) ’);
dE1=input(’Initial guess of \Delta E (eV) = ( > 0 and < 0.5) ’);
nu1=input(’Initial guess of \Nu (Hz) = ( > 1 and < 10^12) ’);
Qo=Q303data(1);

\%Qo=input(’Initial guess of Q_{o} (cm^{-2}) = ( ~ 2e-3) ’);
k=8.617e-5;
T=303;
Eo=linspace(0,2*Eo1,501);
dE=linspace(0.0001,2*dE1+0.0001,501);
nu=logspace(log10(nu1)-5,log10(nu1)+5,501);

\% First vary Eo, this section also plots the square of the residuals versus
\% Eo for graphical confirmation
for j=1:501
    Nt(j)=quad(@normdist,0,2,[],[],Eo(j),dE1);
    for i=1:4
        Qn(i)=quad(@qfun,0,2,[],[],Eo(j),dE1,t(i),nu1,k,T);
        Q(i)=(Qo/Nt(j))*Qn(i);
    end
Qt=Q.’;
REobase=Qt-Q303data;
REobasesum=sum(REobase);
```

```
REo=(Q303data-Qt).^2;
REo2(j)=sum(REo);
end
subplot(3,1,1);
semilogy(Eo,REo2,'k*');

\% Find value of Eo for minimum R^2
[y1,i1]=min(REo2);
MinEo=Eo(i1);
y1;

\% Use Eo value from above and vary dE, this section also plots the square
\% of the residuals versus dE for graphical confirmation
for j=1:501
    Nt(j)=quad(@normdist,0,2,[],[],MinEo,dE(j));
    for i=1:4
        Qn(i)=quad(@qfun,0,2,[],[],MinEo,dE(j),t(i),nu1,k,T);
        Q(i)=(Qo/Nt(j))*Qn(i);
    end
Qt=Q.';
RdEbase=Qt-Q303data;
RdEbasesum=sum(RdEbase);
RdE=(Q303data-Qt).^2;
RdE2(j)=sum(RdE);
end
subplot(3,1,2);
semilogy(dE,RdE2,'k*');

\% Find value of dE for minimum R^2
[y2,i2]=min(RdE2);
MindE=dE(i2);
y2;

\% Use Eo and dE values from above and vary nu, this section also plots
\% the square of the residuals versus nu for graphical confirmation
for j=1:501
    Nt(j)=quad(@normdist,0,2,[],[],MinEo,MindE);
    for i=1:4
        Qn(i)=quad(@qfun,0,2,[],[],MinEo,MindE,t(i),nu(j),k,T);
        Q(i)=(Qo/Nt(j))*Qn(i);
    end
Qt=Q.';
Rnubase=Qt-Q303data;
Rnubasesum=sum(Rnubase);
Rnu=(Q303data-Qt).^2;
Rnu2(j)=sum(Rnu);
end
```

```
subplot(3,1,3);
loglog(nu,Rnu2,'k*');

\% Find and output values of Eo, dE and nu for minimum R^2's
MinEo
y1
MindE
y2

[y3,i3]=min(Rnu2);
Minnu=nu(i3)
y3

\% Beep to tell the user that it's done with this iteration
beep;
```

ABSTRACT

POLYFLUORENE-BASED ORGANIC FIELD-EFFECT TRANSISTORS

by
Michael C. Hamilton

Chair: Jerzy Kanicki

The electrical performance and device stability of a patterned-gate, gate-planarized, inverted, coplanar thin-film transistor with an organic polymer F8T2 active layer semiconductor was studied. The validity of electrical performance parameter extraction methods was studied and the inclusion of a field-dependent mobility provided the most reliable results. A gate-bias dependent activation energy near 0.2eV for the field-effect mobility of holes in F8T2 was found. The source and drain contact and channel resistances were characterized and are similar with values near $10^9\Omega$. Additionally, these devices showed promise for use in high-voltage applications. The effects of broadband and monochromatic illumination were characterized and strongly absorbed illumination reduced the threshold voltage. Application of a photo-field effect theory provided an estimation of the density and slope of the gap states. This method also provided an estimate of the flat-band voltage of -10V. The performance of the device as a photodetector showed a responsivity of 1A/W, a photosensitivity greater than 100, an external quantum efficiency greater than 100%, a noise equivalent power of 10^{-14} $WHz^{-0.5}$ and a specific detectivity of approximately 2×10^{11} $cmHz^{0.5}W^{-1}$. Hysteresis in the transfer characteristics was characterized

by the dependence on the applied gate-bias, temperature and illumination. It was observed that the hysteresis is a charge trapping effect that is dependent on the charge density within the channel. The hysteresis was eliminated by incorporating an organic insulator layer between the inorganic insulator and the organic semiconductor. Bias temperature stress effects were characterized and the major effect was an increase in threshold voltage. Analysis using a stretched exponential behavior for DC bias stress effects showed that there exists a distribution of trap states centered at 0.25eV above the valence band. Negative AC BTS resulted in a dependence on the total stress time and demonstrated the combination of several physical phenomena, including slow carrier transport and the existence of few reversible and many irreversible trap states. A relatively low (65°C) optimal operating temperature of organic-based devices was observed. The trap states were further characterized using the photodischarge method to investigate the kinetics and distribution of trap states. A narrow distribution of trap states at 0.3eV above the valence band was found, which is consistent with field-effect mobility and bias temperature stress results.